Corrections

Elena Terzić

February 2019

- **pg. iii/iv** Glossary added
- Captions were put above all tables throughout the text (before they were below).
- **pg. 39, eq. 2.4** updated
- **pg. 44** MS changed to Mediterranean Sea. Same applies for the entire Chapter 3.
- **pg. 47** Sentence added: "The Northern Ionian subbasin however proves to be an exception due to higher-than-average CDOM concentrations, which in turn invalidate the gradient by causing higher K_d values at shorter wavelengths.
- **pg. 49, Table 2.3** Caption corrected from K_d to K_{bio}.
- **pg. 51, Table 2.4** Caption corrected from K_d to K_{bio}.
- **pg. 52, line 6** Attenuation depths specified for 380 and 412 nm separately (45 and 60 m NWM, 90 and 120 m SLEV).
- **pg. 56, 4th paragraph** regression analyses corrected from REF01, REF02 to REG01, REG02.
- **pg. 57, Table 2.5** Decreased table width and font size.
- **pg. 64, section 3.2.2.** Explanation of the term "voxel": "which represents a value on a regular grid in 3-dimensional space (i.e. a "3-dimensional pixel").
- **pg. 65** 3.2.2. subsection substituted with "Vertical Mixing Models subsection".
- **pg. 65** Sentence replacement: from "Furthermore, a first attempt to model the impact of CDOM has been made ..." to: "Furthermore, the impact on light propagation ..."
- **pg. 66, line 13** Added: "according to bacterial capability of decomposing them to inorganic compounds."

- **pg. 67, Bio-Optical Models** First sentence modified to: "Alternative solutions to measured PAR profiles were used in models OPT1, OPT2abcd, OPT3, OPT4abc and OPT5."
- **pg. 67, eq. 3.5** equation corrected to $K_d(PAR) = a\,[Chl]^b + c$
- **pg. 70, section 3.3.1** Sentence added: "The assimilation of PAR profiles into the 1-D model helped to accurately estimate the DCM depth."
- **pg. 70** A sentence was removed between "At surface, ..." and the last paragraph: "In addition to ..."
- **pg. 71, Figure 3.1** Sentence added: "Floats' names, along with their tracking positions and periods, are reported in Appendix A within Chapter 2."
- **pg. 79, last paragraph** Removed reference [Antoine et al., 2008].
- **pg.80** Last sentence modified.
- **pg. 99, Figure 4.6** "REAN" abbreviation added in the caption.
- **pg. 100, Figure 4.7** "REAN" abbreviation added in the caption.
- **pg. 111 and 112, Figure 4.13 and 4.14** Bar plots titles removed, y-axis labels enlarged.
- **pg. 112, Figure 4.14** Caption corrected from: "K_d^{var} and K_d^{clim}" to "$K_d^{var} - K_d^{clim}$"
- **118, 2nd paragraph** RMSE value corrected from 0.03 to 0.035 m^{-1} for the North-Western Mediterranean subbasin.
- **pg. 121, Figure 4.20** Bar plots titles removed, y-axis labels enlarged.

UNIVERSITÀ
DEGLI STUDI DI TRIESTE

Marine bio-optical properties applied to biogeochemical modelling

Maths and Geosciences Department

Doctoral School in Earth Science, Fluid-Dynamics and Mathematics. Interactions and Methods – XXXI Cycle

Candidate

Elena Terzić

ID number PHD0900026

Thesis Advisor

Dr. Stefano Salon

Co-Advisors

Dr. Paolo Lazzari

A thesis submitted in partial fulfillment of the requirements
for the degree of Doctor of Philosophy in Earth Science, Fluid-Dynamics and Mathematics

2017/2018

Elena Terzić. *Marine bio-optical properties applied to biogeochemical modelling.*
Ph.D. thesis. University of Trieste

EMAIL: eterzic@inogs.it

Glossary

Symbol	Definition	Units
a	absorption coefficient	m^{-1}
a_{CDOM}	CDOM absorption	m^{-1}
a_{nap}	absorption of non-algal particles	m^{-1}
a_{ϕ}	phytoplankton absorption	m^{-1}
AOP	apparent optical property	
AC-S	spectral absorption and attenuation meter	
b	scattering coefficient	m^{-1}
b_b	backscattering coefficient	m^{-1}
b_{bp}	particulate backscattering	m^{-1}
β	volume scattering function	$m^{-1}\,sr^{-1}$
BFM	Biogeochemical Flux Model	
BFM_i	reaction term corresponding to the tracer C_i	
B/G	blue-to-green Ratio	
BGC-Argo	Biogeochemical-Argo	
c	beam attenuation coefficient	m^{-1}
CDOM	colored dissolved organic matter (gelbstoff, gilvin)	
C_i	i-th biogeochemical tracer	
Chl	chlorophyll a concentration	$mg\,m^{-3}$
c_p	beam attenuation of particulate matter	m^{-1}
CV	coefficient of variance	%
DCM	deep chlorophyll maximum	
DOC	dissolved organic carbon	$mgC\,m^{-3}$
D_v	vertical eddy diffusivity coefficient	$m^2\,s^{-1}$
E_d	downward planar irradiance	$W\,m^{-2}\,nm^{-1}$
E_o	downward scalar irradiance	$W\,m^{-2}\,nm^{-1}$
FDOM	fluorescent fraction of the dissolved organic matter	
HPLC	high-performance liquid chromatography	
K_{bio}	K_d for all biogenic components	m^{-1}
K_d	diffuse attenuation coefficient	m^{-1}

K_d^{clim}	climatological K_d	m^{-1}
K_d^{var}	interannually variable K_d	m^{-1}
K_w	K_d for pure water	m^{-1}
L	spectral radiance	$W\,m^{-2}\,nm^{-1}\,sr^{-1}$
λ	wavelength	nm
Lat	latitude	$^\circ$
Lon	longitude	$^\circ$
L_u	upwelling radiance	$W\,m^{-2}\,nm^{-1}\,sr^{-1}$
L_w	water-leaving radiance	$W\,m^{-2}\,nm^{-1}\,sr^{-1}$
MAREDAT	MARine Ecosystem DATa	
MERIS	MEdium Resolution Imaging Spectrometer	
MLD	mixed-layer depth	m
MODIS	MODerate resolution Imaging Spectroradiometer	
μ_d	average cosine for downwelling irradiance	
NPQ	non-photochemical quenching	
PAR	photosynthetically active/available radiation	$\mu\,mol\,quanta\,m^{-2}\,s^{-1}$
PFT	phytoplankton functional types	
POC	particulate organic carbon	$mg\,C\,m^{-3}$
PSD	particle size distribution	
ρ_θ	potential density	$kg\,m^{-3}$
QED	quantum electrodynamics	
RMSE	root mean square error (alternatively RMSD)	arbitrary
R	reflectance	
R_{rs}	remote sensing reflectance	sr^{-1}
RTE	radiative transfer equation	
RTM	radiative transfer model	
S	salinity	PSU
SeaWiFS	Sea-viewing Wide Field-of-view Sensor	
SRTE	scalar radiative transfer equation	
SST	sea surface temperature	°C
T	temperature	°C
VIIRS	Visible Infrared Imaging Radiometer Suite	
UV	ultraviolet	
v_{sink}	sinking velocity	$m\,s^{-1}$
VRTE	vector radiative transfer equation	
z_{eu}	euphotic depth	m
z_{od}	first optical depth	m

Contents

Introduction

The seminal idea of optical oceanography is that by inspecting the colour of the ocean, we can get a grasp on the biogeochemical composition of the water body. The field is used in many applications, ranging from ecology and biogeochemistry, to the understanding of possible hazards in our oceans and the emerging trend of climate change [IOCCG, 2008].

The term 'ocean colour' stems from the fact that the visible part of the spectrum is used by the ocean ecosystem for photosynthesis, which accounts for almost half of the global photosynthesis on Earth. The ocean habitat however differs from the land, as conditions are not always in favour of having both light and nutrients present to make photosynthesis and thus carbon dioxide intake possible. The growth of phytoplankton is therefore linked to physical processes and inversely, the sole process of phytoplankton growth modulates the underwater light field, which illustrates how physics and biogeochemistry are interrelated and a chain link between the three components (optics, biogeochemistry and hydrodynamics) is essential for a more accurate modelling approach.

Physical processes in the ocean are fundamentally related to the biogeochemical and light environment and thus impact the growth of phytoplankton, which requires both light and nutrients. Advection, diffusion and mixing can control the supply of nutrients and therefore influence the distribution of phytoplankton in the mixed layer or during stratified conditions (e.g. deep chlorophyll maximum formation). Inversely, phytoplankton growth can alternate the light field and in turn change the rate of solar heating, therefore changing the hydrodynamics of the water body. In order to understand fully how physics links to biology and vice versa, numerical simulations provide an essential tool to understand their dynamics also on larger spatio-temporal scales.

The emergence of satellites and the constant refinement of algorithms used for optical and biogeochemical variables retrieval has proven to be essential for a number of different fields, ranging from physical oceanography, biogeochemistry, fisheries and coastal management [IOCCG, 2008]. Such an observational tool provides information on (quasi-)synoptic scales, however limiting the analyses

to the penetration depth or first optical depth [Gordon and McCluney, 1975]. The largest limitation of satellite remote sensing products is that the quantities are derived through the use of inversion algorithms, therefore providing only indirect measurements [IOCCG, 2011]. Moreover, satellite data sets are subject to frequent gaps due to clouds and atmospheric aerosols, or persistent data gaps in winter due to low sun angle [Cole et al., 2012].

Inversely, research cruises provide information also on biophysical variables along the water column, but are spatially scarce and temporally biased due to unfavourable weather conditions to carry out measurements during the whole year or seasonal span.

Autonomous platforms, such as gliders and Biogeochemical-Argo (BGC-Argo) floats, have in recent years proven to be a useful tool to complement the shortcomings of research cruises and can thus provide data for regions and seasons which are otherwise inaccessible. Their advantage over satellite products, apart from the possible measurements at deeper layers, is that no algorithms are needed for the bio-optical variable retrieval. An increased density of such platforms could prove useful both for satellite-derived product validation, as well as for potentially merging float data with biogeochemical models. Quality-controlled radiometric measurements could be, due to their refined vertical resolution, used as alternative light models in 1-dimensional simulations, whereas biogeochemical variables could be useful for the validation of such models. Furthermore, information on measured optical properties could be potentially used as additional model constraints.

For numerical models that aim to represent large-scale ocean features, data from satellite can be used for model initialization, assimilation, as well as for validation. Constraining the model with satellite data has been used for various operational applications, which can be sub-divided into two major categories: using ocean color for the improvement of the underlying bio-physical processes or else for operational purposes [IOCCG, 2008].

Data assimilation merges observations and models and its aim is to bring the model into consistency with observations. Such an approach might be useful for parameter optimization [Ciavatta et al., 2011] and for providing state estimates (for operational purposes [Teruzzi et al., 2014, 2018]). Assimilating apparent optical properties or AOPs [Ciavatta et al., 2014; Jones et al., 2016] proves to be a step further in bio-optical modeling, as the error in satellite data retrieval is generally lower for optical properties compared to biogeochemical variables like chlorophyll concentration.

In most biogeochemical models, which are successfully coupled with hydrodynamics, the description of optics is generally (over)simplified, therefore one of the necessary improvements still remains the integration of a more complex

optical model, where inherent and apparent optical properties (IOPs and AOPs respectively) are already included as model state variables. [Fujii et al., 2007].

The description of light propagation in the ocean ranges from simple, exponentially attenuating profiles of photosynthetically active radiation (PAR), to the fully coupled hyperspectral radiative transfer model, as described in Mobley et al. [2015]. Although most models use the former (simpler) one, much progress has been done in addressing the importance of improving light for better calculations both of physics and biogeochemistry by solving spectral irradiance, such as in Baird et al. [2016a]; Dutkiewicz et al. [2015]; Fujii et al. [2007]; Gregg and Casey [2007] and Bissett et al. [1999].

The final goal of the thesis project is to improve the quality of Copernicus Marine Environment Monitoring Service (CMEMS [1]) biogeochemical products for the Mediterranean Sea through the development of a new optical module for the MedBFM forecasting model system.

CMEMS products quality assessment requires the comparison of model outputs with observations and the use of specific metrics. A quality-controlled bio-optical in-situ data set from the Biogeochemical-Argo Mediterranean floats network (BGC-Argo, with 4 radiometric, 2 physical and 1 biogeochemical variable) and remote sensing products from the Copernicus Marine Data Stream (inter-annually variable weekly data of diffuse attenuation coefficients of downward planar irradiance, K_d^{var}, at 490 nm) were used for such purpose.

In both cases, the optical data (PAR profiles and $K_d(490)$ maps respectively) served as model input for the MedBFM system (in 1- and 3-dimensional settings), whilst the biogeochemical data from BGC-Argo floats (fluorescence-derived chlorophyll concentration profiles) and HPLC-obtained chlorophyll data from MAREDAT [Buitenhuis et al., 2013] were used for validation purposes.

The work included two different MedBFM model configurations: first in the form of a non-assimilative 1-dimensional model with various bio-optical and mixing parametrizations, where the former might serve both as a first step towards more complex optical representations and could on the other hand have a diagnostic utility by inspecting the product quality through the use of BGC-Argo floats. The combined use of a biogeochemical model of medium complexity (i.e. BFM [Lazzari et al., 2010, 2012, 2016]) with a rich data set enabled also an in-depth study on the biogeochemistry of the examined basin. The second configuration focused on the impact of using weekly variable K_d^{var} versus climatological K_d^{clim} values as a full 3-dimensional model optical forcing, thus estimating the effect of an updated data set in terms of spatio-temporal variability of the chlorophyll field and output quality.

Chapter 1 presents a brief overview of optical oceanography: its historical

[1] http://marine.copernicus.eu/

development, general theory and bio-optical anomalies of the examined basin. Chapters 2 and 3 adopted a BCG-Argo data set comprised of 31 floats (1314 profiles) for the period between 2012 and 2016. In Chapter 2, the analysis was focused on quality-checked profiles of downward planar irradiance (E_d) at three different wavelengths (380, 412 and 490 nm) and of photosynthetically active radiation for planar irradiance sensors (PAR), which have been used to obtain their depth derivatives - the diffuse attenuation coefficients (K_d). A comparison has been made with a bio-optical model proposed by Morel and Maritorena [2001] and its later corrections for specific wavelengths [Morel et al., 2007b] in order to ascertain the adequacy of taking chlorophyll as a proxy for all biogenic components, merging impacts of phytoplankton, particulate and colored dissolved organic matter (CDOM) in only one term. The use of such relatively simple bio-optical models was extended from the first optical depth (which is the depth of the satellite signal penetration, ranging approximately between 15 and 35 m in the Mediterranean Sea) to the first 150 meters, exploring the possibility to use such algorithms beyond satellite remote sensing applications. Due to the biogeochemically complex nature of the Mediterranean basin, it is debatable whether the enhanced content of CDOM in the region and its high absorption in the near-UV/blue range might increasingly contribute to the light attenuation in the blue part of the spectrum and whether could be therefore correctly quantified within the chlorophyll concentration term. Similarly, the possibility of describing $K_d(PAR)$ with $K_d(490)$ is explored, which could enable a new modelling parametrization described in Chapter 4.

In Chapter 3, an example of merging different techniques was investigated by adopting a 1-D version of the 3-D biogeochemical model embedded in the MedBFM system. In particular, the BGC-Argo data set described above was integrated in 1-D model simulations following trajectories of each float and considering measured planar PAR profiles as the reference light parametrization. The simulations were aimed to be consistent with data measured by float sensors, especially in terms of deep chlorophyll maximum (DCM) depth. Several light models were tested in order to estimate their impact on modeled biogeochemical properties, including self-shading dynamics based on chlorophyll and CDOM concentrations. Results, evaluated with the corresponding in-situ BGC-Argo chlorophyll data, indicate that the proposed approach allows to properly simulate the chlorophyll dynamics and illustrate how PAR and vertical mixing are essential environmental regulation factors driving primary producers dynamics. Higher skills are reached using in-situ PAR, but some of the alternative bio-optical models show comparable skill in reproducing DCM depth spatial variability. Simulation results show that during the stratification phase the diel cycle has significant impact on the surface chlorophyll regimes.

The work done in this chapter has been submitted to Biogeosciences [Terzić et al., 2018] and is currently under revision.

In Chapter 4, satellite data from the Copernicus Marine Data Stream were acquired in order to update the optical algorithm that has been used so far in the MedBFM model within CMEMS. The objective was to quantify the sensitivity of model results using climatological (K_d^{clim}) vs. improved (K_d^{var}) data (based on ESA CCI merged files for $K_d(490)$) in terms of chlorophyll concentrations. The output was validated also through the use of the quality-controlled BGC-Argo data set previously described, which was compared to corresponding model outputs at given locations. A similar analysis was carried out in terms of apparent optical properties, where a match-up was done between $K_d(490)$ values from the BGC-Argo data set and the spatio-temporally corresponding satellite points. Results indicate that by using the interannually variable data set, the divergence of updated K_d values compared to climatological ones extends to 20%, which results in variations in surface chlorophyll concentration magnitudes for up to 50 % compared to the use of a climatological data set. By looking at surface chlorophyll trends, seasonal variability decreases for approximately 5%, whereas the interannual variability varies among different sub-basins for up to 20%. The DCM on average increases for 10 m with the use of K_d^{var}, while DCM chlorophyll values result in minimal decreases in western subbasins (0.03 $mg\,m^{-3}$). A time series analysis around the BOUSSOLE site shows a significant underestimation (more than 50%) of the model chlorophyll output compared to HPLC data, which is in-line with the previous reanalysis assessment. A match-up with BGC-Argo float profiles of fluorescence-derived chlorophyll shows a slightly lower root mean square error (RMSE) and higher correlation with the use of K_d^{var}, thus displaying only a slight increase of the model product quality. A similar match-up was performed by comparing K_d coefficients from satellites and the ones derived from BGC-Argo radiometric data at 490 nm for the first optical depth, which resulted in systematically higher results from remote sensing observations compared to in-situ measurements.

Such an integrated approach could be useful as a first step towards the implementation of a hyperspectral radiative transfer model, which would present a fundamental upgrade to obtain a more accurate description of the underwater light field, impacting both biogeochemistry and hydrodynamics.

Chapter 1

Ocean Optics - An Overview

Abstract

The aim of the present chapter is to give the reader a concise recap of three major topics involving this work:

1. The historical development of optical oceanography as a scientific branch, which has drastically expanded in the last 40 years.

2. A descriptive summary of the radiative transfer theory through the derivation of the scalar radiative transfer equation, the applications of its simplified (analytical) solutions, concluding with the introduction of inversion methods and a brief case study of forward modelling.

3. The advancement of optics for biogeochemical studies in the region of interest, i.e. the Mediterranean Sea. This section focuses especially on the "bio-optically anomalous" nature of the basin and on the state-of-the-art knowledge, addressing the questions that still arouse interest in the research community.

Note that the scope of the following pages is not to revise the theory in its entirety by writing all the necessary equation derivations in order to obtain final solutions, but rather to draw a framework of the present thesis, as well as address the applications and practical importance of the field, thus describing cases when such tools are or could be used.

1.1 Historical Overview

Classification of natural waters into optical water types, as many other taxonomies, has been done in order to generalize and systematize the science of ocean colour and has undergone a major development since the beginning of optical oceanography studies, which probably started due to an enhanced interest among mariners who wanted to find a way to measure the water depth beneath their vessels. According to Arnone et al. [2004], the Secchi disk, invented around 1865 by the commander of the papal navy, Pietro Angelo Secchi, by studying the disappearance of circular disks in the Tyrrhenian Sea, is considered as the first quantitative optical instrument that has been used to measure water transparency and hence provided the ability to differentiate water mass based on their optical properties. Such measurements still represent the largest assemblage of in-situ optical data, thus, despite their spatio-temporal limitations and the current availability of more sophisticated

methods, still arouse interest in modern research (e.g. Preisendorfer [1986]; Lee et al. [2015, 2016] or Megard and Berman [1989] for the Eastern Mediterranean Sea).

By the late 1800s and early 1900s, transparency measurements were upgraded by the use of colour-based comparators, such as the Forel-Ule scale, which was invented for the optical classification of Swiss lakes in 1890 [Barale and Schlittenhardt, 2012]. Different inorganic compounds with standard formulas are (still) used to produce a colour palette with twenty one fluid vials covering tints varying from indigo-blue to coca-cola brown [Wernand and Van der Woerd, 2010]. The analysis consists of finding the vial that matches best the colour of the water body, resulting in an index from 1 to 21. Such measurements are still of interest due to the method's simplicity, as well as to a large database of historical observations available (often used in conjunction with the Secchi disk), which has value for studies of long-term changes in ocean ecosystems [Mobley et al., 2010]. Today it is possible to make Forel-Ule measurements also by simply using a smart-phone application [1].

Upon the development of reliable underwater radiometry toward the end of World War II and the publication of first large-scale empirical data sets, Jerlov [1968, 1976] introduced a classification of water bodies based on their spectral optical attenuation depth, z_k, which is inversely proportional to the diffuse attenuation coefficient of downward planar irradiance K_d. Since ocean colour is inversely proportional to the absorption coefficient a (and thus to K_d for homogeneous bodies with negligible effects of inelastic scattering), the spectra is linked to the observed colour. Observations are discretized into 5 typical oceanic and 9 coastal spectra. Although this classification scheme is limited by the in-situ data which was available at that time, it still improved the previous methods by quantifying optical properties with the use of in-situ instrumentation.

The augmented interest in optical water-mass classification is due to developments in both biogeochemistry and physics. Quantitative description of the absorption spectra of algal pigments, the development of methods for pigment extraction from environmental samples, and the development of radiative transfer theory laid foundation for the derivation of algorithms to retrieve important optical properties from ocean-colour measurements made from space [Arnone et al., 2004].

Initially, Morel and Prieur [1977] defined two types of waters (Case I and II) by having described the shape of reflectance (the ratio between downwelling and upwelling irradiance) and its spectral changes according to the predominant optical constituents by looking at the ratio between chlorophyll concentration

[1] http://www.eyeonwater.org/

and the scattering coefficient at 550 nm. In recent years, the criterion for distinction has been (over)simplified as whether the variation in colour is dominated by phytoplankton and their associated degradation products [Arnone et al., 2004] or where reflectance ratio algorithms work well to obtain chlorophyll concentration (both Case I). It should be underlined however that waters in the same area may be Case I during some time of the year and Case II in other times or that certain regions with similar chlorophyll may have significant variations in ocean colour in the open ocean environment due to the presence of also other water constituents with different optical signals (e.g. Eastern Mediterranean vs. South Pacific gyre) [Mobley et al., 2010]. Such a distinction is still most commonly used in the scientific literature concerning marine optics despite a more than a decade open appeal by Mobley et al. [2004] to reevaluate classifications due to simplified or elusive interpretations, which might result in misuse and poor algorithm performance.

Instead, multivariate combinations of satellite-derived optical parameters provide a basis for generating unique optical fingerprints for different water masses. An example of such an optical differentiation is the use of ternary diagrams (e.g. Babin et al. [2003]; Bricaud et al. [2004]) by designating a point in a triangle based on the relative contribution of absorption by phytoplankton, non-algal particles, and CDOM to the total absorption (subtracting the contribution of salt water) at a specific wavelength. A point at the triangle's centre indicates equal contribution by all components, while each points at the apex describe waters where all the contribution is dominated by only one water constituent [Mobley et al., 2010].

The major breakthrough in ocean colour studies, which could denominate also the beginning of modern optical oceanography, coincides with the emergence of satellite platforms and the possibility of using information on the ocean colour through remote sensing algorithms. Among various satellite sensors placed in Earth orbit to perform environmental observations, the Coastal Zone Color Scanner (CZCS), which functioned on board the satellite Nimbus-7 from late 1978 to early 1986, has been the main source of the early ocean colour data available for most of the marine regions of the world [Barale and Schlittenhardt, 2012]. It was the first satellite-borne sensor designed to remotely assess the biological productivity of ocean waters by means of the apparent colour of the water. This in turn opened the possibility of mapping the distribution of water constituents over entire basins, trying to establish quantitative relationships between optical properties of surface waters and various biogeochemical and physical parameters (for example: Bricaud et al. [1981, 1987]; Gordon et al. [1988]; Morel [1988]; Morel and Maritorena [2001]; Morel et al. [2007a,b] and many others).

After the unprecedented success of the pioneering sensor, which had 6 bands of 20 nm bandwidth (only 4 of which were used for ocean colour applications), many other multi-spectral sensors have been developed and launched, which generally had a few more bands with narrower bandwidths. The Sea-viewing Wide Field-of-view Sensor (SeaWiFS, 1997-2010, O'Reilly et al. [1998]) had an additional band near 412 nm to improve the detection of colored dissolved organic matter (CDOM), whereas near-IR bands were added for atmospheric correction purposes. Similarly, the MODerate resolution Imaging Spectroradiometer (MODIS, since 2002) has additional bands in the 400-900 nm range, used for clouds, aerosols and atmospheric water vapour detection [Mobley et al., 2010]. In the same year, the European Space Agency (ESA) launched the Medium Resolution Imaging spectrometer (MERIS), which operated for 10 years. Since 2014, ESA has launched a number of Sentinel satellites with the scope of improving the current Earth observation missions and thus enabling a complete and continuous spatial coverage. For ocean colour purposes, the satellites of use are Sentinel-2 (for coastal applications) and especially Sentinel-3, the primary objective of which is marine observation. In order to preserve the heritage of its preceding sensor (MERIS), the Sentinel-3-OLCI sensor kept the original 15 wavelengths with corresponding bandwidths, however upgrading to 6 additional ones. Apart from a number of technical improvements [2], the global ocean coverage is reached in less than 4 days compared to MERIS, which exceeded 15 days. OLCI has also a 100% overlap with the SLSTR sensor for synchronous sea surface temperature (SST) measurements.

Currently, much interest is concentrated on the future use of hyperspectral sensors, such as NASA's PACE OCI sensor with 5 nm resolution from 385 to 770 nm or EnMAP, with 6.5 nm sampling interval between 420 and 1000 nm (scheduled to be launched in 2020 and 2022 respectively). The major advantage of hyperspectral over multispectral sensors will be the possibility to measure contiguous spectral bands, hence covering the whole visible and a portion of the near-IR range.

Although significant progress has been made in the advancement of remote sensing technologies and algorithm refinements, it still remains crucial to validate observations with different in-situ platforms and numerical models. Following the "pace" of the latest agenda in optical oceanography, the near future lies in the hyperspectrality of both measurements and models, conveying a full display of water environment complexities. This will in turn require the revision of currently used relationships between biogeochemical and optical properties and to start considering interdisciplinary approaches by establishing a multilateral network of experts in a number of different, but interrelated

[2] https://sentinel.esa.int/web/sentinel/user-guides/sentinel-3-olci/overview/heritage

fields involving the studies of the Earth's biosphere.

1.2 General Theory

The author would like to acknowledge that the main sources for this chapter are the open-source Ocean Optics Web Book [Mobley et al., 2010] and the literature from the Ocean Optics Class 2017 organized by NASA and the University of Maine. Notes from lectures were corroborated and controlled with the course material, which is publicly accessible on-line [3].

1.2.1 Radiometric Quantities

Spectral radiance $L(z, \theta, \phi, \lambda)$ is the fundamental radiometric quantity of interest in hydrologic optics, depending on zenith and azimuth solar angles, wavelength and depth. Although radiance is an extremely useful concept and is adequate for most needs of optical oceanography, it is an approximation to the exact description of light in terms of electric and magnetic fields. With a known radiance field, however, all other radiometric quantities of interest in oceanography can be derived (upwelling/downwelling planar and scalar irradiances and the photosynthetically available radiation - PAR). Radiometric quantities (or variables) are shown inside the red box in Figure 1.1.

1.2.2 Inherent Optical Properties - IOPs

Natural waters, both fresh and saline, are a complex mixture of dissolved and particulate matter, which are optically significant and highly variable in concentration and composition, thus exhibiting large spatio-temporal variations, seldom resembling those of pure water.

When a photon interacts with matter, two things can occur: the photon's light energy converts to another form, be it heat or chemical bond energy (absorption), or the photon changes direction and/or energy (scattering). The absorption and scattering properties of a medium, such as sea water, are therefore described by its inherent optical properties, or IOPs, which are independent on the ambient light field. The two fundamental IOPs are the absorption coefficient (a) and the volume scattering function (β), from which the total scattering (b) and the backscattering (b_b) coefficients can be obtained. Summing the absorption and scattering coefficients results in the beam attenuation coefficient (c) - see blue box in Figure 1.1.

IOPs depend on the composition (i.e. what materials are the substances made of, which is quantified with the index of refraction n), morphology (size and shape of particles), and concentrations of the particulate and dissolved substances in the ocean, described by the particle size distribution (PSD).

[3] http://misclab.umeoce.maine.edu/OceanOpticsClass2017/

Depending on their distinct spectral shapes, constituents that comprise optically important components to total absorption in the ocean can be generally divided into four major groups:

- water
- phytoplankton
- non-algal particles
- colored dissolved organic matter

Scattering of particles with diverse shapes varies substantially given a same volume and similarly, for a same shape, changing volumes cause different scattering signatures of examined particles. Mobley et al. [2010] describes as an example the atmospheric visibility through rain and fog: despite the possibly equal amount of water in a given volume of air, the smaller particle size of fog drastically decreases visibility due to a different scattering regime. Larger particles are known to scatter strongly at small angles (therefore having a negligible backscattering contribution), whereas small particles (i.e. diameters are smaller than wavelengths) follow the Rayleigh theory, having an equal contribution in all directions.

A fundamental problem of optical oceanography proves to be the understanding of IOP variability as a function of various constituents, ranging for a few orders of magnitude from pure water to turbid coastal water environments (units of m^{-1}). Obtaining robust information on IOPs is essential in radiative transfer theory since, along with boundary conditions (see Section 1.3), serve as the forward model input. In order to retrieve radiances and therefore AOPs, which are described in the section below, it is crucial to obtain an in-depth knowledge on the water properties related to the compositions and concentrations of various biogeochemical substances.

1.2.3 Apparent Optical Properties - AOPs

Apparent optical properties (AOPs, see the green box in Figure 1.1) arise when radiometric quantities other than radiance are used to describe the light field in a water body [Mobley, 1994]. They depend both on the medium (i.e. the IOPs) and on the directional structure of the environmental light field. However, compared to radiometric quantities, they also display enough regular features and stability to be useful descriptors of the water body, therefore, being ratios of radiometric quantities or their depth derivatives, depend more on the IOPs than on the changes in external conditions. They can be generally divided into three major groups: reflectances, average cosines, and diffuse attenuation coefficients, the latter being a common thread in the following chapters.

Remote Sensing Reflectance

In its modern interpretation, the term ocean colour is used to indicate the visible spectrum of upwelling radiance at the sea surface (L_u) or, after having corrected for the atmospheric and surface-reflected (sun and sky glint) contributions [Mobley et al., 2016], water-leaving radiance (L_w), which is related to the presence, nature and abundance of substances dissolved and suspended in the surface layer of the sea by processes of absorption and scattering. Water-leaving radiance L_w divided by downwelling irradiance E_d gives rise to the remote sensing reflectance R_{rs}, the most commonly used AOP for the retrieval of IOPs and biogeochemical variables of interest since, compared to reflectance R (i.e. the ratio between upwelling and downwelling irradiance), it is less sensitive to environmental conditions and relates to the IOPs with a lower degree of uncertainty.

1.3 The Radiative Transfer Theory

Apart from the advancement in satellite remote sensing technologies in the past 40 years, much progress has been done also in the development of the radiative transfer theory, which, through the radiative transfer equation (RTE), connects optical properties of the water body and light within water (see Figure 1.1).

1.3.1 Forward Modelling

Radiative transfer theory provides the connection between IOPs and AOPs.

The physical environment of a water body - surface waves, bottom depth and type, incident radiance from the sky - enters the theory via boundary conditions (see yellow box in Figure 1.1), which are necessary to obtain a solution of the RTE [Mobley et al., 2010].

The RTE derivation is based on quantum electrodynamics (QED), where light is consisted of elementary "excitations" called photons - quanta of the electromagnetic (EM) field (e.g. see Feynman [2006]) by solving Maxwell equations that view light as propagating electric and magnetic fields. A propagating wave solution of Maxwell equations leads to a general vector radiative transfer equation (VRTE) for the Stokes vector, i.e. an array of four real numbers used to fully specify the state of polarization, which refers to the plane in which the electric field vector is oscillating. In oceanography, several assumptions are made in order to simplify the VRTE to a scalar radiative transfer equation (SRTE, shown also in Fig.1.1):

- Scattering particles are randomly oriented and mirror symmetric. The latter usually works well also for phytoplankton of various shapes and

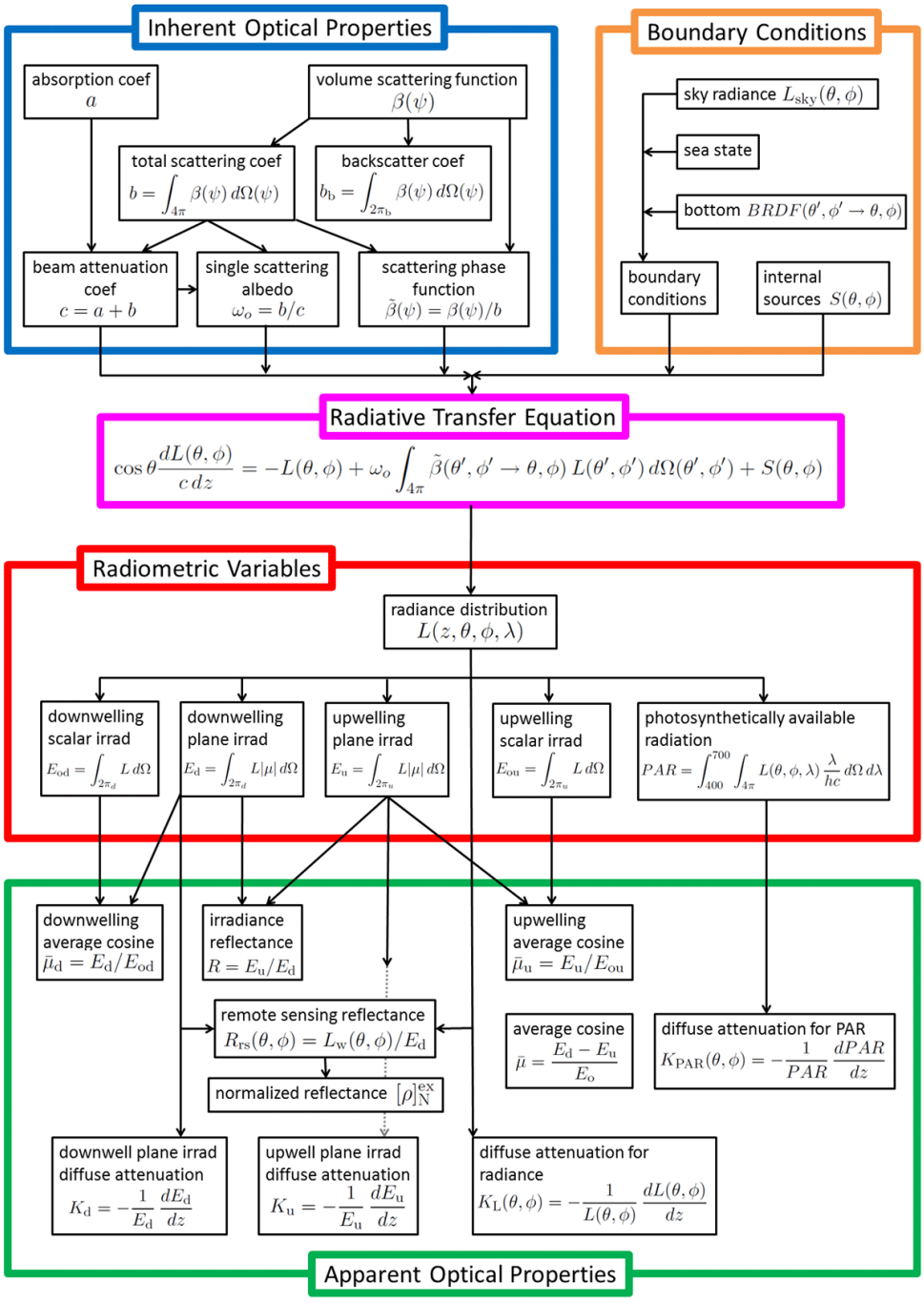

Figure 1.1. Organization chart for optical oceanography [Mobley et al., 2010]

sizes, however some functional groups prove to be exceptions, such as *Chaetoceros*. Assuming an equal number of randomly oriented left- and right-handed helixes allows such a generalization for all phytoplankton species.

- The biggest source of error lies in the assumption that light is unpolarized. It should be noted, however, that polarization carries important information and is increasingly being used to extract environmental footprints via remote sensing, as well as to enhance underwater visibility [Mobley et al., 2010].

Comparison with radiances computed by the VRTE and the SRTE in Hydrolight, the most commonly used radiative transfer numerical model, shows that the difference in calculated radiances is typically around 10%.

The equation can be also derived heuristically, i.e. by looking at it in terms of gains and losses in a small element (see the magenta box in Figure 1.1

- Losses of Radiance:
  - The loss due to absorption and scattering is proportional to the amount of radiance (note that $a + b = c$).
- Sources of Radiance:
  - Elastic scattering into the beam
  - Internal sources of radiance (*de novo*) due to emission (e.g. bioluminescence) or inelastic scattering - each requires a separate formulation, however in this case are shown as a generic source function S

To summarize: given the IOPs, the internal sources and boundary conditions at the air-water surface and the bottom, the radiative transfer model solves the RTE for the radiance distribution $L(z, \theta, \phi, \lambda)$ throughout and leaving the water. It is thus a linear (in the unknown radiance), first-order (only a first derivative) integro-differential equation, which can give only one solution for a given set of conditions and can be generally solved only numerically.

Two solutions of the RTE can be however derived on pen and paper due to a number of simplifications considered: The Lambert-Beer and Gershun's Law.

Analytical solutions: The Lambert-Beer Law

Most biogeochemical models work with the simplified version of the RTE, namely, the Lambert-Beer Law. Despite its straightforward understanding and relatively uncomplicated implementation, it is essential to get a grasp on the assumptions which lead to it. The examined water body is:

- homogeneous (IOPs are independent on depth)
- absent of scattering ($\beta = 0$, thus $b = 0$ or $c = a$)
- without internal sources (i.e. bioluminescence, Raman scattering ...)
- infinitely deep (no bottom reflectance)

Visualizing such an ocean in real life situations would mean that while looking downwards, the water would be completely absorptive and therefore black.

Analytical solutions: Gershun's Law

Gershun's Law is useful to retrieve the absorption coefficient from measured in-water radiances at wavelengths where inelastic scattering is negligible.

This is how irradiance is used in a coupled physical-biological-optical ecosystem model to couple biological variables (which with water determine the absorption coefficient and irradiance) to hydrodynamics (heating of the upper ocean water).

The application of Gershun's Law is used by describing the time rate of change for sea temperature: the rate of water heating depends on how much irradiance there is and on how much of it gets absorbed.

1.3.2 Inversion Modelling

Inversion models experienced a first interest when satellites started being used for the retrieval of biologically important variables, such as chlorophyll *a*. The seminal idea was to relate the water-leaving signal with chlorophyll concentrations. The first algorithm proposed for the CZCS was based on a linear regression of a data set comprised of only 31 points (log-transformed measurements of Chl and water-leaving radiances).

Roughly, inversion models can be divided into empirical and semi-analytical ones, the former being band-ratio algorithms (used in satellite remote sensing) and neural networks, which have in the recent years experienced an increased interest in the community both for remote sensing algorithm refinements as well as for large data set manipulations, such as phytoplankton community size and functional types detection through flow cytometry.

Semi-analytical models emerged from the conclusions that a direct link between chlorophyll *a* and radiances cannot explain fully the optical processes behind it and that information on IOPs is needed instead.

The general idea behind the inverse problem of radiative transfer theory can be summarized as follows: given radiometric measurements of underwater

or water-leaving light fields, determine the inherent optical properties of the water [Mobley et al., 2010]. Even though it is of major interest especially in the satellite remote sensing community, it still remains a rough approximation of the RTE with several caveats:

- solution uniqueness (for different boundary conditions, radiance can change, but not the IOPs - can the inverse model detect same IOPs for different light conditions?)
- sensitivity to errors (small errors in water-leaving radiance retrieval can result in large errors in IOP calculation)

The input measurements from remote sensing contain substantial errors resulting from inadequate atmospheric corrections or wrong sensor calibration. In the visible range, more than 90% of the atmospheric signal due to various sources has to be eliminated in order to obtain water-leaving radiance. A 0.5 % error in atmospheric correction or calibration corresponds to a 5% error in L_w, which can then result in IOPs off for an order of magnitude.

Several approaches have been developed in the last two decades with the aim to overcome the difficulties inherent to such techniques. For a comprehensive overview see IOCCG [2006] and more recently Werdell et al. [2018].

1.4 Coupling Optical with Ecological Models - A Case Study

The theoretical introduction is concluded with a case study described in Mobley et al. [2015] in order to tackle the subject of coupling the radiative transfer model with ecological models. A comparison is shown between a Lamber-Beer Law-based (analytical) irradiance model versus an accurate one (Ecolight-S). Detailed model configurations along with the whole set of equations used are beyond the scope of this section, however it should be underlined that most of the state-of-the-art models seldom incorporate a whole chain-link between hydrodynamics, biology and light as it was done in the present study and as such deserves further consideration. Findings can be summed-up as follows:

1. The use of accurate irradiance gave up to almost 60% differences in chlorophyll concentrations after 2 weeks of simulated time.
2. Accurate irradiance calculations increased the sea surface temperature (SST) and decreased T at depth, leading to an increased stratification, thus impacting the circulation pattern.

3. The use of the accurate irradiance model couples both physical (in the range between 400 and 1000 nm through Gershun's Law) and biological calculations (from 400 to 700 nm) so that biology feeds back to physics and vice versa.

4. EcoLight-S outputs ancillary quantities such as remote sensing reflectance (R_{rs}) and in-water spectral irradiance, which can be used to validate ecosystem predictions using remotely sensed ocean colour imagery or optical measurements from in-situ instrumentation, without the need to convert them to chlorophyll a (though possible).

5. The ecosystem total run time with EcoLight-S was $< 20\%$ more than for the analytical irradiance models.

6. The use of 24h average irradiances gave factor-of-two differences in chlorophyll a concentrations compared to the use of a diel irradiance pattern with the same 24-h average value.

Such studies serve as a current paradigm to ecological modellers and show the directions which will be taken in the upcoming years.

1.5 Bio-Optical Anomalies in the Mediterranean Sea

1.5.1 Introduction

At a global scale, there exist average (empirically derived) relationships between IOPs and biogeochemical variables (such as chlorophyll a (Chl), considered as the main proxy for phytoplankton biomass [Cullen, 1982], or particulate organic carbon (POC)). Certain open ocean areas, however, deviate from the mean of world's oceans and are therefore considered bio-optically anomalous [Mitchell and Holm-Hansen, 1991; Mitchell, 1992; Morel et al., 2007a; Szeto et al., 2011; Huot and Antoine, 2016], which can in turn affect the accuracy of semi-analytical bio-optical models used for the retrieval of biogeochemical variables from ocean (remote sensing) reflectance and can induce large errors on variable estimation.

The possible causes for such phenomenon could be:

- phytoplankton community structure (cell size, pigment packaging, pigment composition, photophysiology), which can affect phytoplankton absorption (a_ϕ) and the particulate backscattering signal (b_{bp})
- Excess/deficit of non-algal (biogenous or mineral) particles (influencing a_{nap} and b_{bp})
- Excess/deficit of CDOM (influencing a_{CDOM})

either separately, or as a combination of several factors.

The Mediterranean Sea is a quasi-enclosed basin which has been extensively studied over the last decades since it is often considered to be "a model of the world ocean itself", despite its size (0.7% of the global ocean's surface and only 0.25% its volume) due to similarities in the processes of dense water formation, as well as in the thermohaline circulation [Lacombe, 1990] and mesoscale eddies [Pinardi and Masetti, 2000]. The region has been historically defined as a Case I optical type, with predominantly oligotrophic waters with Chl concentration rarely exceeding 0.2 $mg\,m^{-3}$, save for the late winter/ early spring blooms in the North-Western Mediterranean [Siokou-Frangou et al., 2010]. Other regions that are associated with higher-than-average Chl concentrations coincide with areas of dense water formation and mesoscale eddies (i.e. the Alboran Sea, Balearic-Catalan Sea, Adriatic Sea and the South Eastern Levantine Sea), or with the coastal areas close to major river discharges (with enhanced nutrient concentrations), such us the Po in the North Adriatic Sea, the Rhone in Gulf of

Lions and the Nile in the Levantine Sea. Another bio-optical specificity is the strong west-east trophic gradient [Bosc et al., 2004; Manca et al., 2004; Lazzari et al., 2012; Tanhua et al., 2013], as well as a noticeable seasonal variability in the western basin [Marty et al., 2002; Bosc et al., 2004; d'Ortenzio and Ribera d'Alcalà, 2009; Lazzari et al., 2012].

The seasonal evolution of Chl distribution follows the typical succession of temperate regions, characterized by a phytoplankton biomass increase in late winter/early spring, a decrease during the summer season and a second smaller phytoplankton bloom in autumn [Siokou-Frangou et al., 2010; Sammartino et al., 2015].

1.5.2 Beginnings

First observations of bio-optical anomalies date back to more than two decades ago, when Gitelson et al. [1996], after having examined a data set from Berman et al. [1984a,b] off the Israeli coast, concluded that the waters of the South-Eastern Mediterranean have an anomalous blue-to-green reflectance ratio when compared to Case I waters with the same pigment concentrations. That was the first example of a regional algorithm proposal in order to derive Chl concentration from the CZCS data in the Southern Mediterranean. In the same paper it was suggested that the anomalous behaviour was due to the abundant presence of small coccolithophorids. Later, D'Ortenzio et al. [2002] observed an overestimation of Chl also in the North-Western Mediterranean and the Ionian Sea, however concluding that the coccolithophorids could explain the anomaly only partially. Similarly, Corsini et al. [2002] proposed a regional algorithm for the Alboran Sea due to an unsatisfactory performance of global relationships, most likely due to the mesoscale features in the subbasin [Viúdez et al., 1998].
All these observations served as first evidences that bio-optical anomalies were present not only in the South-Eastern Mediterranean, but in several other areas of the Western and Eastern basins, mostly during oligotrophic periods.

At the same time, results from the PROSOPE cruise carried out in 1999 and published in Claustre et al. [2002] also showed lower than expected blue-to-green ratio (B/G), most significantly at low Chl concentrations (higher absorption in the blue and scattering in the green), departing drastically from the SeaWiFS OC4v4 algorithm [O'Reilly et al., 1998] for concentrations below 0.4 $mg\,m^{-3}$. In other words, derivation of Chl from B/G measurements through global algorithms can in oligotrophic regions overestimate the actual Chl concentration by a factor exceeding 2. Claustre et al. [2002] hypothesized that such phenomenon results from the Saharan dust deposition (see also Loisel

et al. [2011]). Dust events are episodic, but small, sub-micron particles may accumulate at the upper mixed layer for long periods (i.e. as long as deep convective processes do not occur). It should be noted however that no direct CDOM measurements were taken concomitantly, which could also possibly explain a higher absorption in the blue part of the spectrum. Generally, only few CDOM analyses were carried out for offshore waters of the Mediterranean Sea before the present decade [Kitidis et al., 2006; Bracchini et al., 2010].

From the same cruise data set, Morel et al. [2007a] showed two other kinds of bio-optical anomalies: firstly, through an indirect estimation the occurrence of very high CDOM absorption values at 370 nm ($a_{CDOM}(370)$) and secondly, greater beam attenuation of particulate matter at 555 nm ($c_p(555)$) compared to the global (c_p) vs. Chl relationship from Loisel and Morel [1998], assuming an enhanced content of CDOM in the former and possibly of dust, detrital particles and/or coccolithophores in the latter case.

Such an observed bias in Chl retrieval can have in turn a significant impact in the use of remote sensing (in this case SeaWiFS) global products also in validation and tuning of ecosystem modelling, as well as in data assimilation schemes, thus regional algorithms were proposed with the goal to overcome this issues. Volpe et al. [2007], after having re-examined the two regional models proposed by D'Ortenzio et al. [2002] and Bricaud et al. [2002], introduced a new, MedOCI4 algorithm for SeaWiFS, concluding that the anomalies in the Mediterranean are not due to the atmospheric correction term, but that are most likely caused by a different phytoplankton community structure. Similarly, Santoleri et al. [2008] developed MedOCI4 equivalents for two additional sensors: MODIS and MERIS, underlining that it should be investigated to what extent a different phytoplankton community structure and distribution could alter the spectral signature of the water column.

In order to extend the existing time series beyond that provided by a single satellite sensor, the European Space Agency (ESA) has in the recent years generated the Ocean Colour—Climate Change Initiative (OC-CCI), a multi-sensor, global, ocean-color product, mainly devoted to climate applications [Storm et al., 2013], that merges observations from four different sensors: SeaWiFS, MODIS, MERIS, and VIIRS. The current operational algorithms are an updated version of the one provided by Volpe et al. [2007] (see the Copernicus Marine Environment Monitoring Services (CMEMS) Quality Information Document [Volpe et al., 2017]. The rationale for such a choice most likely stems from the fact that other sensors are band-shifted to match the SeaWiFS wavelengths, which is considered the highest quality sensor with the best match to in-situ observations up to date [Belo Couto et al., 2016].

1.5.3 Past Decade - New Insights

The match-up of satellite-derived reflectances with in-situ observations is crucial to evaluate their quality and temporal stability. To contribute to this effort, the BOUSSOLE buoy has been specifically designed to perform radiometric measurements at sea (in support to satellite ocean colour calibration and validation - see Antoine et al. [2008a]) and also to carry out fundamental studies in marine optics and bio-optics [Antoine et al., 2006]. Apart from integrated radiometers, which measure downwelling and upwelling irradiances (E_d and E_u respectively) as well as upwelling radiances (L_u) at 7 wavelengths, the buoy has additional sensors to measure bio-optical properties, such as the beam attenuation coefficient (c) at 660 nm, Chl fluorescence and the backscattering coefficient (b_b) at two wavelengths (for more details see Antoine et al. [2008b]). Additional acquisitions are complemented by monthly cruises on site.

The BOUSSOLE is located on an area that has been extensively dedicated to frequent measurements since the early 1990s, such as the monthly DYFAMED cruises [Marty et al., 2002], which has collected core data that are made publicly available to the scientific community, including CTD casts, phytoplankton pigments (through high performance liquid chromatography or HPLC, Vidussi et al. [2001]), nutrients, oxygen, dissolved organic carbon (DOC), and primary production from short-time ^{14}C incubations [Antoine et al., 2008a].

Since 2011, a large array of autonomous Biogeochemical-Argo (BGC-Argo) floats has been deployed, measuring a whole set of bio-optical variables [IOCCG, 2011]. Between 2012 and 2016, 105 BGC-Argo floats were distributed on a global scale [Organelli et al., 2017], 31 of which were present in the Mediterranean Sea (see Chapters 2 and 3).

In the past decade, the development of new technologies for the acquisition and analysis of bio-optical variables has brought new insights, but at the same time raised new questions to address, such as the CDOM dynamics, size and composition of algal communities, absorption by phytoplankton (a_ϕ) and non-algal particles (a_{NAP}) and particulate backscattering (b_{bp}).

Colored Dissolved Organic Matter - CDOM

Several case studies started tackling the subject of CDOM spatio-temporal dynamics due to the previous lack of direct measurements. Higher CDOM concentrations relating to Chl were observed on two sites: at the BOUSSOLE during oligotrophic periods (Chl less than 1 $mg\,m^{-3}$) in all seasons except winter [Organelli et al., 2014] and in the Catalan-Balearic Sea, based on data from SUMMER cruises in 2011-2012 (for Chl between 0.04 and 0.1 $mg\,m^{-3}$),

described in Pérez et al. [2016]. Conclusions are generally consistent with the ones stated in Morel and Gentili [2009], i.e. that the dynamics of surface CDOM in Case 1 waters is driven not only by algal biomass, but also (and likely predominantly) by the circulation of water masses and by photochemical processes (see also Xing et al. [2014]).

Similarly, in Organelli et al. [2017], as well as in Chapter 2, an anomalous relationship was observed from a BGC-Argo data set between the biogenic component of diffuse attenuation coefficients for downward planar irradiance (K_{bio}) (at 380 and 412 nm) and Chl, deviating from global algorithms proposed by Morel and Maritorena [2001] and Morel et al. [2007b], thus suggesting an enhanced content of water constituents absorbing in the near-UV, such as CDOM and/or non-algal particles (NAP).

Phytoplankton communities

With the refinement of satellite sensors and the algorithms associated with the retrieval of bio-optical variables, the analysis of ocean colour satellite imagery has allowed to determine the dominant phytoplankton groups in surface waters through the development of bio-optical models aimed at identifying the main phytoplankton functional types (PFTs) or size classes (PSC) from space. This is receiving increasing attention due to the realization that capturing the role of phytoplankton in the global ocean cycles requires improved representation of their complex functionalities [IOCCG, 2014] since such information could indicate environmental anomalies and thus represent changes in ecology. A whole summary of the state-of-the-art algorithms can be found in Mouw et al. [2017].

For this purpose, a regional algorithm for the Mediterranean Sea was proposed by Navarro et al. [2014] and upgraded in Navarro et al. [2017], the PHYSAT-Med, based on the global PHYSAT model introduced by Alvain et al. [2005], which relies on the identification of specific signatures in the normalized water leaving radiance spectra (nL_w), therefore enabling an estimation of five phytoplankton groups (nanoeukaryotes, Prochlorococcus, Synechococcus, diatoms and coccolithophores).

Similarly, Sammartino et al. [2015] in their empirical model (following the method suggested by Brewin et al. [2011]) allow the assessment of spatio-temporal variability for three phytoplankton size classes (pico- (0.2 - 2 µm), nano- (2 - 20 µm) and microphytoplankton (20 - 200 µm), [Sieburth et al., 1978]) during the SeaWiFS operational period (1998-2010).

The model developed by Di Cicco et al. [2017], on the other hand, is able to identify simultaneously the contribution of each of the PSC and PFT group to the satellite estimates of total Chl concentration in the basin, at the same

time improving the uncertainty and spread compared to global models for an order of magnitude for all phytoplankton classes.

Results from all three publications extended the interpretation of previously detected patterns [Siokou-Frangou et al., 2010; Uitz et al., 2012], suggesting a dominance of picophytoplankton throughout the year at the basin level (most abundantly the Prokaryotes), especially during spring and summer months and in oligotrophic environments. Even though picophytoplankton is dominant in most areas, nanophytoplankton is widespread all along the year and over the entire basin (with a peak in winter), accounting for 30 to 40% of the total Chl signal. The models also successfully reproduced diatom blooms in spring, especially in the Adriatic Sea and the North-Western Mediterranean, as well as the presence of Prymnesiophytes in the coastal regions.

Relating to the findings from Gitelson et al. [1996] and D'Ortenzio et al. [2002], Navarro et al. [2017] identified the presence of coccolithophorids in the basin along the Mediterranean coastline and especially in the surroundings of large river mouths (Ebro, Rhone and Nile), as well as in the Adriatic Sea. Di Cicco et al. [2017] on the other hand estimated the contribution of coccolithophorids as 30 to 40% of the total Chl signal.

PFT/PSC estimates from satellite data confirm the significant contribution of nanophytoplankton to total biomass, even in oligotrophic areas, which corresponds to findings in Bricaud et al. [2010] and Organelli et al. [2011], however, much should still be addressed regarding the typical relationships between diagnostic pigments and particle size in the region. One recent example of such a deviation from conventional nomenclatures was published by Leblanc et al. [2018] in a case of massive bloom of small, nanoplanktonic diatoms during a 2013 cruise in the North-Western Mediterranean. Since diatoms are usually attributed to the microphytoplankton group, omitting nanoplanktonic cells' contribution to the carbon export could lead to a critical underestimation of the total carbon budget.

Phytoplankton absorption a_ϕ

Bricaud et al. [1995] and Bricaud et al. [2004] concluded that the phytoplankton absorption coefficients (a_ϕ) tend to increase non-linearly with increasing Chl concentration, resulting both from a decreasing contribution of non-photosynthetic pigments and increasing pigment packaging (larger algal size induces a larger packaging effect and thus lower a_ϕ coefficients [Morel and Bricaud, 1981]).

Organelli et al. [2011] examined 4 sub-regions of the Mediterranean Sea, demonstrating that a higher contribution of photoprotective pigments was present in oligotrophic waters, which could result in lower a_ϕ. It was also noted that the variation in a_ϕ at 443 nm from low to high values towards mesotrophic

regions could be explained by the variations in phytoplankton assemblage main size, concluding that the global relationships need to be re-examined.

Particle backscattering b_{bp}

In the recent work by Barbieux et al. [2018], a higher than global b_{bp} to Chl ratio (with b_{bp} values being higher than average) was observed with measurements from BGC-Argo floats except for the Western basin during spring and the Levantine region during winter, which could be due to an enhanced content of non-algal particles, phytoplankton photoacclimation or to a change in the phytoplankton size community to smaller groups after a microphytoplankton bloom. High absorption of non-algal matter was lastly reported from the MINOS cruise published in Bricaud et al. [1998].

Summary

The occurrence and origins of bio-optical anomalies in the various regions are still far from being clarified. An enhanced concentration of CDOM in the surface layer seems to be confirmed on several sites of the Western and Eastern Mediterranean during oligotrophic periods, however measurements are still sparse. Phytoplankton communities show some specificities, with an enhanced contribution of nanophytoplankton (contributing to up to 30 or 40 % of the total Chl concentration), nonetheless with a constant prevalence of picophytoplankton in oligotrophic regions.

b_{bp} coefficients were reported to be higher than expected (most likely suggesting a high amount of biogenous detritus and/or dusts) in most investigated regions, but not in all seasons. Recent reports have still not clarified to what extent the enhanced absorption in the near-UV/blue part of the spectrum can be attributed to CDOM and NAP, lacking concomitant measurements and techniques to differentiate the backscattering signal from organic and inorganic substances.

The underlying causes for bio-optical anomalies in the Mediterranean Sea still remain far from clarified, and their spatial and seasonal variability remains to be further documented. However, with the development of new technologies (e.g. BGC-Argo), as well as with the tendency to make data from HPLC [Buitenhuis et al., 2013] and other bio-optical data sets from various sources [Valente et al., 2016] openly accessible to the whole scientific community, enables new, interdisciplinary ways to integrate in-situ data with satellites and ecological models, which is also the final aim of this thesis, hoping to shed a light on one of the possible methods of merging various approaches. The author's scope of this introduction is to underline that still much work has to

be done and that the present study is still far from a full disclosure of possible connections between physics, biogeochemistry and bio-optics in the region.

Chapter 2

Kd coefficients in the Mediterranean Sea: Data Analysis

Abstract

In the present chapter, a Biogeochemical-Argo data set comprised of 31 floats for the period between 2012 and 2016 in the Mediterranean Sea was investigated. The quality-checked profiles of downward planar irradiance (E_d) at three different wavelengths (λ = 380, 412 and 490 nm) and of photosynthetically active radiation (PAR) were used to obtain their depth derivatives - the diffuse attenuation coefficients (K_d). With fluorescence-derived chlorophyll *a* profiles, deep chlorophyll maximum gradients were confirmed, indicating different trophic regimes between eastern and western subbasins. A spatio-temporal analysis of K_d values enabled to further confirm the presence of longitudinal gradients in terms of apparent optical properties, suggesting an enhanced content of highly absorptive substances in the blue part of the spectrum. A comparison was made with a state-of-the-art bio-optical hyperspectral model, linking K_d functions with chlorophyll *a* concentrations, in order to ascertain the adequacy of taking the latter as a proxy for all biogenic components, merging impacts of phytoplankton, particulate and colored dissolved organic matter (CDOM) in only one term, therefore classifying the basin as a Case I water optical type. The use of such relatively simple bio-optical models was extended from the first optical depth to 150 meters, exploring the possibility to use such algorithms beyond satellite remote sensing applications. Due to the biogeochemically complex nature of the Mediterranean Sea, it is debatable whether the enhanced content of CDOM in the region and its high absorption in the near-UV/blue range might increasingly contribute to the light attenuation in the blue part of the spectrum and whether could be therefore correctly quantified within the chlorophyll *a* concentration term. Similarly, the possibility of describing $K_d(PAR)$ with $K_d(490)$ is explored, which could enable a new modelling parametrization described in Chapter 4. Moreover, both K_d functions, as well as Chl profiles, are discussed as possible validation tools in different model settings (used in Chapters 3 and 4), or as an additional method to compare satellite remote sensing products, such as $K_d(490)$.

2.1 Introduction

The emergence of first satellite remote sensing platforms, which were particularly aimed at the retrieval of biogeochemical and bio-optical properties from the water-leaving radiance signal, started in the late 70s with the launch of the Coastal Zone Colour Scanner (CZCS). This in turn aroused interest in the

optical community to explore possible empirical relationships between biogeochemical variables (especially chlorophyll a, which is a proxy for phytoplankton biomass [Cullen, 1982]), and the optical properties of the material dissolved or suspended in seawater [Morel and Prieur, 1977; Gordon et al., 1988; Morel, 1988]. The studies aimed at examining the variability of ocean colour according to the predominant optical constituents that affected the water-leaving signal. This in turn lead to a new classification of two optical water types, known as Case I and Case II waters [Morel and Prieur, 1977], which has still been most commonly used in the scientific literature [Barale and Schlittenhardt, 2012] despite its limitations [Mobley et al., 2004]. Case I waters were described as water bodies for which the inherent optical properties or IOPs (most commonly divided into colored dissolved organic matter (CDOM), non-algal particles (NAP) and accessory phytoplankton pigments) co-vary with phytoplankton and hence with chlorophyll a (Chl) concentration [Lee and Hu, 2006; Antoine et al., 2014]. Case II waters, on the other hand, denote all other water environments, for which the IOPs vary independently of Chl. Since the initial goal of the paper was not to introduce a new optical classification, but rather to provide a framework for conceptual measurements of reflectances [Antoine et al., 2014], further studies focused on refining the concept [Morel, 1988; Morel and Maritorena, 2001]. 20 years after the seminal paper of Morel and Prieur, the first empirical relationships proposed could be further re-examined due to the development and wider use of more accurate techniques for pigment detection, such as the high performance liquid chromatography (HPLC, Vidussi et al. [2001]). With this aim, Morel and Maritorena [2001] focused on the assessment of spectral diffuse attenuation coefficients for downward planar irradiance, K_d, and Chl concentrations, by having re-evaluated the relationships obtained in Morel [1988]. K_d values in the (near-)UV and visible parts of the spectrum were used to assess the variations in light absorption by CDOM, NAP and Chl at global scales and have therefore been denoted as robust optical proxies for Chl and CDOM concentrations [Morel and Maritorena, 2001; Morel et al., 2007b,a]. Such a rationale stems from the fact that in homogeneous water bodies with negligible inelastic scattering processes, K_d co-varies with total absorption a [Mobley et al., 2010]. Thus, with some errors, apparent optical properties, such as K_d, could tell us something on the absorbing constituents of the examined basin.

As previously described in Chapter 1, the Mediterranean Sea has proven to be a bio-optical anomalous region, i.e. global relationships tend to be insufficiently accurate for the retrieval of certain bio-optical and biogeochemical parameters. The main causes for such behaviour could stem from:

- Enhanced concentration of CDOM [Morel et al., 2007a; Morel and Gentili,

2009; Xing et al., 2011; Organelli et al., 2014; Xing et al., 2014; Pérez et al., 2016]

- Enhanced concentration of NAP through the occurrence of Saharan dust deposition [Claustre et al., 2002]
- Phytoplankton pigment packaging [Morel and Bricaud, 1981; Bricaud et al., 1995, 1998]
- Excess or shortage of accessory phytoplankton pigments [Bricaud et al., 2004, 2010]

Relating to the present study, Morel et al. [2007a] observed that global relationships between K_d at 490 nm and Chl proposed in Morel and Maritorena [2001] worked well for two quite different environments, such as the Mediterranean Sea and the South Pacific Ocean. On the other hand, K_d in the UV wavelengths deviated most notably from global algorithms [Morel et al., 2007a] in the Mediterranean Sea, attributing such a divergent behaviour to an enhanced content of CDOM, which was in the next years corroborated by Morel and Gentili [2009]; Xing et al. [2011]; Organelli et al. [2014]; Xing et al. [2014]; Sempere et al. [2015]; Pérez et al. [2016]; Catalá et al. [2018].

Such bio-optical anomalies can in turn cause vast uncertainties in the global remote sensing inversion algorithms (i.e. retrieving IOPs from apparent optical properties or AOPs), thus regional models started being developed in order to improve the algorithm performances [D'Ortenzio et al., 2002; Bricaud et al., 2002; Volpe et al., 2007; Santoleri et al., 2008] and as such should be validated with in-situ ground truth and possibly numerical models.

With this in mind, the optical community has in the past 6 years deployed a high number of autonomous profiling instruments, the Biogeochemical Argo (BGC-Argo) floats, derived as an extension of the Argo programme, which was first launched in 1999 and was primarily focused only on the retrieval of physical variables, such as temperature (T) and salinity (S). Such platforms allow a more refined vertical resolution of examined properties, as well as a quasi-real time acquisition in spatio-temporally inaccessible areas with different trophic regimes. The aim of BGC-Argo has been to expand the set of measured properties to bio-optical and biogeochemical ones [IOCCG, 2011; Johnson and Claustre, 2016], such as downward planar irradiance (E_d) at different wavelengths (380, 412 and 490 nm), the photosynthetically active radiation (PAR), chlorophyll a concentration derived from fluorescence (hereafter Chl), dissolved oxygen, the fluorescent fraction of the dissolved organic matter (FDOM), the backscattering coefficient of particulate matter (b_{bp}) at 700 nm etc. A widened selection of measured properties and an enhanced frequency of their measurements have made possible to start working on a more detailed reconstruction

of the underwater light field and reassess the previously established global relationships on a regional scale.

2.2 Data Set Description

31 floats were acquired for the period between 2012 and 2016 for the Mediterranean basin, with 1314 profiles of T and S (not quality checked), Chl concentration (units of $mg\,m^{-3}$) derived from fluorescence, and radiometric quantities, such as downward planar irradiance (E_d) at three different wavelengths ($\lambda =$ 380, 412 and 490 nm, units of $\mu\,W\,cm^{-2}\,nm^{-1}$) and the photosynthetically active radiation (PAR, unit of $\mu\,mol\,quanta\,m^{-2}\,s^{-1}$), which gives us information on the penetration of light for the whole photosynthetic band - from 400 to 700 nm [Kirk, 1994]. Tracking periods and positions (start-end) for each float are presented in section 2.5 Data acquisition had nominally a 10 m vertical resolution between 250 and 1000 m, 1 m from 10 to 250 m, increasing to 0.20 m from 10 m to the surface [Organelli et al., 2016]. Each cast started from 1000 m parking depth at an adequate time in order to reach the surface around local noon (with a time window of two hours).

According to the spatial partition, which is used also for the Copernicus Marine Environment Monitoring Services (CMEMS), profiles were present in 13 out of 16 subbasins (Figure 2.1), with the majority in the North Western Mediterranean (332), followed by Northern Ionian (172) and Southern Tyrrhenian (162). No data were available for the Southern Ionian, Northern Tyrrhenian and the Eastern Levantine. 7 profiles were present in the Northern Adriatic and only one in the Western Levantine (see Table 2.1).

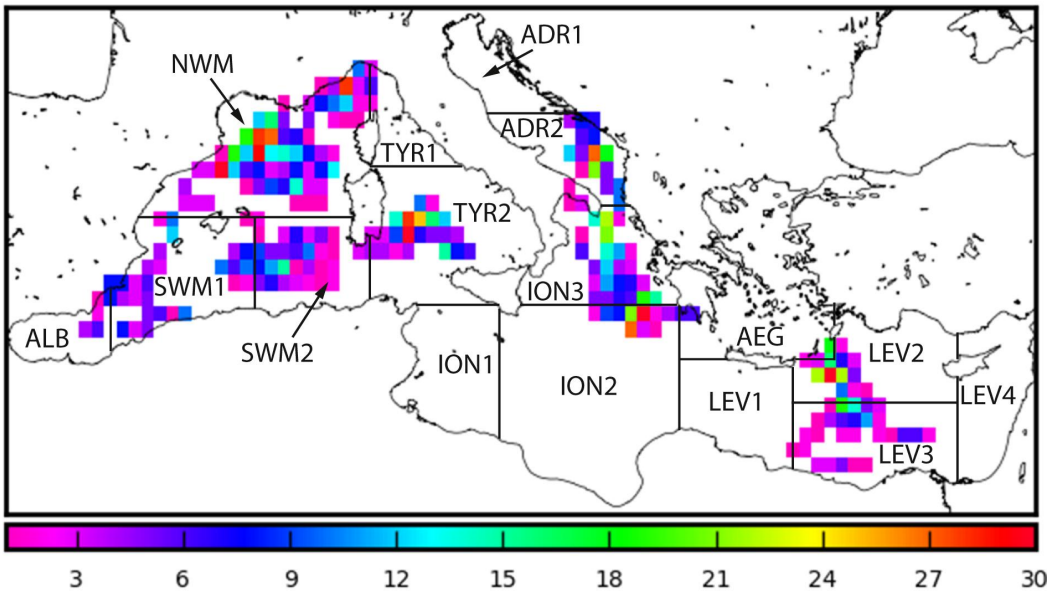

Figure 2.1. Spatial distribution of float profiles superimposed to the subbasin partition used in the Mediterranean CMEMS system.

Table 2.1. Subbasin division - abbreviations and number of profiles.

No.	Subbasin	Abbreviation	Profiles
1	Aegean Sea	AEG	23
2	Alboran Sea	ALB	28
3	South Western Mediterranean west	SWM1	108
4	South Western Mediterranean east	SWM2	77
5	North Western Mediterranean	NWM	332
6	Northern Tyrrhenian	TYR1	/
7	Southern Tyrrhenian	TYR2	162
8	Western Ionian	ION1	/
9	Eastern Ionian	ION2	104
10	Northern Ionian	ION3	170
11	Northern Adriatic	ADR1	7
12	Southern Adriatic	ADR2	131
13	Western Levantine	LEV1	1
14	Northern Levantine	LEV2	83
15	Southern Levantine	LEV3	88
16	Eastern Levantine	LEV4	/

2.2.1 Light and Radiometry

The quality control procedure of radiometric quantities (i.e. downward planar irradiances) consisted of dark signal and cloud identification, wave focusing and spikes correction [Organelli et al., 2016]. Radiometric measurements are available for the depth range between the surface and 250 m.

The diffuse attenuation coefficient for downward planar irradiance K_d is defined as the vertical gradient of the natural logarithm of the downward planar irradiance E_d [Xing et al., 2011].

$$K_d(z,\lambda) = -\frac{d[ln(E_d(z,\lambda)]}{dz} = -\frac{1}{E_d(z,\lambda)}\frac{dE_d(z,\lambda)}{dz(\lambda)} \tag{2.1}$$

K_d - methodology

Originally, Morel [1988]; Morel and Maritorena [2001]; Morel et al. [2007b] applied the studies to the first optical depth (hereafter z_{od}), which is the layer of interest for satellite remote sensing applications [Gordon and McCluney, 1975]. According to Morel [1988], z_{od} is equal to $z_{eu}/4.6$, corresponding to an e-folding reduction of the surface irradiance value. z_{eu} represents the euphotic depth, which corresponds to the attenuation of downward planar irradiance to 1% of the subsurface value [Kirk, 1994].

The first part of the study follows the same methodology with the additional aim to use such data also in Chapter 4 in order to compare satellite-derived K_d functions with in-situ values at the corresponding locations and periods. K_d values were obtained trough the non-linear least squares curve-fitting approach. For validation purposes, Chl was calculated as a mean value for these layers. The range of z_{od} spans from 13 to 32 meters, which is in agreement with the estimates made by d'Ortenzio and Ribera d'Alcalà [2009].

Due to the use of K_d in Chapter 3 in a 1-dimensional modelling configuration, an interest in depth variability was also taken into consideration. In this case, K_d functions were calculated as the local slopes of $\ln(E_d)$ for layers of 15 m for the euphotic depth range (z_{eu}). The choice of 15 m stems from the fact that, despite the quality control procedures, irradiance profiles still retain a noisy behaviour and the calculation of their depth derivative stabilizes when increasing layers (dz).

A note on optical depths

Definitions of optical depths often remain elusive or somewhat contradictory and in many publications are not very well explained, thus the issue requires

further attention with a brief explanation, which will hopefully make the subject clear.

In homogeneous waters (i.e. IOPs are constant with depth), the downward planar irradiance E_d can be written as an exponential function changing with depth, following the Lambert-Beer law:

$$E_d(z,\lambda) = E_d(0-,\lambda)e^{-K_d z} \tag{2.2}$$

where $E_d(0-,\lambda)$ represents the subsurface irradiance value. The optical depth ζ (dimensionless) is thus defined as the product of K_d and z, written in the following equation:

$$\zeta = K_d z \tag{2.3}$$

As mentioned in the previous paragraph, z_{eu} corresponds to the attenuation of E_d to 1% of the subsurface value $E_d(0-,\lambda)$. The equation 2.2 thus changes as:

$$E_d(z_{eu},\lambda) = 0.01E_d(0-,\lambda) = E_d(0-,\lambda)e^{-K_d z_{eu}} \tag{2.4}$$

or :

$$ln(0.01) = -K_d z_{eu} = -4.6 \tag{2.5}$$

For high K_d values in turbid waters (e.g. $K_d = 0.2\ m^{-1}$), z_{eu} will be equal to 23 m, whereas in clear water environments (e.g. $K_d = 0.05\ m^{-1}$), z_{eu} will increase towards 92 m.

The first optical depth z_{od} corresponds to $\zeta = 1$ (and following the same rationale, the second optical depth is equal to $\zeta = 2$, etc.), which means:

$$ln(1/e) = -K_d z_{od} = -1 \tag{2.6}$$

z_{od} is therefore equal to the depth where $z = 1/K_d$, hence, where irradiance drops to 1/e (36.76%) of its surface value. By using eq. 2.5 in eq. 2.6, the final version can be written as:

$$z_{od} = z_{eu}/4.6. \tag{2.7}$$

First optical depths from previous cases would be therefore estimated as 5.75 m for $K_d = 0.2\ m^{-1}$ and 20 for $K_d = 0.05\ m^{-1}$.

Relating to [Gordon and McCluney, 1975], their seminal paper defined the penetration depth of light in the sea for remote sensing purposes as the depth above which 90% of the diffusely reflected irradiance (excluding specular reflectance) originates (z_{90}). Following the procedure described above, such

depth would in homogeneous water bodies correspond to -ln(0.1)/K_d or 2.3/K_d, which is also defined as the mid-point of the euphotic zone [Kirk, 1994].

However, by assuming an axisymmetric (azimuthally homogeneous) radiance distribution and a quasi-single scattering approximation (QSSA, Gordon [1973]), Gordon and McCluney [1975] defined the penetration depth as $1/K_d$, which in the light of previous assumptions (i.e. homogeneous waters) corresponds to the depth at which the downwelling in-water irradiance falls to 1/e (or almost 37%) of its surface value.

To summarize: Gordon through more sophisticated approximations defined as z_{90} what in homogeneous water bodies would correspond to z_{od}, the main difference being that, in his definition, the layer actually contains 90% of the originating irradiance (compared to 63% in homogeneous waters) due to the QSSA.

The scope of this theoretical digression was to emphasize the importance of knowing the underlying assumptions behind the derivation of a commonly used parameter, such as the first optical depth. In this chapter, equations for a homogeneous water body are accepted in order to stay in line with the reference models described in Morel and Maritorena [2001] and Morel et al. [2007b].

2.2.2 Fluorescence-derived Chlorophyll

In BGC-Argo floats, Chl concentration is measured indirectly through its fluorescent property, i.e. the portion of light absorbed by a phytoplankton cell can be emitted at another - longer wavelength. The instrument's excitation/emission wavelengths correspond 470 and 695 nm respectively. Phytoplankton fluorescence is a complex function of the quantum yield (i.e. emission efficiency) and the Chl-specific absorption coefficient (i.e. the Chl absorption coefficient normalized with Chl concentration), both of which depend on numerous factors: phytoplankton taxonomic composition, pigment content and ratios, photoadaptation, phytoplankton physiology, nutrient conditions and stage of growth [Babin, 2008; Mobley et al., 2010].

The quality control of Chl followed the procedures from Schmechtig et al. [2014], i.e. the identification of negative spikes, adjustment of non-zero dark values, verification of the range of measured values according to the instrument manufacturer. Non-photochemical quenching (NPQ) is a photoprotective mechanism [Kiefer, 1973], regulating photosynthesis in environments where light energy absorption exceeds the capacity of light utilization. Following Xing et al. [2012a], a correction for NPQ was also applied by extrapolating the values of maximum fluorescence within the mixed-layer depth (MLD, de Boyer Montégut et al. [2004]) towards the surface. Due to a factory

calibration bias, Roesler et al. [2017] published a recommendation to divide the fluorescence-derived (quality-controlled) Chl value by a factor of 2, which was obtained by a global comparison between fluorescence and HPLC data, as well as with the in-situ radiometry absorption line height retrieval (see Boss et al. [2007] or Roesler and Barnard [2013]).

For the purpose of a simultaneous analysis of all 7 available variables, the entire BGC-Argo data set was vertically interpolated to a resolution of 1 m for 250 m depth.

2.2.3 K_d model

The ample data set of BGC-Argo floats enabled a revision of the relationships between diffuse attenuation coefficients and Chl concentrations, firstly proposed by [Morel and Maritorena, 2001].

K_d is considered as a sum of K_w (pure water contribution) and K_{bio} (a term merging the contributions of all biogenic components). Regression analyses were performed for all wavelengths between 400 and 700 nm at a 5 nm frequency, on the log-transformed quantities, Chl and ($K_d(\lambda)$ - $K_w(\lambda)$), the latter representing K_{bio}, expressed with the empirical equation 2.8:

$$K_{bio}(\lambda) = \chi(\lambda) \cdot [Chl]^{e(\lambda)} \tag{2.8}$$

where $\chi(\lambda)$ (units of $m^2\, mg^{-1}$) and $e(\lambda)$ (unitless) denote the wavelength-dependent constant and exponent respectively.

With an increased number of field data the updated statistical study ("LOV data" in Morel et al. [2007b]) led to a slightly modified relationship for 412 and 490 nm (see Xing et al. [2011], eq. (8a) and (8b)).

The regression model has been used in such way that the Chl values from BGC-Argo floats were implemented in the equations for K_{bio} at all three available wavelengths.

Additionally, the relationship between $K_d(490)$ and $K_d(PAR)$ from Morel et al. [2007b] was also examined in order to provide possible parametrizations of $K_d(PAR)$ values in Chapter 4.

2.3 Results and Discussion

2.3.1 Surface gradients of Chl and K_d

One of the Mediterranean Sea specificities is a strong east-west trophic gradient, which has been observed both by in-situ measurements and numerical models [Bosc et al., 2004; Manca et al., 2004; Lazzari et al., 2012; Tanhua et al.,

2013]. With surface maps, gradients can be confirmed both from Chl and K_d data calculated for the first optical depth (i.e. as seen by satellites). Figure 2.2 shows a significant eastward decrease in mean concentrations, ranging from more than 0.5 $mg\,m^{-3}$ (higher values are observed in the North Western Mediterranean, exceeding 1 $mg\,m^{-3}$ - not shown in this image due to the preservation of medium-range values visibility) to less than 0.1 $mg\,m^{-3}$ in the Levantine region.

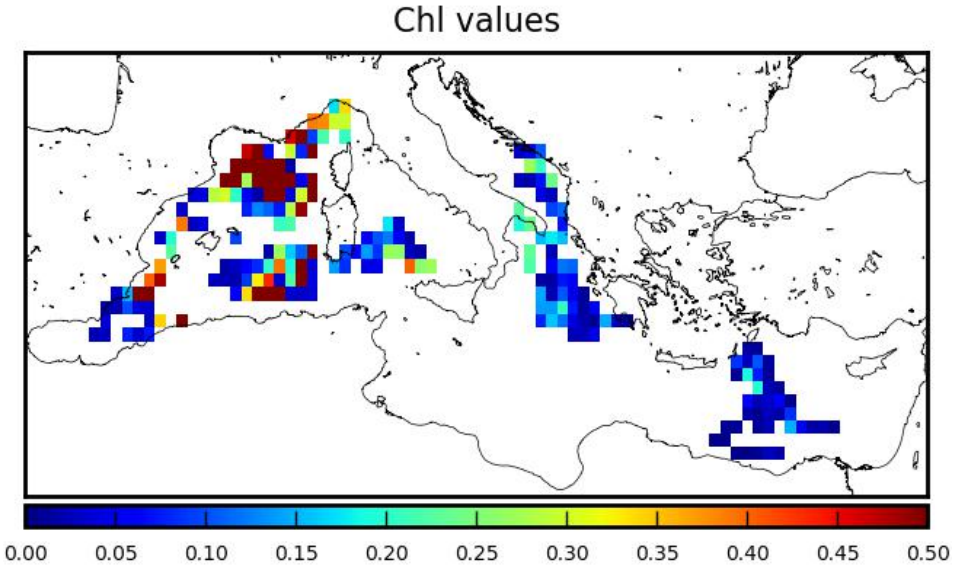

Figure 2.2. Spatial distribution of Chl values (units of $mg\,m^{-3}$) for the first optical depth z_{od}, data extracted from the BGC-Argo data set.

Following the same pattern, maps of K_d values at all three wavelengths (λ = 380, 412 and 490 nm respectively) and for PAR are depicted in Figure 2.3. All maps show similarly as the Chl map in Figure 2.2 a distinct variability comparing western and eastern profiles. Highest values are observed for $K_d(380)$ (up to 0.20 m^{-1}), following a systematic decrease with increasing wavelength. In the validation section, a seasonal analysis is considered to gain additional insights on temporal variability.

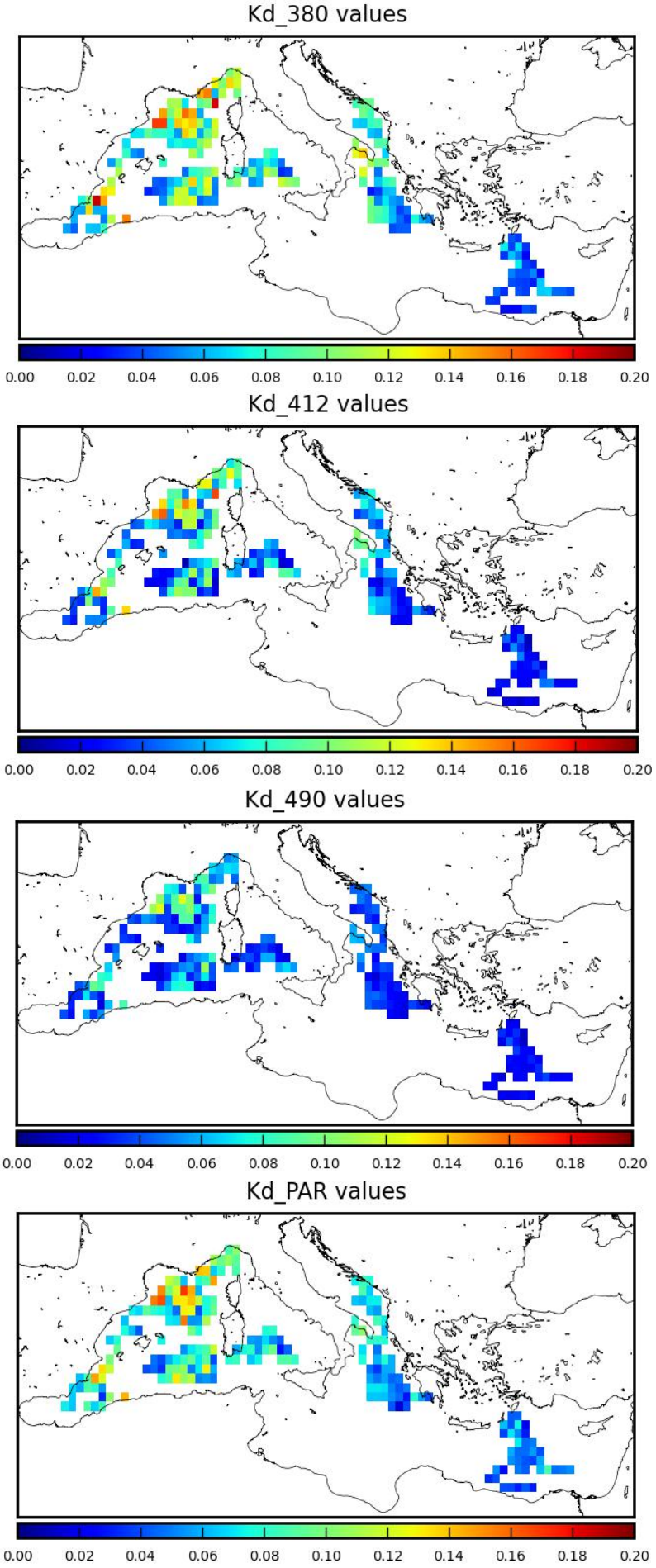

Figure 2.3. Spatial distribution of K_d values (units of m^{-1}) for the first optical depth z_{od}, data extracted from the BGC-Argo data set.

2.3.2 Deep chlorophyll maximum (DCM) gradients

The analysis introduced in the previous section is expanded towards deeper layers, taking the deep chlorophyll maximum (DCM) as another indicator of possible biogeochemical gradients. DCM is an ubiquitous feature in oligotrophic environments and between spring and autumn in the Mediterranean Sea [Siokou-Frangou et al., 2010], displaying a longitudinal deepening from west to east, as well as latitudinally from north to south (see Lazzari et al. [2012]). Oligotrophic environments, such as the Eastern Mediterranean, are characterized by deep DCM and nitracline, which are concomitantly associated with lower Chl concentrations and primary productivity [Estrada et al., 1993], contrary to the areas with higher biological activity (such as the Ligurian Sea), which display shallower DCM with higher values of Chl.

DCM depths and values were calculated following the criteria used also in Chapters 3 and 4:

- DCM should be deeper than 40 m and shallower than 200 m
- Chl concentration at DCM should exceed 0.1 $mg\,m^{-3}$

Cases of subsurface maxima (at depths shallower than 10 m, as reported in Marty et al. [2002] and Manca et al. [2004]) were in this analysis disregarded, since such features are present only during spring blooms in the North-Western Mediterranean.

It should be underlined however that 249 profiles were omitted due to DCM values shallower than 40 m, mostly in the Western basin, which in periods between late spring and early autumn display shallower DCM depths (30 m on average, which is in agreement with values reported in Dolan et al. [2002]). For the sake of consistency, the condition for depths larger than 40 m is kept throughout this thesis, keeping in mind that it should need further revision of the criteria defining DCM.

4 profiles had Chl values at DCM lower than 0.1 $mg\,m^{-3}$, resulting in 1061 profiles taken into consideration for the DCM spatio-temporal analysis.

Results from the BGC-Argo data set are shown in Figures 2.4 and 2.5 (DCM depth and Chl magnitudes respectively). Profiles were present in 13 subbasins from Figure 2.1 and seasonally divided with winter from January to March, following the next seasons with consecutive groups of 3 months. Note however that not all regions had evenly distributed measurements in terms of temporal scales, thus some basins might result in having more profiles during a particular season or else lack them in others. For more details about the seasonal division of profiles per subbasin see Table 2.2.

Table 2.2. Seasonal distribution of profiles per subbasin.

Subbasin	Abbr.	Winter	Spring	Summer	Autumn
Aegean Sea	AEG	/	15	8	/
Alboran Sea	ALB	/	20	8	/
SW Med West	SWM1	28	19	35	26
SW Med Eeast	SWM2	33	17	12	15
NW Med	NWM	102	104	57	69
Southern Tyrrhenian	TYR2	45	50	40	27
Eastern Ionian	ION2	23	47	21	13
Northern Ionian	ION3	48	39	42	41
Northern Adriatic	ADR1	1	6	/	/
Southern Adriatic	ADR2	24	70	28	9
Western Levantine	LEV1	/	1	/	/
Northern Levantine	LEV2	23	4	43	13
Southern Levantine	LEV3	7	43	33	5
Total	MED	335	434	327	218

As shown in Figures 2.4 and 2.5, the DCM feature generally disappears in winter (except for two cases in the Eastern Mediterranean), giving way to a well mixed shape with more constant Chl values along the mixed layer depth (MLD) [Marty et al., 2002; Mignot et al., 2014].

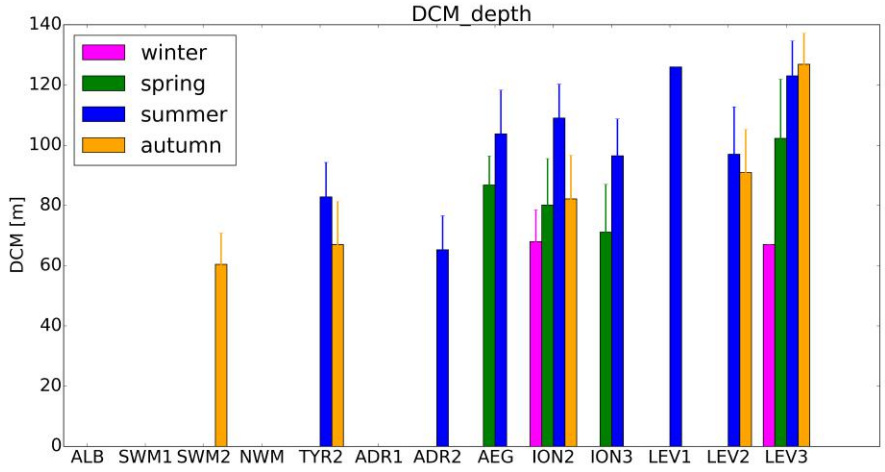

Figure 2.4. Spatial and seasonal values of DCM depth (mean and standard deviation, units of m) from the BGC-Argo data set.

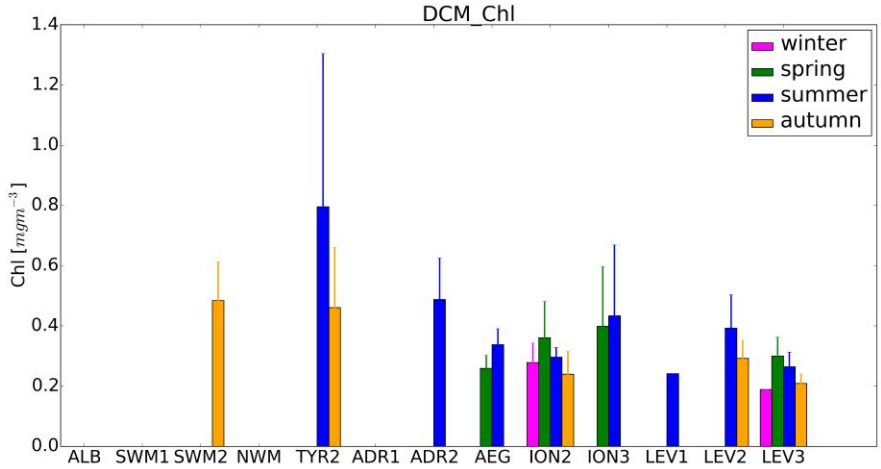

Figure 2.5. Spatial and seasonal values of Chl values at DCM depth (mean and standard deviation, units of $mg\,m^{-3}$) from the BGC-Argo data set.

DCM depths are ranging from 60 m in the South-Western Mediterranean / 70 m in the Southern Adriatic (as in Boldrin et al. [2002]) to 130 m in the Southern Levantine (in agreement with findings in Christaki et al. [2001] and Dolan et al. [2002]). The increase in DCM depth can be observed from Western to Eastern basins, followed by a decrease in mean Chl concentrations (0.8 $mg\,m^{-3}$ in the Southern Tyrrhenian with a standard deviation of 0.6 $mg\,m^{-3}$ and 0.2 $mg\,m^{-3}$ in the Southern Levantine).

According to Siokou-Frangou et al. [2010], such a trend is most likely related to lower productivity and hence higher seawater transparency in the Levantine Sea, which could be already seen by observing the spatio-temporal variability of surface Chl in Figure 2.2.

Moreover, by analysing K_d functions (Figure 2.3), which represent one of the apparent optical properties (AOPs), it is possible to deduce the IOPs that most likely affect such patterns.

According to Gordon [1989], K_d is proportional to both the absorption and backscattering coefficients (a and b_b respectively) and inversely proportional to the average cosine of downwelling irradiance μ_d, which is the ratio between scalar and planar downwelling irradiance. Backscattering is typically only a few percent of the total absorption coefficient, except in extremely clear waters where it may occasionally reach 25% in the blue-violet region of the light spectrum (i.e. when backscattering by water molecules becomes the dominant process, Morel et al. [2007a]). Thus with a certain degree of error and in the absence of scattering data, K_d can be related to absorption coefficients, although

it should be underlined that there are several previous studies that indicate a significant (higher-than-average) scattering contribution in the Mediterranean Sea by Saharan sub-micron particles [Claustre et al., 2002; Loisel et al., 2011], coccolithophorids [Gitelson et al., 1996; D'Ortenzio et al., 2002] or both [Morel et al., 2007a].

2.3.3 K_d Validation - Float Data and Model Comparison

K_d spatio-temporal variability

Figure 2.6 shows a spatio-temporal division of mean values per subbasin with the corresponding standard deviations.

By firstly comparing the four bar plots, as previously shown in Figure 2.3, all figures demonstrate that the east-west dichotomy holds true especially for winter and spring months with lower gradients during autumn, which are less noticeable in summer. The Northern Ionian subbasin however proves to be an exception due to higher-than-average CDOM concentrations, which in turn invalidate the gradient by causing higher K_d values at shorter wavelengths.

Highest values are spotted in winter and spring months in the Western basins, with a maximum in the North West Mediterranean during spring ($K_d(380)$ approaching 0.15 m^{-1}, decreasing to 0.10 m^{-1} at 490 nm). Minimum values are in all cases during summer months (excluding the Alboran Sea, which has only 15 profiles in summer and 8 in autumn), with values around 0.05 m^{-1} at 380 nm, decreasing towards 0.02 m^{-1} at 490 nm for Western basins and similarly from 0.04 m^{-1} to 0.02 in eastern regions.

In Xing et al. [2011], $K_d(412)$ is used to get independent estimates of Chl concentration and CDOM absorption. The diminishing values during summer, supported by observations in Xing et al. [2011], could be due to photobleaching in the surface layer. During the winter vertical mixing period, a spring bloom of phytoplankton is triggered with a concomitant convective transport of CDOM from deeper layers, which is unbleached.

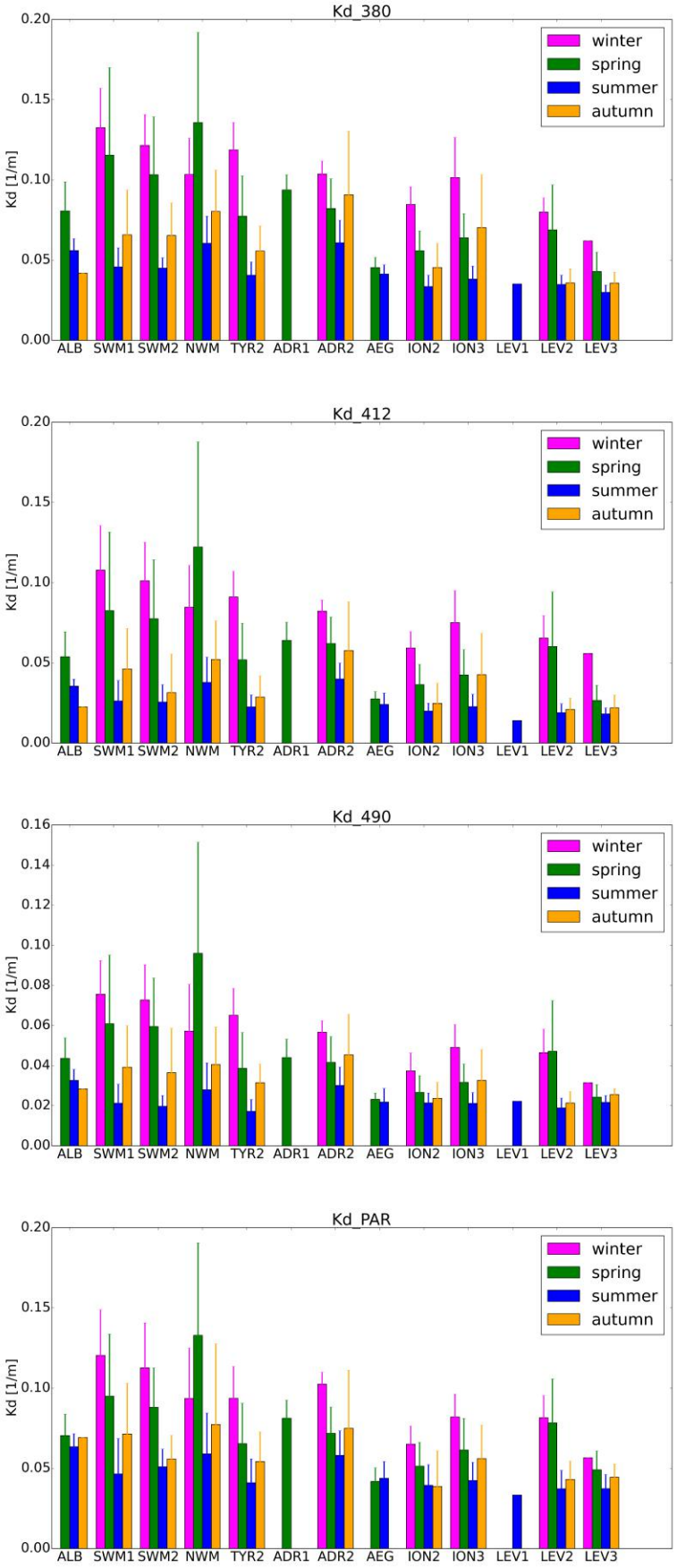

Figure 2.6. Spatial and seasonal values of K_d values (units of m^{-1}) for the first optical depth z_{od}.

K_d model for the first optical depth

Following equation 2.8, regressions were performed for the present data set with values shown in Table 2.3:

Table 2.3. K_{bio} exponential regression analyses for the first optical depth z_{od}.

Case	N	λ								
_	_	380			412			490		
_	_	R^2	χ	e	R^2	χ	e	R^2	χ	e
Morel 2001	_	_	0.127	0.685	_	0.1229	0.6533	_	0.0724	0.6896
Morel 2007	_	_	_	_	_	0.1333	0.6199	_	0.0825	0.6529
BGC-Argo	1315	0.81	0.1377	0.3406	0.86	0.1276	0.4400	0.84	0.0084	0.5713

The standard deviation (not shown) is modified by a Student's t-value (with a 95% confidence interval), which accounts for the additional uncertainty in the estimates due to the small number of data points. The coefficient of variance (CV) is calculated as the ratio between the standard deviation and the mean values (in %). For χ, CV ranges between 1.5% and 1.7%, whereas for the exponent e, it results in values between 2.1 % and 2.5 %, both being smallest for 412 nm, when also the correlation coefficient (R^2) is highest (0.86).

Figure 2.7 shows scatter plots between BGC-Argo K_d values and the regression analysis carried out at separate wavelengths. Results from the original bio-optical models (Morel and Maritorena [2001] for 380 nm and Morel et al. [2007b] for 412 and 490 nm) are also included. Regression results depart mostly from the model at 380 nm (top figure), showing a distinct underestimation of the latter. Similarly, the figure at 412 nm (middle) shows lower model values for K_d coefficients between 0.01 and 0.1 m^{-1}, whereas the bottom figure displays minimal differences between the two groups of points. Taking a closer look at the Table 2.3, the term which departs most drastically from models, is the exponent $e(\lambda)$. Updated values from 380 to 490 nm result in 50%, 70% and 88% of the original ones respectively.

The increasing difference towards shorter wavelengths suggests an enhanced content optical constituents that are highly absorptive in the blue part of the spectrum (CDOM and/or NAP). At this stage, in the absence of CDOM fluorescence data from the BGC-Argo collection, it can be only hypothesized about the contribution of CDOM. The present work however used a subset of the global data set with a similar analysis published by Organelli et al. [2017], which had access to the additional variables, concluding that high $K_d(380)$ values were attributed to higher-than-average FDOM over the entire basin. Nevertheless, for a full (dis)closure, further investigation is necessary in order to obtain a quantitative differentiation between the two possible components impacting absorption at shorter wavelengths.

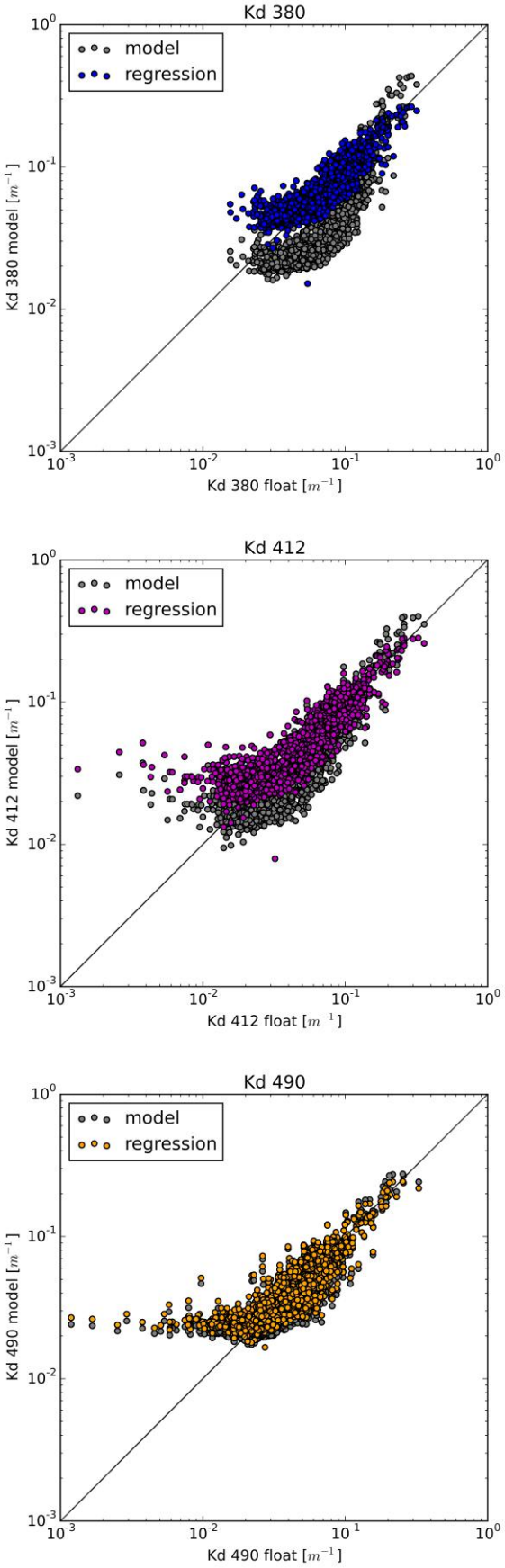

Figure 2.7. Scatter plot with K_d values from the regression analysis for the first optical depth z_{od} and float values. Grey dots show values obtained by bio-optical models [Morel and Maritorena, 2001; Morel et al., 2007b], whereas the coloured (blue, magenta and yellow) ones result from analyses shown in Table 2.3.

K_d - extending the model beyond the first optical depth

Even though the original model has been proposed only for the first optical depth in order to retrieve algorithms which could be in use for satellite remote sensing purposes, a similar regression analysis was carried out at different depths, from 30 to 90 m in a 15 m interval and from 90 to 150 in a 30 m interval. Note that the number of points considered depends also on the "euphotic range" criterion applied - for depths z where $PAR(z)$ was less than 1% of the surface value $PAR(0)$, points were omitted and thus also the calculation of K_d was dismissed.

Table 2.4. K_d exponential regression analyses for various depths.

Case / zmax	N	λ								
_	_	380			412			490		
_	_	R^2	χ	e	R^2	χ	e	R^2	χ	e
Morel 2001	_	_	0.127	0.685	_	0.1229	0.6533	_	0.0724	0.6896
Morel 2007	_	_	_	_	_	0.1333	0.6199	_	0.0825	0.6529
30	2591	0.77	0.1426	0.3105	0.84	0.1334	0.4136	0.84	0.0833	0.5401
45	3834	0.70	0.1424	0.2869	0.80	0.1319	0.3862	0.81	0.0822	0.5175
60	4898	0.60	0.1439	0.2807	0.76	0.1316	0.3762	0.79	0.0807	0.5122
75	5594	0.58	0.1429	0.2792	0.75	0.1308	0.3755	0.78	0.0797	0.5145
90	5940	0.47	0.1426	0.2786	0.74	0.1300	0.3766	0.78	0.0793	0.5181
120	6109	0.40	0.1418	0.2776	0.68	0.1296	0.3775	0.77	0.0792	0.5210
150	6145	0.40	0.1423	0.2801	0.60	0.1293	0.3746	0.77	0.0792	0.5214

With increasing depth, the correlation coefficient drastically decreases most visibly at 380 nm (from 0.77 to 0.4) and proves to be more stable at 490 nm (from 0.84 to 0.77). Standard deviations of regression coefficients, χ and e, are not shown in the Table 2.4, however, as in the regression analysis for z_{od}, coefficients of variance were calculated for both variables, displaying highest values at 380 nm (CV for χ and e from 1.3% to 1.7% and 2.1% to 3.2% respectively), diminishing towards 490 nm (CV for χ and e from 0.9% to 1.2% and 1.2% to 1.6% respectively).

Looking at Figures 2.8 and 2.9, plots display mean profiles of Chl with the standard deviation for the North Western Mediterranean (NWM) and Southern Levantine (SLEV) subbasins, both during summer months. In both figures, a distinct DCM feature can be observed, which is around 60 m for NWM with a mean Chl concentration of 0.3 $mg\,m^{-3}$ and 120 m for SLEV with Chl of 0.2 $mg\,m^{-3}$. Although the magnitudes appear similar, the standard deviation for the NWM is much higher compared to SLEV (0.3 and 0.05 $mg\,m^{-3}$ respectively). Other curves show K_d values obtained by BGC-Argo float data (dark blue), modelled K_d with coefficients from Morel and Maritorena [2001] (magenta) and Morel et al. [2007b] (cyan), as well as K_d obtained from

results of the regression analysis (red) for the maximum depth range (150 m) from Table 2.4.

K_d profiles are plotted only for the depth range above the 1% of the surface irradiance threshold, in both images clearly demonstrating the deepest penetration of light at 490 nm. The near-UV wavelengths (380 and 412 nm) attenuate at 45 and 60 m respectively in the NWM and at around 90 and 120 m in SLEV, whilst the light at 490 nm does not reach the critical value for the whole depth range of radiometric data available.

Confirming the spatio-temporal analysis of K_d for the first optical depth in Figure 2.6, K_d values decrease with increasing wavelength, although less noticeably during summer months, still, both Figures 2.8 and 2.9 show some variability when observing vertical profiles. Looking at BGC-Argo float profiles (blue), which are independent of Chl measurements, in NWM (Figure 2.8), $K_d(380)$ ranges between 0.07 m^{-1} at surface layers, increasing twofold at intermediate depths coinciding with the DCM depth. $K_d(412)$ values tend to be slightly lower, between 0.04 m^{-1} at surface layers, however increasing 3-fold at 60 m. Lower surface values in the near-UV/blue wavelengths are in agreement with previous findings by Xing et al. [2011]; Organelli et al. [2014]; Pérez et al. [2016] and Organelli et al. [2017], and could be explained by the photobleaching effect.

The study from Xing et al. [2014] underlined different CDOM dynamics at the surface compared to DCM depth. A subsurface CDOM maximum (YSM) was shown to be formed during summer (after phytoplankton degradation) and disappearing in winter, which was found at the same depth as DCM, both being indicators of CDOM originating from a decomposing phytoplankton biomass.

Lowest ranges are found for $K_d(490)$, following the shape of the Chl profile, thus having increasing values between 0.025 and 0.06 m^{-1}, decreasing to 0.035 m^{-1} at 150 m.

Moreover, the discrepancy between original models and regression-revisited values or data also decreases with increasing wavelength, thus corroborating Figure 2.7 and results from Table 2.4, proving that the Mediterranean Sea is biogeochemically much more complex compared to the simplified Case I definition and that Chl cannot be used as the main proxy to describe other optically active constituents, especially at 380 and 412 nm.

Lowest values are seen in the 490 nm, which corresponds with one of the reasons of that particular wavelength choice for remote sensing applications, however inherently carrying several caveats. In open ocean environments, where all biogenic constituents co-vary with Chl (Case I waters), $K_d(490)$ is assumed to be a good proxy for water turbidity (or better: clarity). Since

light energy is inversely proportional to wavelength, red photons have lower energy compared to blue ones and are thus attenuated at shallower depths. On the other hand, the blue part of the spectrum proves to be challenging from the atmospheric correction point of view due to an enhanced scattering of the atmosphere. 490 nm therefore proved to be a good compromise in order to reach deeper layers of the water with a lowest possible uncertainty in the atmospheric correction procedure.

Secondly, as it was already written in Chapter 1, the aim of apparent optical properties (AOPs, in this case K_d) retrieval is to limit the influence of a changing external (light) environment as much as possible and to relate them to IOPs. From this perspective, the choice of $K_d(490)$ could be to some extent debatable. As done in the analysed models, linking $K_d(490)$ directly to Chl could be questionable from a spectral standpoint: the blue (Soret) peak in phytoplankton (or more accurately, Chl) absorption is found at around 440 nm [Bidigare et al., 1990] and although 490 nm is a good compromise for the removal of a possible absorption signal from CDOM and/or NAP, the Chl absorption curve significantly decreases in a 50 nm range (e.g. see Bidigare et al. [1990] or Bricaud et al. [2004]), which could lead to a lower estimation of phytoplankton absorption. Still, as regression results show, the CDOM absorption signal could account for almost a large portion of the blue part of the spectrum (estimated to up to 50% of the total absorption at 443 nm from remote sensing [Swan et al., 2009]), thus, apart from having a historically rich data collection, 490 is chosen mostly for optimization reasons.

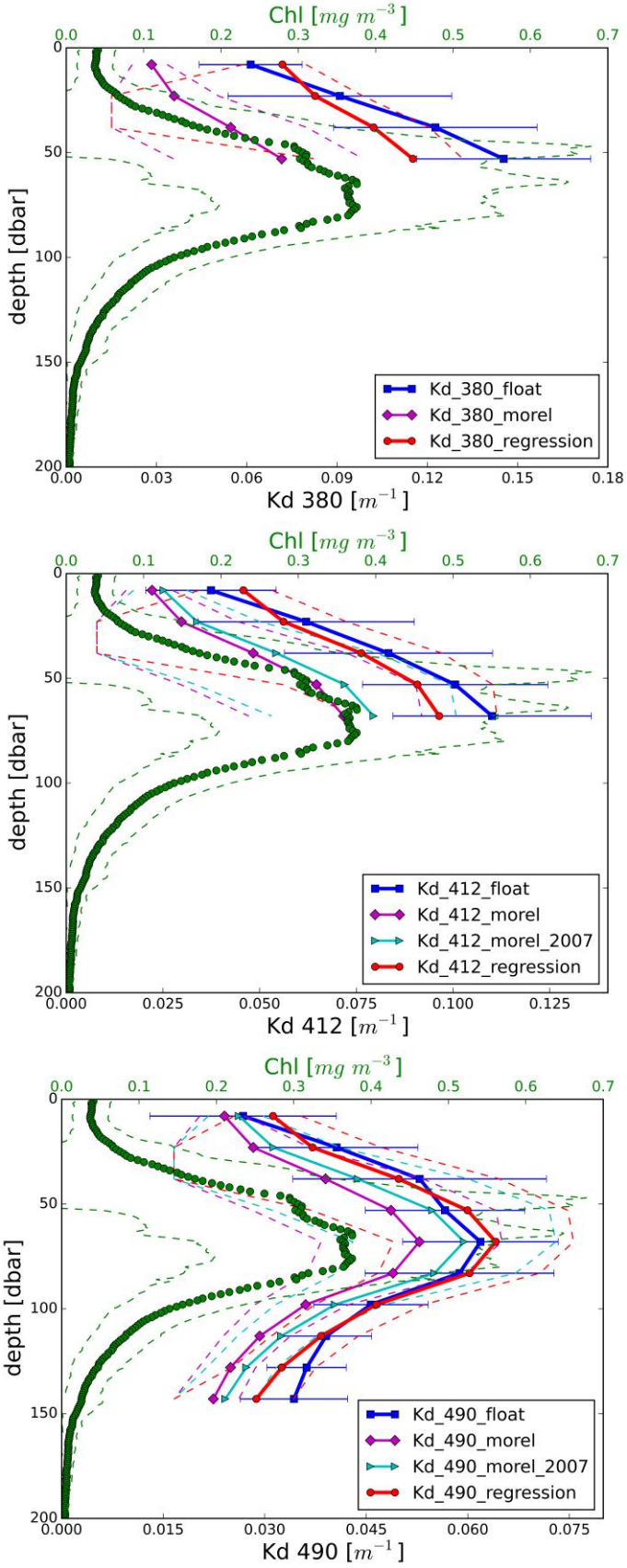

Figure 2.8. North Western Mediterranean subbasin (Summer) - Mean profiles of Chl with standard deviation (green dots and dashed lines), K_d values from floats and models. The blue line represents K_d derived from floats, the magenta and cyan lines depict Morel's models, whereas the red line shows the K_d curve with χ and e factors from the updated regression analysis for the maximum depth range (150 m) - Table 2.4.

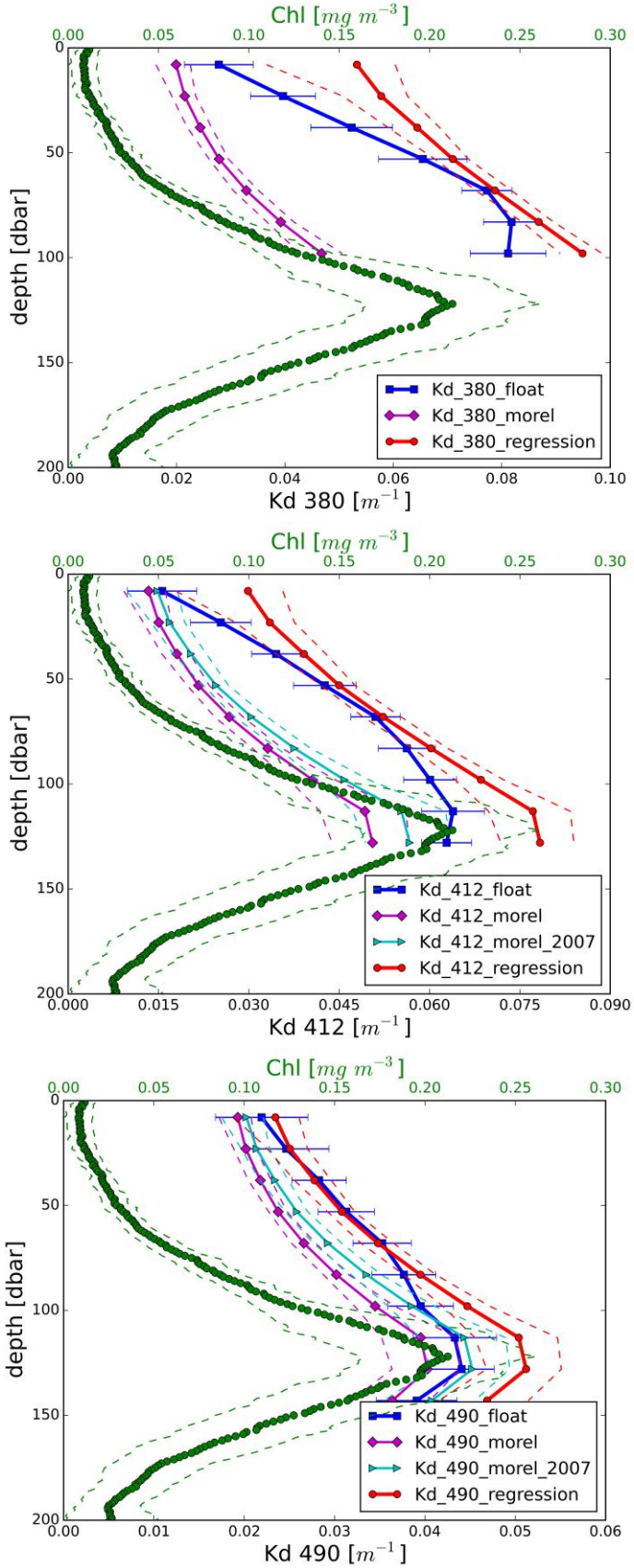

Figure 2.9. Southern Levantine subbasin (Summer) - Mean profiles of Chl with standard deviation (green dots and dashed lines), K_d values from floats and models. The blue line represents K_d derived from floats, the magenta and cyan line depict Morel's models, whereas the red line shows the K_d curve with χ and e factors from the updated regression analysis for the maximum depth range (150 m) - Table 2.4.

2.3.4 From $K_d(490)$ to $K_d(PAR)$

For modelling purposes, which will be further examined in Chapter 4, a regression analysis was carried out also between $K_d(490)$ and $K_d(PAR)$, following equation 2.9.

Some biogeochemical modelling approaches [Zaneveld et al., 1993; Lazzari et al., 2012], despite the weakness of such an approximation, use $K_d(490)$ as a surrogate for $K_d(PAR)$, although PAR is a measure of polychromatic radiation within the entire visible range, i.e., from 400 to 700 nm.

Although their relationship is not explicit, such an analysis is most likely due to the historical importance of $K_d(490)$ since the late 70s, thus a robust parametrization would allow to reconstruct a large data set available from decades of measurements. With this in mind, both equations from Morel et al. [2007b] were re-evaluated.

$$K_d(PAR) = a + bK_d(490) - c[K_d(490)]^{-1} \tag{2.9}$$

As explained in Morel et al. [2007b], $K_d(PAR)$ depends strongly on the layer thickness due to its polychromatic properties. Due to the fact that the red photons are absorbed more quickly at shallower depths, the spectral range of PAR actually narrows down deeper in the water column, thus concentrating around the least attenuated wavelengths. The relationship was therefore tested for two different depth ranges, $1/K_d(490)$ and $2/K_d(490)$ (added for cases of more turbid waters). Additionally, the z_{od} was added to the analysis, which was not considered in the original paper [Morel et al., 2007b]. Table 2.5 consists of regression analyses with three different depth ranges: from REG01 to REG03, calculations were carried out for $1/K_d(490)$, $2/K_d(490)$ and z_{od} respectively.

As shown in bar plots from Figure 2.6 and confirmed during the analysis, $K_d(PAR)$ is on average 1.5 times larger than $K_d(490)$, thus $1.5/K_d(PAR)$ will be approximately equal to $1/K_d(490)$ and similarly, $3/K_d(PAR)$ to $2/K_d(490)$-

Since z_{od} is equal to $4.6/K_d(PAR)$, as shown previously in section 2.2.1, the first optical depth matches slightly deeper layers, corresponding approximately to $3/K_d(490)$, which gives the polychromatic light a longer pathlength for attenuation.

All the cases in Table 2.5 show high correlations, ranging from 0.78 to 0.88, hence for remote sensing applications, $K_d(490)$ could be considered as a relatively robust AOP for $K_d(PAR)$ retrieval. The CV for coefficient c however proves to be highest for the REG03 case, resulting in 95% (compared to REG01 and REG02 which have a CV of 16% and 13% respectively). In all three cases the CV for a resulted in 9 to 10 % and 3 to 5% for b.

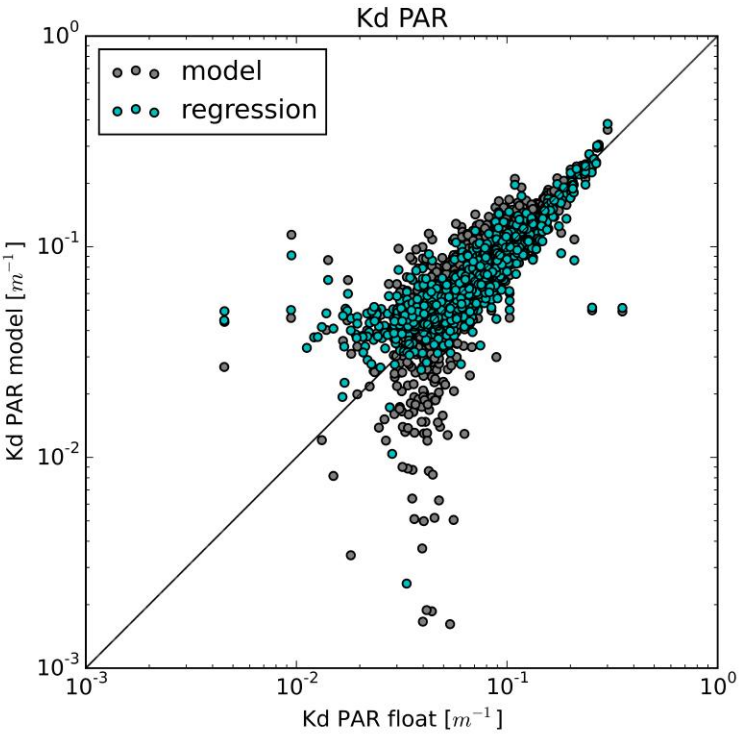

Figure 2.10. Scatter plot with $K_d(PAR)$ values from the regression analysis for the first optical depth z_{od} (REG03 in Table 2.5) and float values. Grey dots show values obtained with the bio-optical model [Morel et al., 2007b] for a maximum depth range of $1/K_d(490)$.

Table 2.5. $K_d(PAR)$ - $K_d(490)$ exponential regression analyses.

Case	max depth [m]	R^2	a	b	c
Morel 1	$1/K_d(490)$	_	0.0864	0.844	0.00137
Morel 2	$2/K_d(490)$	_	0.0665	0.874	0.00121
REG01	$1/K_d(490)$	0.78	0.0265	1.0868	0.00003
REG02	$2/K_d(490)$	0.84	0.0480	0.9407	0.00072
REG03	z_{od}	0.88	0.0379	0.7460	0.00032

2.4 Conclusions

An ample and spatio-temporally heterogeneous data set from the BGC-Argo network was analysed with the aim to get a grasp on the nature of bio-optical and biogeochemical properties in the Mediterranean Sea. Findings can be summarized as follows:

- The presence of DCM gradients was confirmed by having observed deeper DCM (from 80 to 130 m) with lower magnitudes (between 0.2 and 0.4 $mg\,m^{-3}$) in eastern basins and vice-versa for the west (mean depths from 60 to 80 m with Chl values from 0.4 to 0.8 $mg\,m^{-3}$). Features are ubiquitous during all seasons except winter in the Western Mediterranean, when strong convective processes erode the stratified water column and thus the DCM.

- Similarly, K_d values have proven to be systematically higher (from 30 to 50%) for western basins compared to eastern ones at all wavelengths, as well as for $K_d(PAR)$. For the first optical depth, highest values are reached during winter and spring months, drastically decreasing in summer. At shorter wavelengths (380 and 412 nm) such behaviour could be attributed to lower CDOM concentration, affected by photobleaching.

- The updated regression analysis, following bio-optical representations of K_d with Chl, as proposed in Morel and Maritorena [2001] and Morel et al. [2007b], showed high correlation (> 0.8) at all wavelengths for the first optical depth z_{od}, which deteriorated after having considered depths beyond z_{od}, least so at 490 nm (shown in Table 2.4).

- By looking at vertical profiles of mean Chl concentration with K_d values from models and data, divided seasonally per subbasin, 380 and 412 nm wavelengths attenuate to 1% of the surface irradiance value at depths which are almost 3 times shallower compared to 490 nm.

- Chl proves to be insufficient as a biogeochemical parameter to describe the nature of K_d functions as in classical Case 1 water types (see Table 2.4 or Figures 2.8 and 2.9). The enhanced absorption in the near-UV/blue suggests higher than average concentrations of CDOM (confirmed by previous publications) and possibly NAP (at present still no studies related to that).

- The relationship between $K_d(PAR)$ and $K_d(490)$ proved to be robust and should be further considered as a possible parametrization in the 3-dimensional biogeochemical model, which will be again discussed in Chapter 4.

- BGC-Argo floats prove to be an insightful platform both for data analysis and, as shall be seen in the next chapters, as a validation tool for different model configurations. Moreover, in Chapter 4, a match-up of $K_d(490)$ is shown with the satellite-acquired data.

- Despite a wide range of possible applications, it should be underlined that Chl is a fluorescence-derived property and thus prone to several sources of uncertainties. BGC-Argo floats are Lagrangian platforms and as such make (quasi-)synoptic controls with other techniques in order to control the Chl concentration magnitudes (e.g. HPLC or the absorption line-height technique from underwater spectral absorption and attenuation meter (AC-S) data) almost impossible to carry out.

2.5 Appendix A

Table 2.6. Floats tracking period and position (start-end)

Float	Start	End	Lon Start	Lat Start	Lon End	Lat End
lovbio001i	2012-11-26	2013-01-24	7.9129	43.3976	6.3333	42.5095
lovbio015c	2013-05-11	2015-03-18	5.5448	38.3756	6.8693	39.2280
lovbio016c	2013-05-28	2015-05-26	18.5325	37.7258	20.1217	36.7031
lovbio016d	2015-11-08	2016-01-04	8.5423	43.7651	8.1138	43.1795
lovbio017b	2013-04-11	2014-05-04	5.0089	41.9508	3.5216	41.4342
lovbio018c	2013-05-18	2015-05-23	28.0316	33.5997	31.4002	32.3531
lovbio035b	2013-02-21	2014-09-05	4.8633	42.2572	-2.1469	36.2265
lovbio039b	2013-07-25	2014-03-21	12.3115	38.9780	13.0921	38.4307
lovbio042c	2013-06-21	2013-07-07	11.9805	39.6628	11.9365	39.3841
lovbio053b	2013-05-29	2015-02-05	18.5210	37.7431	17.2169	40.0952
lovbio058c	2013-06-18	2015-05-20	11.9656	39.7163	11.2266	39.3356
lovbio063c	2015-03-03	2015-12-22	2.9287	40.9927	4.1317	39.4429
lovbio064b	2013-07-21	2014-03-13	7.8108	43.2953	7.7282	43.2507
lovbio064c	2014-03-17	2014-09-07	7.4037	43.1240	7.3871	42.9534
lovbio066c	2014-02-13	2014-05-22	20.5494	37.0316	22.2422	36.5036
lovbio066d	2014-08-04	2015-05-20	28.5970	34.6950	28.4608	33.5665
lovbio067c	2014-07-17	2016-01-05	5.9916	40.7025	4.4168	41.5186
lovbio068d	2014-07-11	2016-01-01	4.6018	41.9309	4.5600	41.0035
lovbio072c	2014-08-24	2015-09-10	6.5453	37.7768	3.0177	38.1262
lovbio083d	2015-07-01	2015-12-18	27.0414	34.6217	27.8136	33.9370
lovbio085d	2015-05-27	2016-01-03	27.1585	34.5837	27.8724	34.5843
lovbio088d	2015-05-20	2015-11-28	18.5157	38.3012	18.0528	37.5547
lovbio089d	2015-06-04	2015-12-12	10.6694	39.2940	10.1485	39.2201
lovbio090d	2015-05-23	2015-12-18	27.8026	35.6123	26.8293	35.0650
lovbio091d	2015-06-01	2016-01-01	20.0461	36.7235	19.5772	35.9591
lovbio093d	2015-05-27	2015-12-24	28.2032	33.4612	29.4236	33.1930
ogsbio001b	2014-05-28	2015-02-17	-0.6030	36.9278	1.3854	36.5892
ogsbio002b	2015-06-02	2016-01-02	10.7674	39.2503	8.4489	38.3500
ogsbio003b	2015-03-29	2015-12-28	18.3117	41.5346	18.1775	39.5091
ogsbio004b	2015-05-30	2016-01-02	20.0672	36.6967	19.0187	36.4012
ogsbio006b	2014-02-21	2015-03-20	17.7034	41.8324	17.4001	38.5404

Chapter 3

Integration of bio-optical data with numerical models

Abstract

The present chapter is a summarizing version of the publication currently under revision on Biogeosciences [Terzić et al., 2018]. The study is based on a data set comprised of 31 BGC-Argo floats that collected vertical profiles of biogeochemical and optical data from 2012 to 2016 in the Mediterranean Sea. The data set was integrated in 1-dimensional model simulations following trajectories of each float and considering measured photosynthetically available radiation (PAR) profiles as the reference light parametrization. Simulations were aimed to be consistent with data measured by float sensors, especially in terms of deep chlorophyll maximum (DCM) depth. Several light models were tested in order to estimate their impact on modeled biogeochemical properties, including self-shading dynamics based on chlorophyll and colored dissolved organic matter (CDOM) concentrations. Results, evaluated with the corresponding in-situ BGC-Argo chlorophyll data, indicate that the proposed approach allows to properly simulate chlorophyll dynamics and illustrate how PAR and vertical mixing are essential environmental regulation factors driving primary producers dynamics. Higher skills are reached using in-situ PAR, but some of the alternative bio-optical models presented show comparable skill in reproducing DCM depth spatial variability. The approach here presented serves as a computationally smooth solution to analyse BGC-Argo floats data and to corroborate hypotheses on their spatio-temporal variability.

3.1 Introduction

The methodology proposed in this work embeds radiometric quantities measured by BGC-Argo floats within a 1-dimensional (1D) numerical model in order to replicate the biogeochemical evolution of the water column observed by floats. For each float, a separate simulation is carried out and measured chlorophyll concentrations (i.e. derived from fluorescence) are compared with simulated values.

Given the substantial number of profiles and their high vertical resolution, such simulations can be considered as a convenient evaluation tool of chlorophyll spatio-temporal patterns along the water column by comparing them with corresponding in-situ measurements. Furthermore, the present method allows an implementation of various bio-optical models in order to estimate how well they perform compared to in-situ measurements of photosynthetically active radiation (PAR). The objective of such analyses is twofold:

1. to show how it is possible to integrate BGC-Argo float bio-optical data and a simple 1-D model in order to investigate chlorophyll vertical dynamics;

2. to use such a tool on a sufficiently large data set in order to test different bio-optical models.

3.2 Methods

3.2.1 BGC-Argo data set

The Mediterranean Sea BGC-Argo network operating in the period 2012-2016 was composed of 31 floats and has been already extensively described in Chapter 2. All 7 variables (T, S, Chl, $E_d(380)$, $E_d(412)$, $E_d(490)$, PAR) were for modelling purposes vertically interpolated to a resolution of 1 m in the upper 400 m. A further explanation is however required regarding PAR measurements: it should be underlined that the operational definition of PAR used by the BGC-Argo community takes into consideration the planar irradiance E_d rather than the scalar one E_o, therefore differing from its theoretical definition and leading to an underestimation of its values by 30% or more [Mobley et al., 2010]. Scalar values of PAR were thus derived according to Baird et al. [2016b], although neglecting the correction related to irradiance scattering due to a lack of information on IOPs. The second possible approach is based on a constant correction factor: in-situ experiments carried out in the Tyrrhenian Sea indicated that a correction factor of 1.58 can be applied to retrieve scalar from planar irradiance (Dr. Luca Massi, University of Florence, pers. comm.). Both approaches give consistent results with a slightly higher skill in the first case, which was adopted in the experiments shown in the following sections.

A simple geographic partition of profiles was performed with a spatial division into 13 (out of 16) subbasins shown in Figure 2.1 (see Table 2.1 for the number of profiles per subbasin) in Chapter 2.

3.2.2 1-D Biogeochemical model

Biogeochemical processes have been simulated according to the voxel approach ("volume element with biological content and processes", Kohlmeier and Ebenhöh [2009]), which represents a value on a regular grid in 3-dimensional space (i.e. a "3-dimensional pixel"). It is discretized along the vertical in order to resolve vertical irradiance attenuation and nutrient gradients. Each voxel replicated light and mixing conditions according to the trajectory and measurements of the corresponding BGC-Argo float, thus simulating a pseudo-lagrangian

experiment. No exchanges of mass between voxel and the surrounding field have been considered, which implies smaller mass exchanges due to horizontal diffusion and baroclininc components of the (upper ocean) advection field compared to vertical processes and biogeochemical dynamics. Conversely, voxel exchanges heat with the atmosphere and receives light in accordance with its moving position. Such an approach, similar to the one adopted by Kohlmeier and Ebenhöh [2009], has been already successfully applied by Mignot et al. [2018] in order to analyse BGC-Argo Floats in the North Atlantic. Furthermore, it was assumed that major biogeochemical transformations can be described by the Biogeochemical Flux Model (BFM) parametrizations (see below), properly driven by a bio-optical model, which has been validated by contrasting model results and experimental data, as shown later. The model is formulated through a system of partial differential equations:

$$\partial_t C_i(z,t) = \partial_z[D_v(z,t)\partial_z C_i(z,t)] + v_{sink,i}\partial_z C_i(z,t) + BFM_i(T,S,PAR,\overline{C}(z,t)) \tag{3.1}$$

where C_i is the i-th biogeochemical tracer simulated (i=1,50), D_v is vertical eddy diffusivity coefficient derived with the vertical mixing model described in the Vertical Mixing Models subsection, v_{sink} is the sinking velocity and BFM_i is the reaction term corresponding to the tracer C_i. T, S, PAR are the data measured by BGC-Argo floats. In the first set of simulations, the biogeochemical model was forced by PAR measurements obtained from BGC Argo floats. Experimental values of temperature and density (computed from float profiles) were also taken into consideration. A simulation for each of the BGC-Argo float trajectories was performed with this set-up, hereafter abbreviated as REF. Four additional sets of simulations were performed on the REF configuration by applying different values of vertical eddy diffusivity coefficients (MLD1, MLD2, MLD3 and MLD4) in order to assess uncertainties due to different vertical diffusion parametrization. Six additional sets of simulations were performed by forcing the biogeochemical model with PAR obtained by alternative bio-optical models (OPT1, OPT2a,b,c,d), one of which considered also the current modelling approach in the CMEMS Copernicus system (OPT3), described in Chapter 4. In this way, the possibility of using biogeochemical models in the absence of PAR measurements was assessed. Finally, a set of simulations was devoted to understand the impact of using a constant light approximation rather than following the diurnal light variation (CL1 and CL2 configurations) on chlorophyll distribution. Furthermore, the impact on light propagation due to coloured phytoplankton degradation products, i.e. CDOM (OPT4a,b,c,d and OPT5), was evaluated. On the whole, 17 classes of simulations were tested, which are summarized in Tables 3.1 and 3.2.

The biogeochemical model BFM [Vichi et al., 2013] is a biomass-based

numerical model that simulates the biogeochemical fluxes of carbon, phosphorus, nitrogen, silicon, and oxygen, characterizing the lower trophic level (producers, consumers, and recyclers) of the marine ecosystem. Its application is based on the coupled transport-biogeochemical model OGSTM-BFM [Lazzari et al., 2012, 2016]. It includes four phytoplankton functional types (diatoms, nanoflagellates, picophytoplankton, and dinoflagellates), carnivorous and omnivorous mesozooplankton, bacteria, heterotrophic nanoflagellates, and microzooplankton. Each variable is described in terms of internal carbon, phosphorus and nitrogen concentrations. Phytoplankton functional types can be characterized regarding prognostic Chl and can additionally consider the silicate component for diatoms. Particulate and dissolved organic matter are also included, the latter partitioned in labile, semi-labile and semi-refractory phases, according to bacterial capability of decomposing them to inorganic compounds. The present study is focused mainly on Chl, reserving to future analysis (according to data availability and optical model complexity) a study of Plankton Functional Types (PFT) resource competition dynamics [Ryabov and Blasius, 2011, 2014].

Initial conditions for all biogeochemical variables of BFM are provided by the CMEMS reanalysis of Mediterranean Sea biogeochemistry [period 1999-2015, Teruzzi et al., 2014] produced by the MedBFM model system. The initialization profiles are extracted from the MedBFM model output array, taking the nearest model point to the BGC-Argo position in time and space. Simulations' time scale corresponds to a typical BGC-Argo time-series length during the period 2012-2016, i.e. 11 months on average, with a vertical resolution of 1m. After being initialized, the model evolves without further assimilation of biogeochemical data from the 3D configuration.

Vertical eddy diffusivity coefficient profiles $D_v(z)$ are here represented as Gaussian-shaped functions, using potential density values for the mixed layer depth (MLD) calculation with a density-based criterion [de Boyer Montégut et al., 2004; D'Ortenzio and Prieur, 2012]. Such a shape is chosen due to its simplicity and in order to allow a gradual increase of vertical mixing through the pycnocline. Approaches and impacts of using different parametrizations to reconstruct mixing along the water column are shown and discussed in the Vertical Mixing Models subsection. Since the surfacing of BGC-Argo floats is programmed at around local noon, the variability related to diurnal variation of solar irradiance is taken into consideration according to Kirk [1994].

Vertical Mixing Models

Unlike radiometric data, vertical mixing is an indirectly obtained quantity, described in terms of potential density (from temperature and salinity data)

Table 3.1. Model configurations considered in the present work. All simulations include diurnal variability except the two cases with continuous light (CL1 and CL2), which use 24-hour averaged irradiance values.

SIM	MODEL DESCRIPTION
REF	$E_d(PAR)$ from BGC-Argo floats ; $D_v^{background} = 10^{-4} m^2/s$
CL1	as REF with continuous daily light
CL2	as REF with continuous daily light and $D_v^{background} = 10^{-6} m^2/s$
MLD1	as REF with $D_v^{background} = 5\,10^{-5} m^2/s$
MLD2	as REF with $D_v^{background} = 10^{-5} m^2/s$
MLD3	as REF with $D_v^{background} = 5\,10^{-6} m^2/s$
MLD4	as REF with $D_v^{background} = 10^{-6} m^2/s$
OPT1	Riley: $K_d(PAR) = 0.04 + 0.054\ Chl^{\frac{2}{3}} + 0.0088$ Chl
OPT2a OPT2b OPT2c OPT2d	$K_d(PAR) = \mathrm{a}\ Chl^{b} + \mathrm{c}$
OPT3	$K_d(PAR)$ for the first optical depth $z_{od} = z_{eu}/4.6$
OPT4a	as OPT2a + Chl degradation to CDOM - time scale 1 day
OPT4b	as OPT2a + Chl degradation to CDOM - time scale 1 week
OPT4c	as OPT2a + Chl degradation to CDOM - time scale 1 month
OPT5	as OPT2a + CDOM following Dutkiewicz et al. [2015]

Table 3.2. Parameters derived for optical models using BGC Argo float data. For each version of OPT2 only data shallower than z_{max} were used to compute the regression.

Model	z_{max}	R^2	a	b	c
OPT2a	150	0.53	0.075 ± 0.0015	0.572 ± 0.018	0.027 ± 0.001
OPT2b	75	0.61	0.064 ± 0.0015	0.615 ± 0.021	0.040 ± 0.002
OPT2c	45	0.71	0.077 ± 0.002	0.469 ± 0.021	0.034 ± 0.002
OPT2d	30	0.75	0.088 ± 0.003	0.406 ± 0.023	0.029 ± 0.003

along the water column. Vertical eddy diffusivity coefficients (D_v) are defined as Gaussian-shaped functions in the form of:

$$D_v = D_v^{MLD} e^{-0.5(\frac{z}{(\sigma * MLD)})^2} + D_v^{background} \tag{3.2}$$

σ was identified after an initial tuning procedure and equals 0.3 in all simulations. Values in REF model are equal to $D_v^{MLD} = 1.0 m^2 s^{-1}$ and $D_v^{background} = 10^{-4} m^2 s^{-1}$.

The mixed layer depth (MLD) was defined with the density criterion at the threshold value [de Boyer Montégut et al., 2004; D'Ortenzio and Prieur, 2012]:

$$\Delta\rho_\theta = |\rho_\theta(10m) - \rho_\theta(z)| = 0.03 kg/m^3 \tag{3.3}$$

In simulations MLD1, MLD2, MLD3, and MLD4, $D_v^{background}$ values were perturbed for two orders of magnitude (from 10^{-6} to 10^{-4} $m^2 s^{-1}$) in order to estimate the impact such variations have on modeled Chl profile shapes compared to measured ones (see Table 3.1).

Bio-Optical Models

Alternative solutions to measured PAR profiles were used in models OPT1, OPT2abcd, OPT3, OPT4abc and OPT5. They differ in methods used to evaluate the diffuse attenuation coefficient for PAR, $K_d(PAR)$, which is parametrized as a function of Chl concentration rather than being directly calculated from BCG-Argo irradiance data (see Tables 3.1 and 3.2). OPT1 uses the relationship obtained by a statistical analysis done by Riley [1956, 1975]:

$$K_d(PAR) = 0.04 + 0.0088\,[Chl] + 0.054\,[Chl]^{\frac{2}{3}} \tag{3.4}$$

In OPT2 models, statistical regressions were carried out between $K_d(PAR)$ and Chl measured by BGC-Argo floats at four different depth ranges: 150 m, 75 m, 45 m and 30 m (OPT2a to OPT2d, see Table 3.2 for details):

$$K_d(PAR) = a\,[Chl]^b + c \tag{3.5}$$

a and c represent regression coefficients and b the exponent (values reported in Table 3.2. Confidence intervals were calculated with Student's two-sided t-test, where the significance level α was set equal to 0.05). Diffuse attenuation coefficients $K_d(PAR)$ were calculated for PAR measured by BGC-Argo floats as the local slope of the natural logarithm of downwelling irradiance for layers of 15 m thickness for the euphotic depth range, which corresponds to an attenuation of downward planar irradiance to 1% of the subsurface value [Kirk, 1994].

Albeit the regression based on the upper 30 m depth range measurements showed highest correlation, all four bio-optical models were considered and adopted in simulations OPT2a,b,c,d (Table 3.2).

In model OPT3, based on the BGC-Argo data set, $K_d(PAR)$ is calculated for the first optical depth [Morel, 1988], the layer of interest for satellite remote sensing [Gordon and McCluney, 1975], and then adopted as a constant parameter for the entire water column. Such kind of light extinction definition has been used also in the 3-dimensional version of the OGSTM-BFM model, which integrates $K_d(490)$ data from satellite sensors as the external optical forcing in the exponential formulation of downwelling irradiance (for more details see Chapter 4) and Lazzari et al. [2012].

OPT4 and OPT5 models include CDOM dynamics as in the Mediterranean Sea the latter can absorb more than 50% of blue light [Organelli et al., 2014; Morel and Gentili, 2009], thus significantly impacting its attenuation along the water column. OPT4 assumes that CDOM is correlated to Chl production [Organelli et al., 2014] and that light attenuation is therefore affected by a progressive accumulation of such a constituent ("dead" chlorophyll, initialized at zero concentration). Accumulation is compensated by decay (first order kinetic) set at different e-folding characteristic times: 1 day (OPT4a), 1 week (OPT4b) and 1 month (OPT4c). OPT5 implemented a formulation of CDOM as described in Dutkiewicz et al. [2015]: a 2% fraction of all dissolved organic matter (DOM) fluxes is directed to CDOM, including both temperature-related decay and a photodegradation term based on PAR [Bissett et al., 1999]. Additional investigations are provided in section 3.3.3 to discuss CDOM dynamics along the water column. Given the mono-spectral nature of the current description of light, the attenuation of CDOM on PAR is computed by averaging the exponential law of CDOM absorption [Bricaud et al., 1981] on the visible range.

3.3 Results and Discussion

According to the work's objectives, four classes of simulations were considered, which correspond to the following subsections: the reference simulation, a subset with perturbed vertical mixing models, tests with different optical configurations, and a last group of additional analyses involving CDOM description. Outputs are validated qualitatively and quantitatively in terms of profile shapes and the deep chlorophyll maximum (DCM) depth. The DCM definition is already described in Chapter 2 and it is based on the absolute maximum of chlorophyll, excluding results of DCM shallower than 40 m or deeper than 200 m, as well as the ones with concentrations lower than 0.1 $mg\,m^{-3}$. All results, both for model and BGC-Argo floats, are averaged on a weekly basis.

3.3.1 Reference Simulation

The assimilation of PAR profiles into the 1-D model helped to accurately estimate the DCM depth. An overall model skill in the REF configuration is shown in Figure 3.1, with the histogram within indicating a normal distribution of residuals' deviation. Measured and modelled DCM depth showed high correlation (r=0.81, p-value<0.005). Both model and measurements indicate that DCM depth varies typically between 50-70 m in western areas (ALB, SWM1, SWM2, NWM, TYR) and is generally deeper in eastern areas (ADR2, ION3, LEV2, LEV3), between 100-140 m. Model tends to slightly underestimate the DCM variability (Figure 3.1, regression slope = 0.81 < 1), in fact, deepest simulated DCM are around 125 m depth, whilst floats data reach 140 m (e.g. lovbio18c data in Figure 3.1).

Chl patterns display high variability both at temporal and vertical scales, shown in Figures 3.2 and 3.3. The subsurface Chl pattern is formed by patchy structures and during stratification periods it is generally deeper moving eastward. BGC-Argo observations indicate that DCM is further eroded by vertical mixing occurring generally in autumn or early winter. Simulations provide an adequate reproduction of the Chl mixing timing and therefore the DCM erosion. By comparing point-to-point all Hovmöller maps (considering both depth and time variability) for measured and simulated Chl (examples are reported in Figures 3.2 and 3.3), an average correlation of 0.67 is obtained. Such a result quantitatively confirms that the alternation of mixing and stratification phases, as seen from BGC-Argo Chl measurements, is well reproduced. At surface, the increase in Chl is triggered by rather shallow mixing (0-75 m layer).

In addition to a correctly reproduced timing in the alternation of mixing

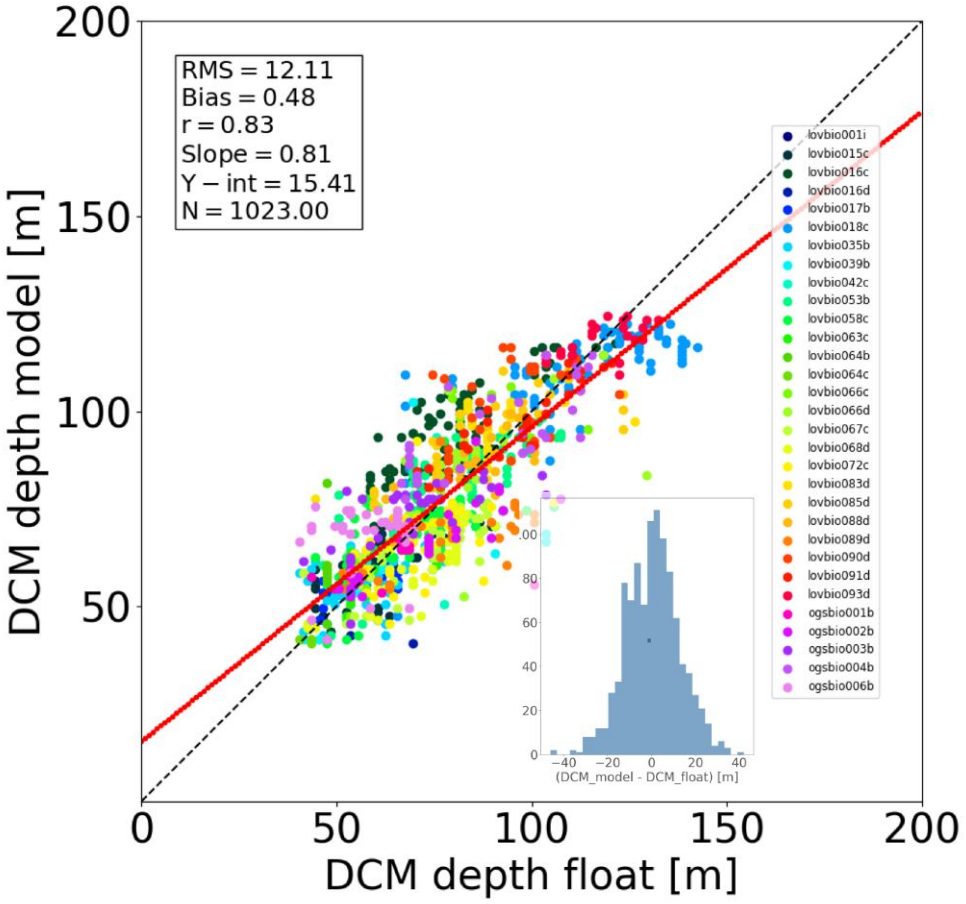

Figure 3.1. Match-up diagram comparing DCM depth obtained from BGC-Argo floats data versus REF model results. Each dot corresponds to a weekly profile. The red line depicts the linear regression between data and model values, defined by its slope and intercept (Y-int) shown in the box. Units of RMSD, Bias and Y-int are in meters. The correlation coefficient r is significant, with p-value $<$ 0.005. The bottom sub-figure shows the residuals' histogram. Floats' names, along with their tracking positions and periods, are reported in Appendix A within Chapter 2.

and stratification phases, proved by high correlation, simulated Chl reproduces also episodic signals, such as Chl deepening due to specific mixing events. For example, a mixing event in the NWM subbasin, reaching approximately 200 m depth during winter in 2015, triggers an intrusion of Chl (0.2 $mg\,m^{-3}$) in deeper layers consistently to BGC-Argo float measurements (float lovbio067c, Figure 3.2). Similar dynamics is reproduced in winter 2014 (Figure 3.3) for the lovbio035b float drifting from NWM toward the ALB subbasin.

Considering float trajectories, two kinds of situations are possible: the BGC-Argo float trajectory is relatively stationary in the deployment area (as shown in Figure 3.2), or the float passively migrates extensively, following a given water mass (as in Figure 3.3). It appears that also in the second case, when lateral dynamics effects could play an important role in BGC-Argo float measurements, the approach applied allows an adequate representation of measured Chl patterns. However, it should be noted that in the present multi-float simulation there are no trajectories including both west and east Mediterranean basins. In such cases, strong gradients between deep water nutrient inventories could invalidate the approach, and hence nudging or more sophisticated techniques would be required [Kohlmeier and Ebenhöh, 2009]. Lateral advection processes could indeed play an important role, although it appears that in the present case considering data-driven mixing and turbulence effects allows to simulate correctly the seasonal variability. The REF simulation can be therefore used as a reference for the following tests on mixing and bio-optical models analysed in the next sections. Furthermore, REF simulation results demonstrate that irradiance along the water column, besides mixing, is the driving mechanism controlling DCM depth. Figure 3.4 (top image) shows significant correlation between DCM and euphotic depths (i.e. where irradiance reaches 1% of surface PAR) , both in cases of measured and simulated Chl.

Similar results, valid on annual average conditions, were found by Mignot et al. [2014] in Eq. 9, where euphotic depth results to be 0.73% rather than 1% of surface PAR, interpreting that the DCM is located at a fixed PAR value, oscillating near the 0.5 $molquanta\,m^{-2}\,day^{-1}$ isolume. Comparable conclusions can be derived for analyses presented hereby, such as in Figure 3.4 (bottom image), where similar results hold true both for data and model outputs with a higher variability of critical PAR values in the case of shallower DCM.

The Mediterranean Sea a nutrient-limited basin (e.g. Crispi et al. [2001]; Lazzari et al. [2016]; Powley et al. [2017]), therefore an insight on the role played by nutrients requires further investigation. Phosphate dynamics shows an increase in surface Chl is driven by nutrient uptake in upper layers due to convective mixing. During stratification periods, the phosphocline follows the euphotic layer threshold. From results shown hereby, it can be ascertained

that together with a strong correlation between light and DCM depth, nutrient concentration is an important driver in regulating phytoplankton biomass at DCM, as depicted in Figure 3.5, where western subbasins exhibit significantly higher values, both of phosphate and biomass, compared to the eastern ones.

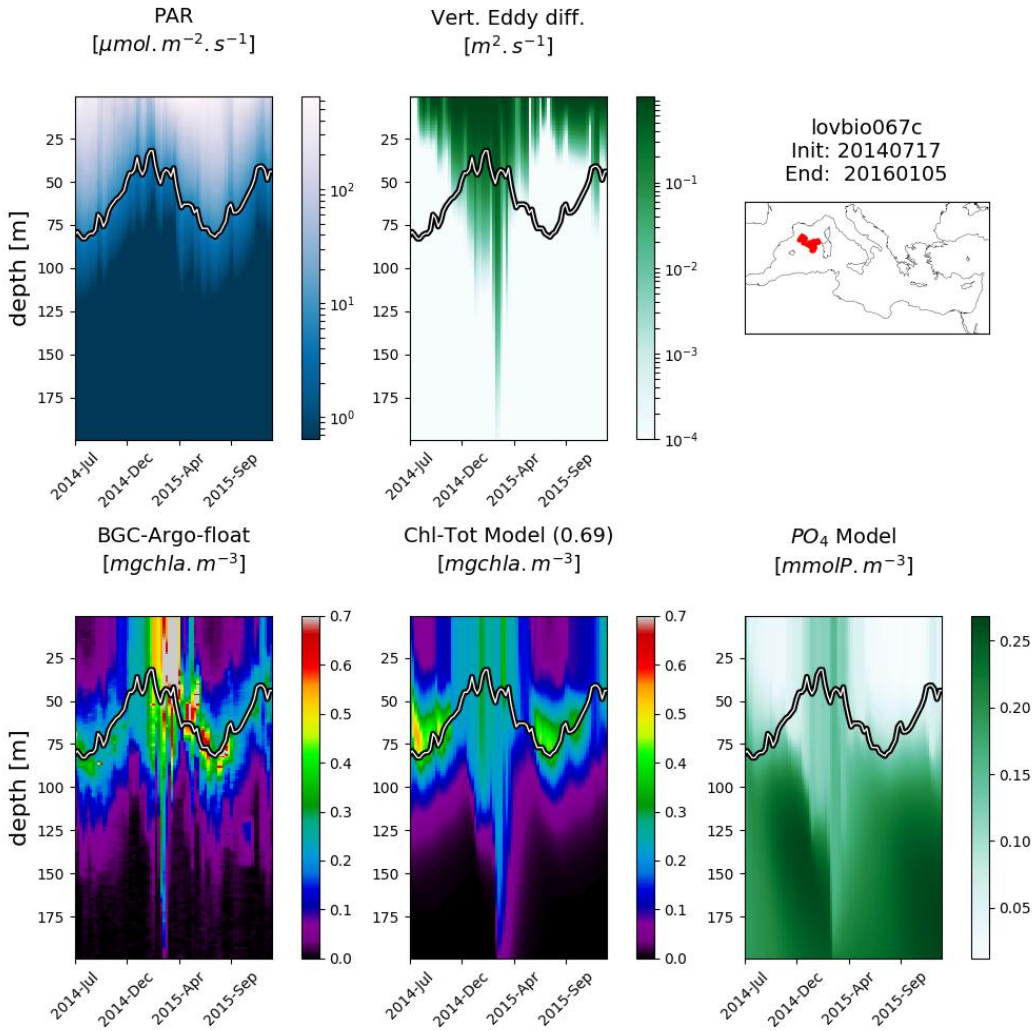

Figure 3.2. Hovmöller diagrams of BGC-Argo float lovbio067c (WMO code 6901649) comparing measured results and simulated ones (REF). The 6-imaged composite is organized as follows: top row shows PAR, vertical eddy diffusivity and the float trajectory; bottom row shows Chl derived from fluorescence measurements, simulated Chl and phosphate. The thick black-white line indicates the depth where PAR equals 0.5 $molquanta\, m^{-2}\, day^{-1}$ [Mignot et al., 2014]. The number in parentheses in modelled Chl indicates point-by-point correlation with BGC-Argo float Chl.

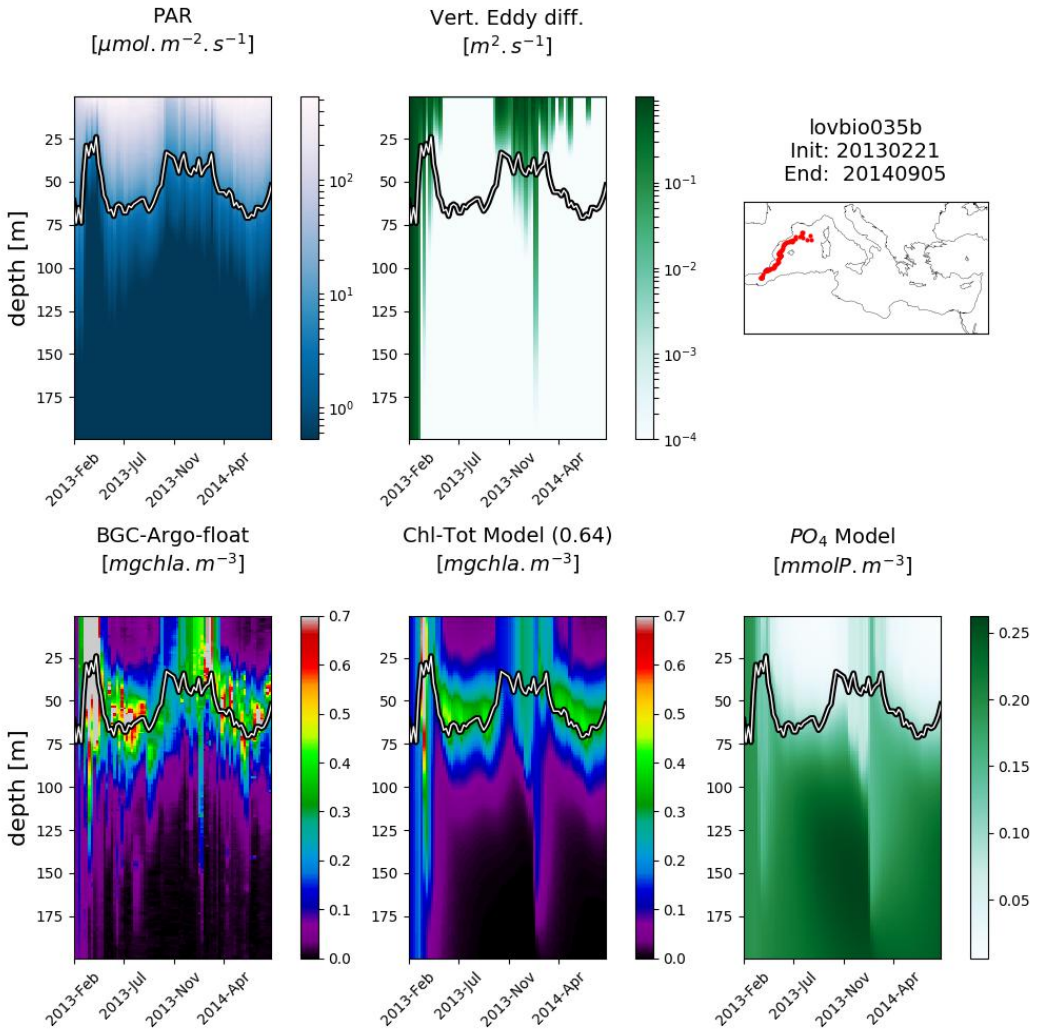

Figure 3.3. Hovmöller diagrams of BGC-Argo float lovbio035b (WMO code 6901511) comparing measured results and simulated ones (REF). The 6-imaged composite is organized as follows: top row shows PAR, vertical eddy diffusivity and the float trajectory; bottom row shows Chl derived from fluorescence measurements, simulated Chl and phosphate. The thick black-white line indicates the depth where PAR equals 0.5 $molquanta\,m^{-2}\,day^{-1}$ [Mignot et al., 2014]. The number in parentheses in modelled Chl indicates point-by-point correlation with BGC-Argo float Chl.

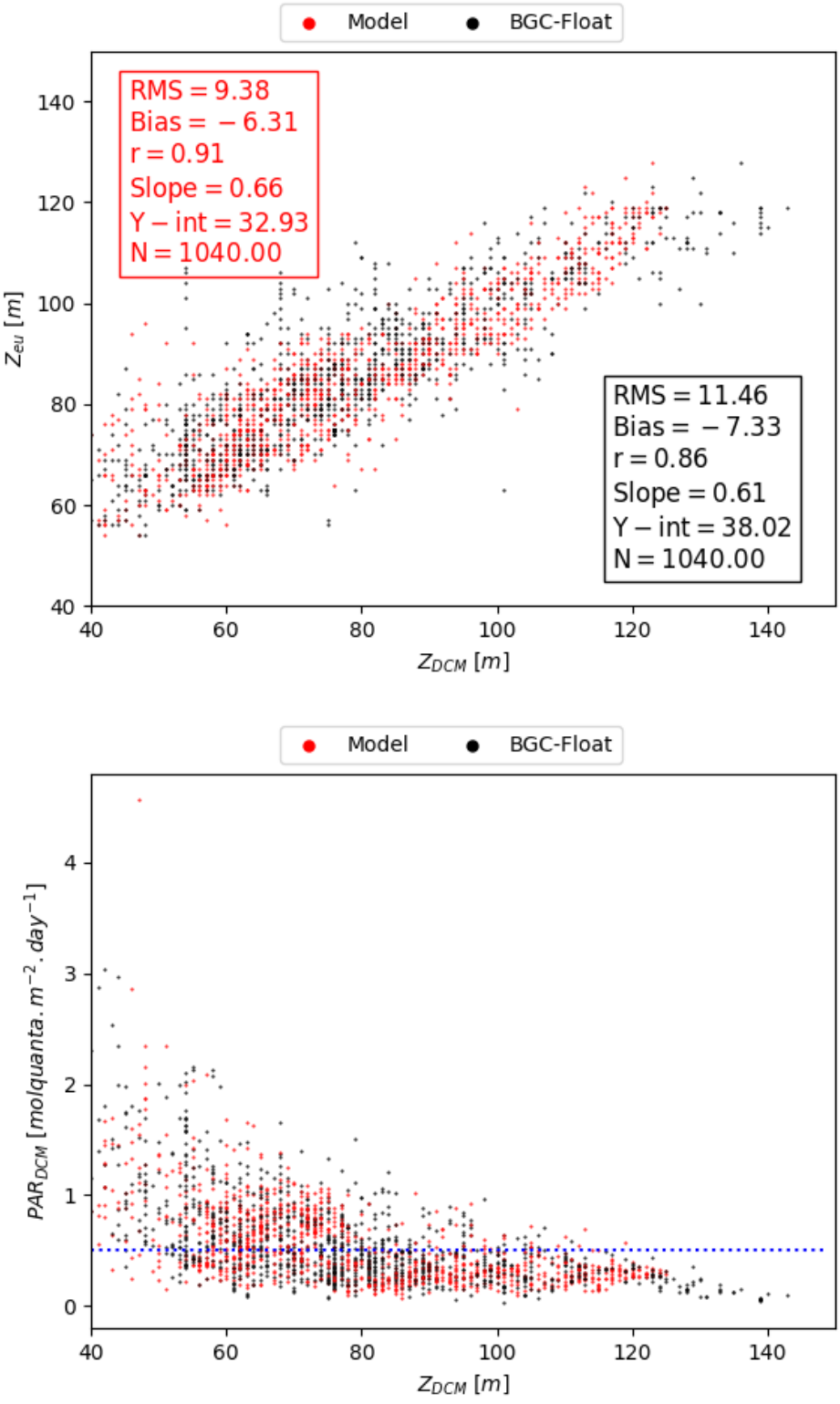

Figure 3.4. Top figure: DCM depth (z_{DCM}, x-axis) compared to the euphotic depth (z_{eu}, y-axis) both for modelled (red dot) and measured results (black dot). Red box (top left) reports statics for model z_{DCM} versus z_{eu}, whereas the black box (bottom right) shows statistics for z_{DCM} derived from chlorophyll data versus z_{eu}. Bottom figure: PAR values (y-axis) at DCM depth (x-axis) both for modelled (red dot) and measured results (black dot). Horizontal blue line marks the 0.5 PAR threshold (units $molquanta\, m^{-2}\, day^{-1}$) as identified in Mignot et al. [2014].

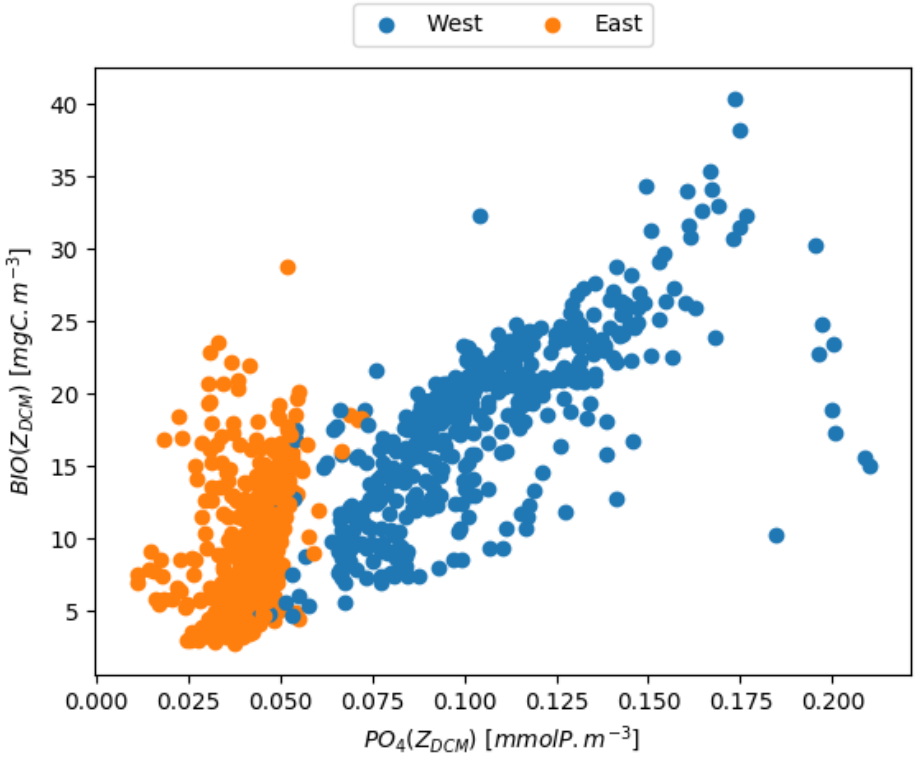

Figure 3.5. Phosphate (x-axis) and total biomass concentration (y-axis) of phytoplankton at DCM depth, including all modeled float trajectories.

3.3.2 Vertical Mixing Models

Several simulations, labelled as MLD1, MLD2, MLD3 and MLD4, were carried out by changing the background vertical eddy diffusivity coefficient $D_v^{background}$ values by two orders of magnitude (from $10^{-6}\,m^2\,s^{-1}$ to $10^{-4}\,m^2\,s^{-1}$, see Table 3.1). This subset of simulations (with float-derived PAR) clusters at a correlation of approximately 0.8 with a root mean square difference (RMSD) of DCM depth between 10-15 m (Figure 3.6).

3.3.3 Bio-Optical Models

The adoption of alternative bio-optical models (OPT1, OPT2, OPT3) results in correlation reduction from 0.8 (of the REF simulation) to 0.6-0.5 (Figure 3.6). OPT3, with almost zero bias, displays an intermediate skill compared to assimilated PAR simulations. OPT1 and the OPT2 cluster of simulations show slightly lower correlations with a RMSD of approximately 20 m in all cases, although increasing in bias (almost zero for OPT1 and from 6 m (OPT2a) to -14 m (OPT2d)). The latter may stem from the fact that DCM depth statistics performed for OPT2a to OPT2d models ranged from 150 m to 30

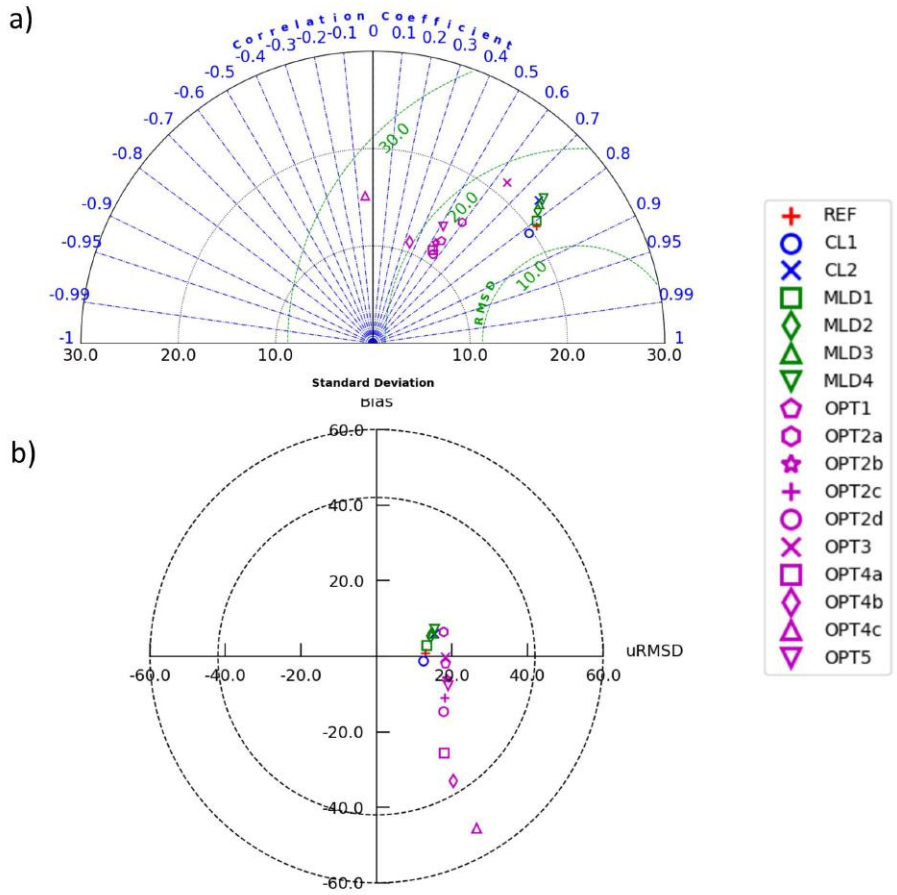

Figure 3.6. Panel a): Taylor diagram showing model skill in reproducing DCM depth compared to data. Correlation is represented by the angle with positive x axis, whereas distances from the origin depict standard deviations. Green circles illustrate iso-contours of RMSD levels. Panel b): Target diagram showing model skill in reproducing DCM depth compared to data. Distance to the origin defines the RMSD, all units are in meters. The position on x-axis is positive if the model standard deviation higher than the one from data results and negative in the opposite situation. For the sake of completeness, all models considered are reported in these summarizing skill diagrams.

m respectively, therefore lowering the number of points considered due to a reduced depth interval. Despite an increasing correlation of the bio-optical model linear regression with decreasing depth range, it should be underlined that the equations for lower depth ranges (such as OPT2d for the first 30 m) most likely do not perform well at greater depths, hence a higher bias in spite of a higher correlation coefficient.

3.3.4 Bio optical models with CDOM formulation

OPT4 and OPT5 simulations take into consideration CDOM dynamics by including an additional term to OPT2a, where light attenuation for PAR was described only in terms of Chl. In OPT4a, b, and c, CDOM is parametrized as "dead" chlorophyll, by changing only the rate of Chl decay from 1 day to 1 month. Such simplified dynamics description, albeit arguably, derives from high correlation observed between Chl and CDOM in Morel and Maritorena [2001]. It should be noted, however, that no analysis which would corroborate findings from Morel and Maritorena [2001] was carried out within the data set examined hereby due to the a lack of information on CDOM fluorescence. In all three model configurations, the "dead" chlorophyll accumulation results in higher turbidity levels that in turn reduce light penetration depths. This is quantified by significantly negative DCM biases (over 40 m in OPT04c), which result in shallower DCM compared to BGC-Argo derived profiles since the attenuation of Chl is overestimated even when considering fastest degradation rates (Figure 3.6). The experiment OPT5 mimics CDOM dynamics described in Dutkiewicz et al. [2015], where a lower bias is observed compared to the (over)simplified OPT04 tests (where correlation coefficients range from 0.6 to less than 0.1 for OPT04a to OPT04c respectively). OPT5 still results in a negative bias of around 10 m compared to the values from -25 m to -40 m for OPT04a to OPT04c.

In open ocean systems, at least three different mechanisms concerning CDOM entrainment in the euphotic layer are considered: lateral flux of CDOM from terrestrial waters (allochthonous origin), production of CDOM within the euphotic layer (autochthonous origin) and bottom-up flux of CDOM from the subsurface layer not affected by bleaching [Nelson and Siegel, 2013].

Figure 3.7 shows an example for a BGC-Argo float deployed in the North West Mediterranean subbasin (NWM). The model, regardless of initial conditions, correctly drives CDOM absorption coefficients in deeper layers to low values, while an enhanced surface production reinforces mineralization and bleaching and thus realizes a continuum of CDOM reactivity and lability. Results of CDOM variability from the BOUSSOLE site show that CDOM

absorption ranges to a maximum value of 0.07 m^{-1} and indicate that there is a temporal delay between phytoplankton bloom and a maximum in CDOM absorption (Figure 3 in Organelli et al. [2014]), whereas deeper layers (below 100 m) have generally lower CDOM absorption. The data set shown in Organelli et al. [2014] evidences that cycles of CDOM accumulation are followed by depletion in the upper 10 m due to photodegradation in summer. In modelling results presented hereby, bleaching has a deeper effect over the entire CDOM "productive" layer (see red and blue lines, Figure 3.7), while subsurface CDOM maximum is not reproduced. Additional investigations of the OPT5 model configuration can address the autochthonous source dynamics, as well as the bottom-up flux of CDOM in this region. Improving model dynamics calibrations could be possibly achieved by utilizing information on CDOM light absorption from BCG-Argo floats measurements [Xing et al., 2012b; Organelli et al., 2017].

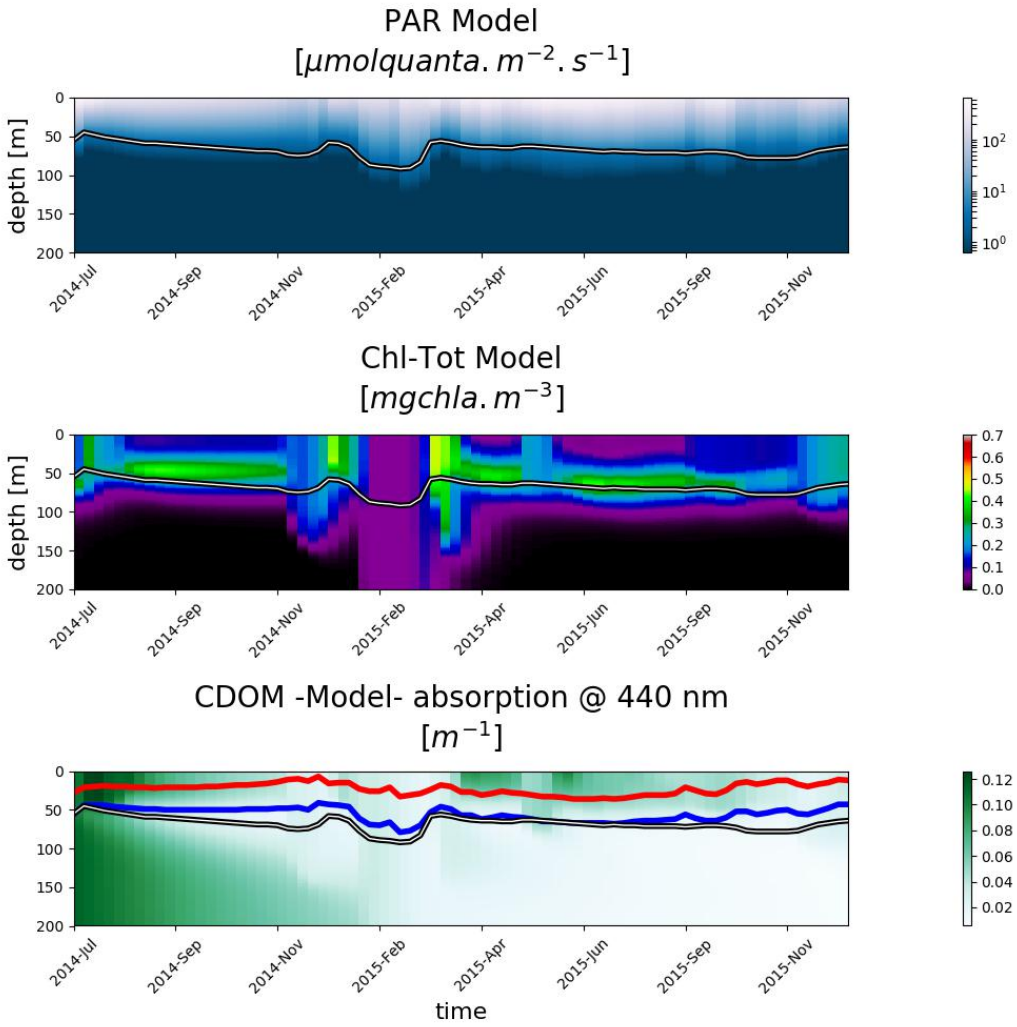

Figure 3.7. Hovmöller diagrams for BGC-Argo float lovbio068d (WMO code 6901648) showing: PAR (top), total Chl (middle) and CDOM (bottom) simulated by model configuration OPT5. The white, red and blue lines depict the euphotic, 100% and 10% bleaching depths respectively.

3.4 Conclusions

The coupled modelling/experimental approach presented here provides a robust and accurate reproduction of DCM variability across the Mediterranean Sea. Such a combined configuration can integrate in a single framework multi-data measurements provided by BGC-Argo floats. DCM is a ubiquitous feature of the Chl vertical structure in the Mediterranean, and different forcing conditions generate geographical gradients in DCM characteristics (i.e. shallower DCM in western regions, deepening eastwards). Second-order features, such as impulsive vertical spikes or specific patterns observed in BGC-Argo profiles, are also

qualitatively reproduced. Results can be summarized as follows:

- mixing and irradiance propagation control Chl dynamics;
- DCM position is mostly controlled by PAR;
- nutrients control the amount of biomass at DCM.

Moreover, it was demonstrated that vertical processes considered in the 1-D model, such as irradiance regimes and vertical mixing, allow to properly reconstruct a large part of Chl dynamics, which was quantified also by skill diagrams.

Such kind of data-rich experiments, combined with a 1-D numerical model, could be considered as a useful tool also to a broader community, rather than only to biogeochemical modellers, in particular to address process studies.

The presented approach might be useful also to quantify the amount of measured signal related to vertical dynamics and the one derived from other processes, such as horizontal advection and subduction of water masses. The usage of PAR measured from BGC-Argo floats (used in REF, CL1, CL2, MLD1, MLD2, MLD3 and MLD4) provides higher correlations compared to configurations with alternative bio-optical models (used in OPT1, OPT2, OPT3, OPT4 and OPT5), as shown in Figure 3.6a.

The comparison of different bio-optical models indicates that, when lacking direct measurements of PAR in subsurface layers, the most fitting alternatives would be OPT3, OPT2a and OPT1, that provide relatively lower bias and higher correlation coefficients (between 0.5 and 0.7), as well as lower RMSD values compared to REF.

Such an analysis can also suggest the rate of improvement when considering a value of light fully integrated in the visible range of the spectrum (400 to 700 nm, REF) versus simplified approaches (i.e. all the OPT simulations here considered).

Results further support the strategic relevance of BGC-Argo data. Temperature, salinity and radiometric parameters encapsulate fundamental information for the reconstruction of primary producers dynamics and are paramount to investigate hypotheses concerning DCM formation. CDOM fluorescence data measured by BGC-Argo floats could be integrated in simulations to further infer and reconstruct the observed biogeochemical processes.

Furthermore, considering a general 3-D biogeochemical model, it is not possible to have a full data coverage of the in-water PAR field without a fully coupled radiative transfer model. Such an approach could be thus exported to more complex 3-D biogeochemical models and generalized to regions other than the Mediterranean Sea (possibly on a global scale).

Chapter 4

The use of variable Kd coefficients in biogeochemical modelling

Abstract

Satellite data from the Copernicus Marine Data Stream were acquired in order to update the optical algorithm that has been used so far in the MedBFM biogeochemical model. The objective was to quantify the sensitivity of model results using climatological versus improved satellite data on diffuse attenuation coefficients for downward planar irradiance at 490 nm. The model output analysis was focused on chlorophyll *a* concentrations and validated also through the use of a quality-controlled Biogeochemical-Argo data set, which was compared to corresponding model outputs at given locations. Results indicate that by using the interannually variable data set, the divergence of updated K_d values compared to climatological ones extends to 20%, which results in variations in surface chlorophyll concentration magnitudes for up to 50 % compared to the use of a climatological data set. By looking at surface chlorophyll results, the seasonal variability decreases for approximately 5%, whereas the interannual variability varies among different subbasins for up to 20%. The deep chlorophyll maximum depth on average increases for 10 m with the use of the updated model, whilst DCM chlorophyll values result in minimal decreases in western subbasins (0.03 $mg\,m^{-3}$). A time series analysis of the site around BOUSSOLE shows a significant underestimation (more than 50%) of the model chlorophyll output compared to HPLC data, which is in-line with the previous reanalysis assessment. A match-up with float profiles of fluorescence-derived chlorophyll results in a slightly lower RMSE and higher correlation with the introduction of an interannually variable data set, thus displaying only a slight increase of the model product quality. A similar match-up was performed by comparing K_d functions from satellites and the ones derived from BGC-Argo radiometric data at 490 nm for the first optical depth, which resulted in systematically higher values from remote sensing observations compared to in-situ measurements.

4.1 Introduction

Despite their major shortcomings (i.e sensitivity to cloud coverage, the use of empirical or semi-analytical algorithms to retrieve information from the water-leaving signal, limitation to surface layers), satellites have been providing an ample global data set with a constant temporal acquisition frequency for almost 40 years and are as such essential also for model validation. A possible merging of different methods could surpass the limitations of separate techniques, thus a combination of numerical models and satellite data has been widely accepted

in the scientific community, most commonly denoted as data assimilation, the aim of which is to bring models into consistency with satellite observations. Such an approach might prove useful for parameter optimization [Ciavatta et al., 2011] and for providing state estimates (reanalyses), which was done also in the present chapter (see Teruzzi et al. [2014, 2018] for more details). Assimilating apparent optical properties (Ciavatta et al. [2014]; Jones et al. [2016]) or even phytoplankton functional groups [Ciavatta et al., 2018] could be a step further in bio-optical modeling, as the error in satellite data retrieval is generally lower for optical properties compared to biogeochemical variables like chlorophyll concentration.

As previously described in the Introduction section, methods of light implementation in ecological models range from simple exponential functions of photosynthetically available radiation (PAR) to fully coupled radiative transfer models. The former, simplest representation is still used in the present chapter, the objective of which is to evaluate the spatio-temporal variability and quantify the sensitivity between two light models in terms of chlorophyll concentrations. More specifically, the analysis is focused on the impact of changing diffuse attenuation coefficients of downwelling irradiance (K_d) from climatological (K_d^{clim}) to interannually variable (K_d^{var}) values, taking data from the Copernicus Marine Data Stream (based on ESA CCI merged files for K_d^{var} at 490 nm). The difference is quantified also in terms of deep chlorophyll maximum (DCM) depth and the product quality assessment (within the CMEMS framework) was done by comparing a match-up of chlorophyll and $K_d(490)$ profiles with a quality-controlled Biogeochemical Argo (BGC-Argo) data set, previously describer in Chapters 2 and 3.

4.2 Methods

4.2.1 Numerical model

The biogeochemical model BFM [Vichi et al., 2013] is a biomass-based numerical model that simulates biogeochemical fluxes of carbon, phosphorus, nitrogen, silicon, and oxygen, characterizing the lower trophic level (producers, consumers, and recyclers) of the marine ecosystem.

The light model used to evaluate photosynthetically available irradiance takes diffuse attenuation coefficients at 490 nm from satellites as the light extinction coefficient:

$$E_d(z) = E_d(z_0)e^{-K_d(x,y,z,t)z} \tag{4.1}$$

$$K_d(x, y, z, t) = K_{d490}(x, y, t) \tag{4.2}$$

where $E_d(z_0)$ is the broadband plane irradiance at the surface level, whereas x, y, and t are longitude, latitude and time, respectively.

Surface irradiance values are obtained from the ECMWF atmospheric model output, where the shortwave radiation Q_s (roughly between 0.2 and 4 μm) refers to radiation emitted by the Sun, then scattered, absorbed or transmitted by the atmosphere and reflected or absorbed by the surface [Hogan, 2017]. Following Ebenhoh et al. [1997], the visible portion of Q_s is then estimated with a multiplying factor of 0.5. In Lazzari et al. [2012], the light attenuation term is derived from SeaWiFS data of seasonal climatological measurements for the period between 1998 and 2004. As it has already been discussed in the aforementioned paper, such an approach could introduce uncertainties due to several reasons: firstly, the use of K_d for only one wavelength (490 nm) is chosen in order to parametrize the diffuse attenuation for the whole visible range (400-700 nm), namely $K_d(PAR)$, and as such does not exactly correspond to the quantity in question (see Chapter 2). Secondly, by extrapolating the constant value calculated for the first optical depth (on average between 15 and 35 m in the Mediterranean [d'Ortenzio and Ribera d'Alcalà, 2009]) along the entire water column, the depth variability is a-priori neglected, which is however present also in homogeneous water bodies (e.g. see Lee et al. [2005] and references therein).

Statistics are computed following the division of the Mediterranean Sea shown already in Chapter 2 (Figure 2.1 and Table 2.1).

4.2.2 K_d data set Reconstruction and Tuning

In the present chapter, a comparison was made between the use of climatological $K_d(490)$ maps (hereafter K_d^{clim}), used also in Lazzari et al. [2012], and an interannually variable data set (K_d^{var}), computed with the ESA-CCI technique for CMEMS at 1 km resolution, merging SeaWiFS, MODIS-Aqua, MERIS and VIIRS sensors (for more details see the Copernicus Quality Information document; Volpe et al. [2017]).

The K_d^{clim} tuning procedure in Lazzari et al. [2012] involved running hindcast simulations (i.e. without the satellite data assimilation) in order to compare the model output with corresponding in-situ values of DCM depth and magnitudes during summer in the Levantine basin (data from Turley et al. [2000] and Moutin and Raimbault [2002]), resulting in a multiplication factor of 1.2 of the original $K_d(490)$ values. Similarly, after a comparison with the tuned K_d^{clim} values for the same season and subbasin, K_d^{var} resulted in a

multiplication factor of 1.3. Such an approach could conceptually correspond more to $K_d(PAR)$ rather than $K_d(490)$, which will be further clarified in the model validation section.

The algorithm used to compute the diffuse attenuation coefficient of light at 490 nm for multi-sensors product is a fourth power polynomial expression of the remote sensing reflectance ($R_{rs}(\lambda)$) ratio ($R_{rs}(490)$ to $R_{rs}(555)$). The latter is shown in equation 4.3, whereas the $K_d(490)$ calculation is written in equations 4.4 and 4.5.

$$\rho_{490/555} = R_{rs}(490)/R_{rs}(555) \tag{4.3}$$

$$K_d(490) = K_w(490) + K_{bio}(490) \tag{4.4}$$

$$K_d(490) = 0.0166 + 10^{\sum_{n=0}^{4} a_n (log_{10}\, \rho_{490/555})^n} \tag{4.5}$$

Note that the regional algorithm for the Mediterranean Sea differs from the global, which has been thoroughly explained in Volpe et al. [2007], therefore also the algorithm for the climatological data set differs from the interannually variable one, which is also shown in Volpe et al. [2017] (see Table 4.1 below), where the SeaWiFS global algorithm is still used for the Black Sea.

Table 4.1. Coefficients used to retrieve the original data set of $K_d(490)$. For K_d^{clim}, the global algorithm for SeaWiFS is applied with a tuning factor (T.F.) of 1.2. For K_d^{var}, the regional MedOC4 is used instead [Volpe et al., 2007] with a tuning factor (T.F.) of 1.3.

Algorithm	**Model**	a_0	a_1	a_2	a_3	a_4	**T.F.**
SeaWiFS	K_d^{clim}	-0.8515	-1.8263	1.8714	-2.4414	-1.069	**1.2**
MedOC4	K_d^{var}	-0.7713	-2.2864	3.6408	2.3152	-5.172	**1.3**

By comparing products with different algorithms, an additional source of error is generated when trying to estimate the sole impact of introducing interannual variability in the reanalyses, thus a necessary step should be to compare the climatological year of K_d^{var} versus the interannually variable one.At this stage it is difficult to ascertain to what extent the difference could be additionally due to the use of diverse algorithms in order to obtain light extinction factor maps at 490 nm.

OGSTM-BFM model needs $K_d(490)$ maps that fully cover the Mediterranean basin surface. Daily data provided in the CMEMS catalogue at 1km of spatial resolution have been used to calculate weekly averages at the model resolution (1/16°). Resulting maps are affected by cloud coverage, thus it has

been necessary to reconstruct full maps by filling the gaps with monthly means and climatological values, the latter being introduced only after the monthly means in case of still incomplete coverage. Full-coverage maps were finally processed using an empirical orthogonal functions (EOFs) decomposition to spatially filter $K_d(490)$.

It should be noted that the analysis was constrained only to open ocean areas, i.e. deeper than 200 m [Lazzari et al., 2012, 2016], leaving the interpretation of coastal regions for future computations with a more sophisticated light model, which could link K_d functions to semi-analytical algorithms based on the radiative transfer equation in order to obtain information on IOPs [Lee et al., 2005].

4.2.3 K_d data set differences

Figure 4.1 shows climatological maps of the updated, K_d^{var} data set. Highest values (0.10 m^{-1} or higher) are displayed during winter and spring months, especially in the western basin. The peak is between February and March in the North-Western Mediterranean, which might coincide with the late winter/early spring bloom period. Constantly higher values are noticed also for the northern Aegean and Alboran seas, which however still prove to be the regions with major uncertainties in biogeochemical modelling due to insufficiently accurate boundary conditions (i.e. connecting the Mediterranean Sea with the Black Sea in the former and with the Atlantic Ocean in the latter case) and are thus less underlined in further elaborations. Lowest values (around 0.03 m^{-1}) are seen in the Ionian and Levantine subbasins almost throughout the entire year with increasing values between December and February (reaching 0.06 m^{-1}). A clear east-west gradient can be observed, with increasing values westward, which is in agreement with the BGC-Argo data analysis in Chapter 2.

In Figure 4.2, climatological months of differences (K_d^{var} - K_d^{clim}) normalized with K_d^{clim} values are shown, which can in turn demonstrate how the spatial variability of satellite-derived K_d is affected by the use of an interannually variable data set. Major discrepancies are seen for the western subbasins, where K_d^{var} values are more than 20% different compared to K_d^{clim}, suggesting more turbid water (higher K_d) in the period between October and February and a more transparent one (lower K_d) between March and May.

Eastern regions on the other hand depict a less conspicuous fluctuation of K_d values: winter and summer months exhibit a certain patchiness which might result in a minimum impact on subbasin scales.

Such patterns are expected to directly affect mostly the DCM depth (higher K_d resulting in shallower depths and vice-versa) and in cases of highest K_d values also surface patterns, especially in the North-Western Mediterranean.

Expectations are thus the following ones:

- DCM depth might increase throughout the entire basin especially in the period between September and January (although the feature will disappear in winter in western regions) and decrease from March to May. The summer period might result in negligible differences between two models due to low K_d anomaly values and a spatial patchiness or fluctuation of positive and negative anomalies (Figure 4.2).
- Regions with highest surface Chl values could coincide with subbasins with highest K_d^{var}, i.e. in the North-Western Mediterranean between January and April.
- The two reanalyses will display different model outputs, although it is expected that such a minor change in the description of light will have an almost negligible effect on Chl output and thus result in a slight product quality improvement, if any.

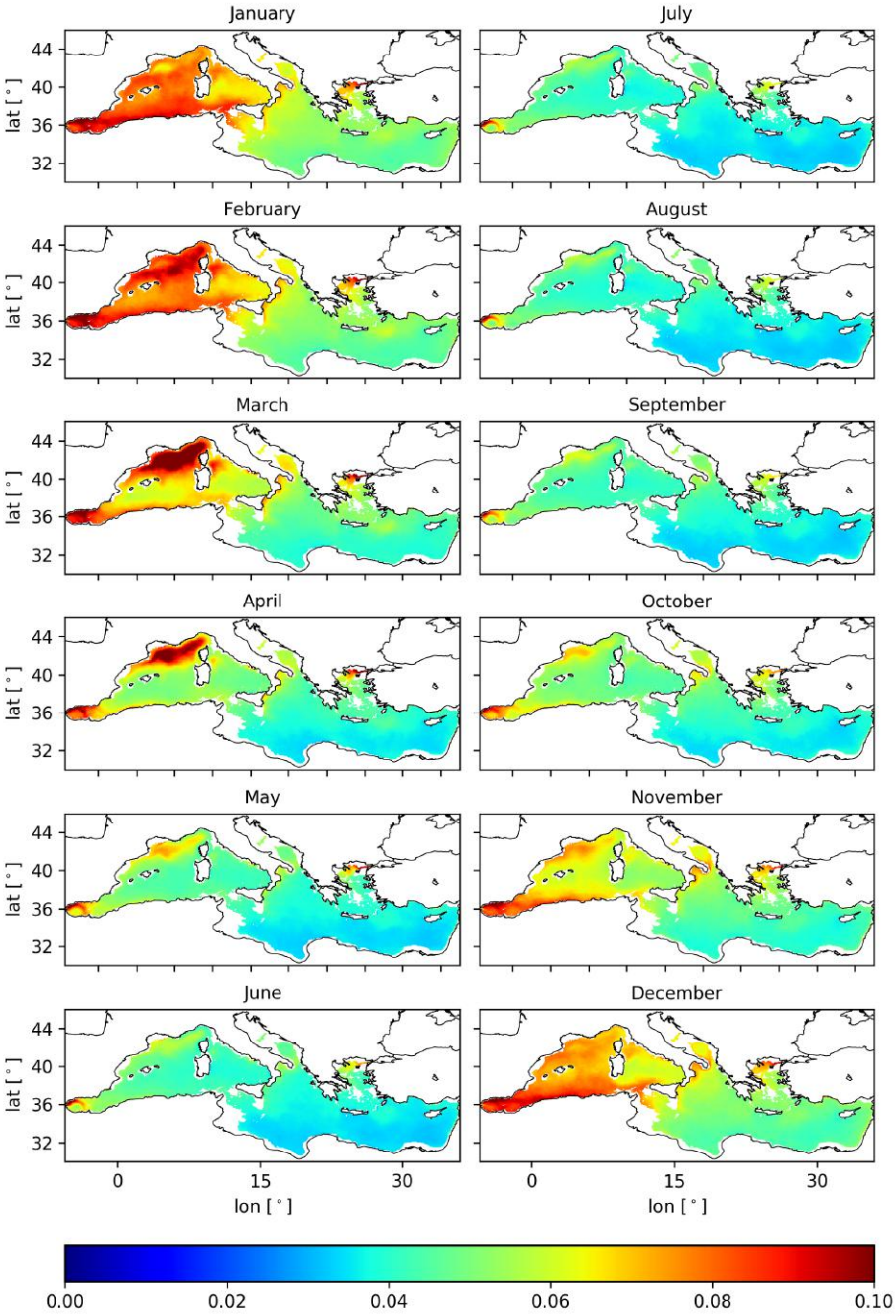

Figure 4.1. K_d^{var} - climatological map, units of m^{-1}.

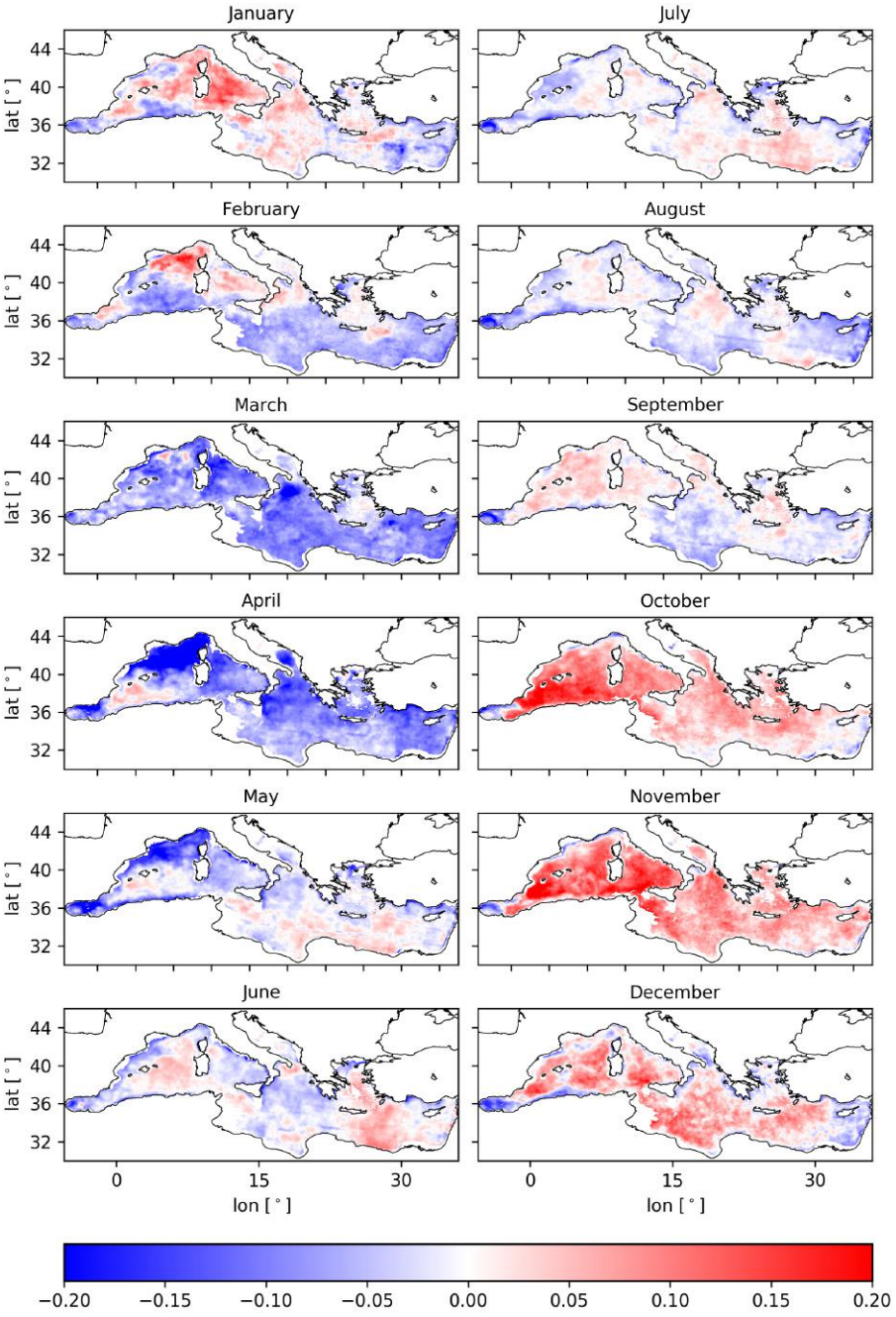

Figure 4.2. K_d - climatological map of anomalies (K_d^{var} - K_d^{clim}), normalized with K_d^{clim}, unitless.

4.3 Results

4.3.1 Impact of K_d^{var} on Chl

OGSTM-BFM was run for the period between 1999 and 2015, using two different $K_d(490)$ models, namely, K_d^{clim} and K_d^{var}, and assimilating Chl data from the ESA-CCI data set. The reference reanalysis (i.e. the one using K_d^{clim} as a light extinction factor), published in the CMEMS catalogue, has been already assessed in Teruzzi et al. [2018].

Model outputs for both simulations are evaluated in terms of Chl concentrations (units of $mg\,chl\,m^{-3}$). Anomalies are calculated as the differences between K_d^{var} and K_d^{clim} simulations, normalized with values from the K_d^{clim} model. Figures 4.3, 4.4 and 4.5 show Chl values at 0, 50 and 100 m respectively. In each of the three figures, only four months are chosen (one for each season, i.e. March, June, September and December), and the composite images consist of 3 columns: the first one displays the model output with the use of K_d^{var} (units of $mg\,m^{-3}$), the middle column shows the difference between K_d^{var} and K_d^{clim} simulations (units of $mg\,m^{-3}$), whereas the last column depicts the difference, normalized with K_d^{clim} model results (unitless).

Looking at surface values in Figure 4.3, highest Chl concentrations are observed in March for the western basin (up to 0.75 $mg\,m^{-3}$ in the North Western Mediterranean), while the rest of the basin displays oligotrophic values (lower than 0.2 $mg\,m^{-3}$), which holds true for all regions in June and September, with values increasing again in December in the Western Mediterranean (0.4 $mg\,m^{-3}$). Surface Chl dynamics corresponds well to the K_d^{var} spatio-temporal distribution, shown in Figure 4.1.The second and third columns, which depict the relative and normalized differences between two model outputs, further support the spatial patterns observed in Figure 4.2, although at a first glance much less directly so. It should be underlined however that the scale of variations is quite low (the second column showing maximum anomalies of $\pm$ 0.2 $mg\,m^{-3}$, although the scale reaches only 0.05 $mg\,m^{-3}$), corresponding to 40% of the Chl values obtained by K_d^{clim}. Results from the updated model show up to 30% higher Chl values in western regions, which results in a maximum increase of 0.2 $mg\,m^{-3}$. Inversely, almost 30% lower concentrations can be spotted in the Levantine and Ionian regions, both peaking in March, which corresponds to a even lower relative decrease in Chl concentration magnitudes (of around 0.03 $mg\,m^{-3}$). Even though the normalized differences from Figure 4.2 show negative values with small patches of increased K_d^{var}, the variation on magnitudes in consideration is so low that they result in a very small impact on Chl changes. The model output difference decreases to almost-null in September with a slight increase in December.

In Figure 4.4, major differences emerge in March in western subbasins, spreading and shifting towards east during summer (in June), although resulting in lower magnitudes. The observed layer could also correspond to the DCM depths at western basins [Boldrin et al., 2002], since the enhanced values persist until September, which corresponds to the seasonal DCM dynamics in the west, appearing between May and October. [Lavigne et al., 2015]. Additionally, Figure 4.5 shows a significant patchiness in the eastern basin, which could be due to mesoscale features, such as the Ionian Cyclone [Fusco et al., 2003]. Moreover, maximum Chl concentrations at 100 m depth (Figure 4.5) are observed in the east (0.4 $mg\,m^{-3}$), which is in agreement with the DCM depth late spring formation and stabilization throughout the summer and autumn months, i.e. from April to November [Lavigne et al., 2015].

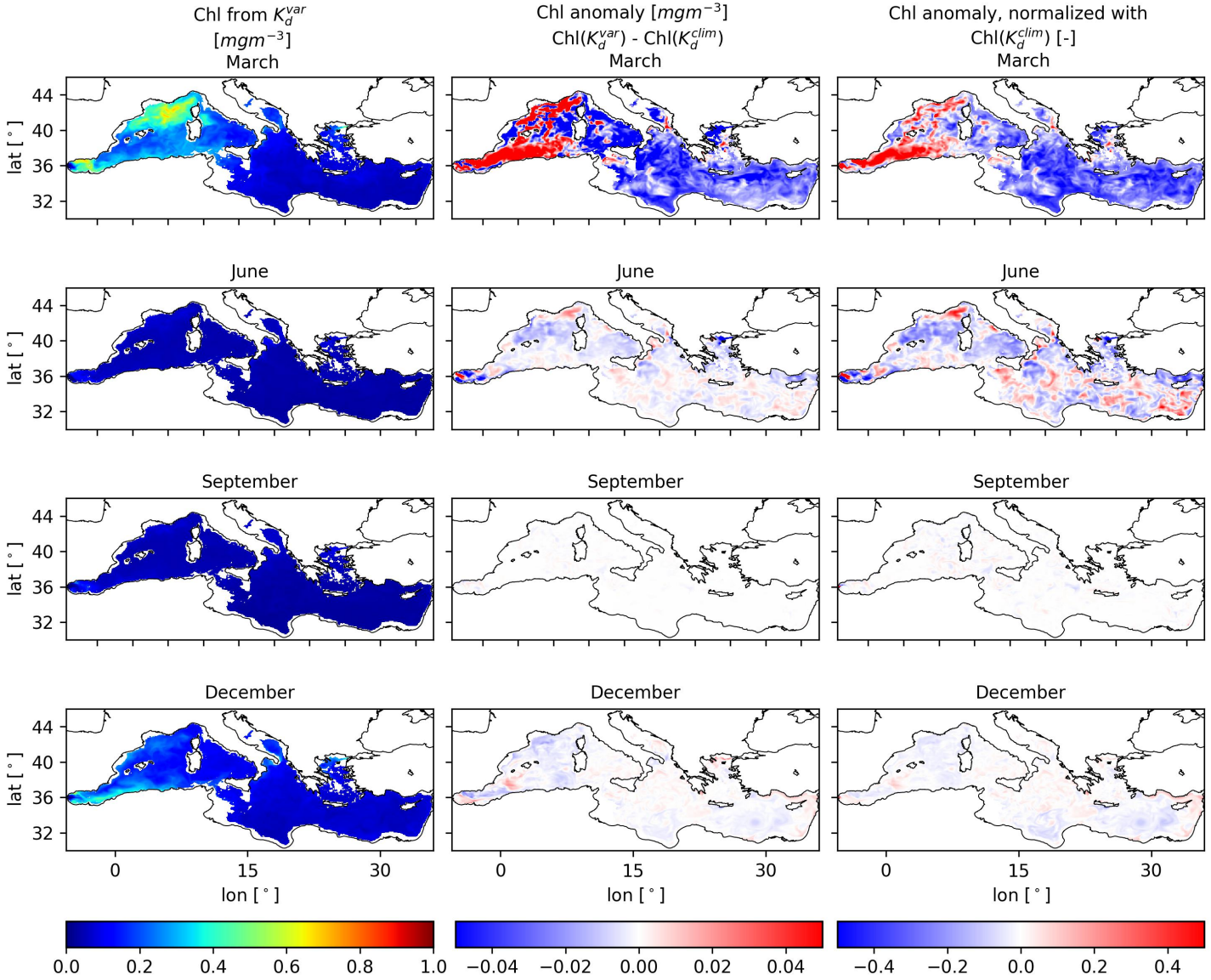

Figure 4.3. Surface Chl output for four months. The first column displays results from the reanalysis with K_d^{var} (units of $mg\,m^{-3}$), the middle one shows the difference between K_d^{var} and K_d^{clim} simulations (units of $mg\,m^{-3}$), whereas the last column depicts the difference, normalized with K_d^{clim} model results (unitless).

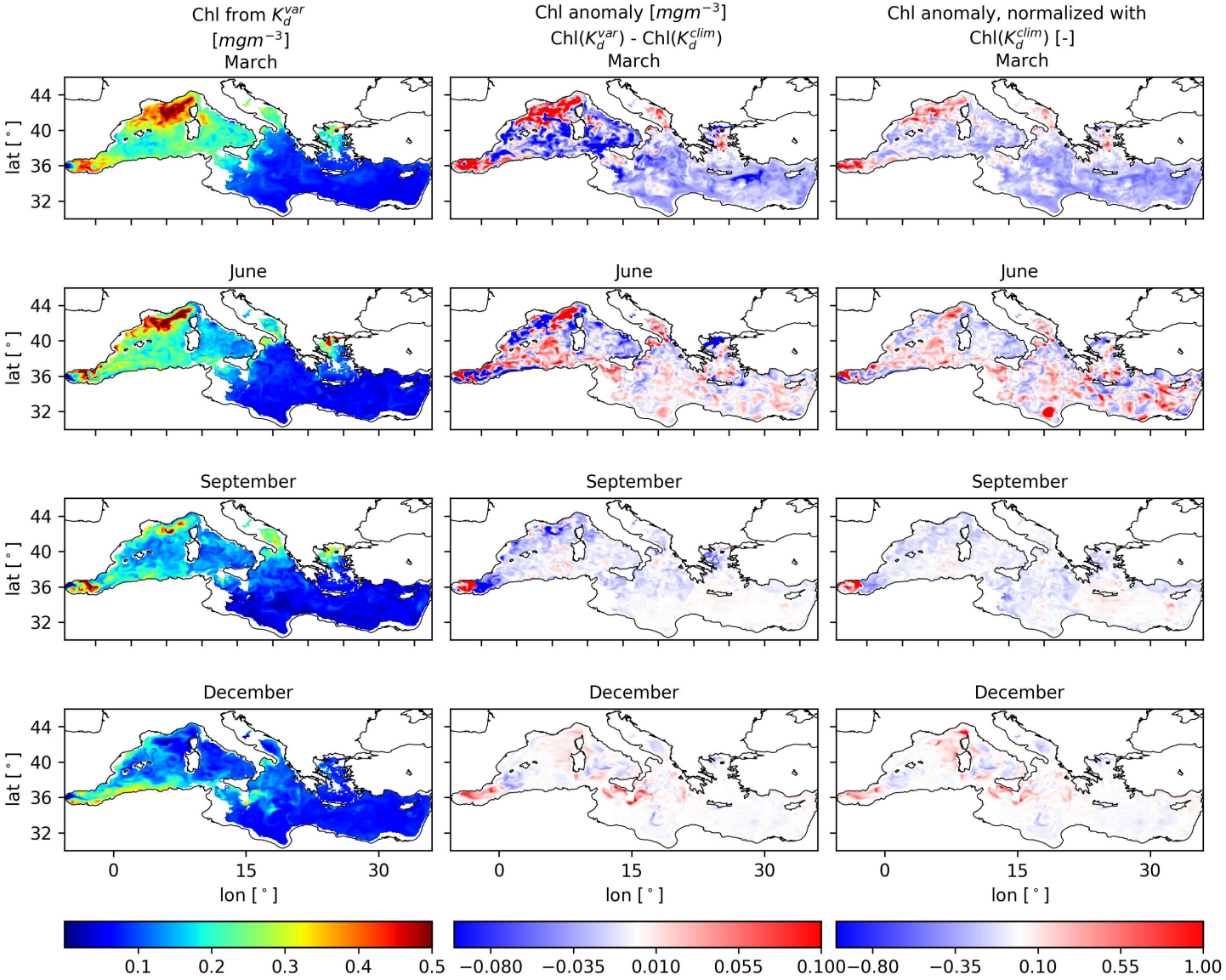

Figure 4.4. Chl output for four months at 50 m. The first column displays results from the reanalysis with K_d^{var} (units of $mg\,m^{-3}$), the middle one shows the difference between K_d^{var} and K_d^{clim} simulations (units of $mg\,m^{-3}$), whereas the last column depicts the difference, normalized with K_d^{clim} model results (unitless).

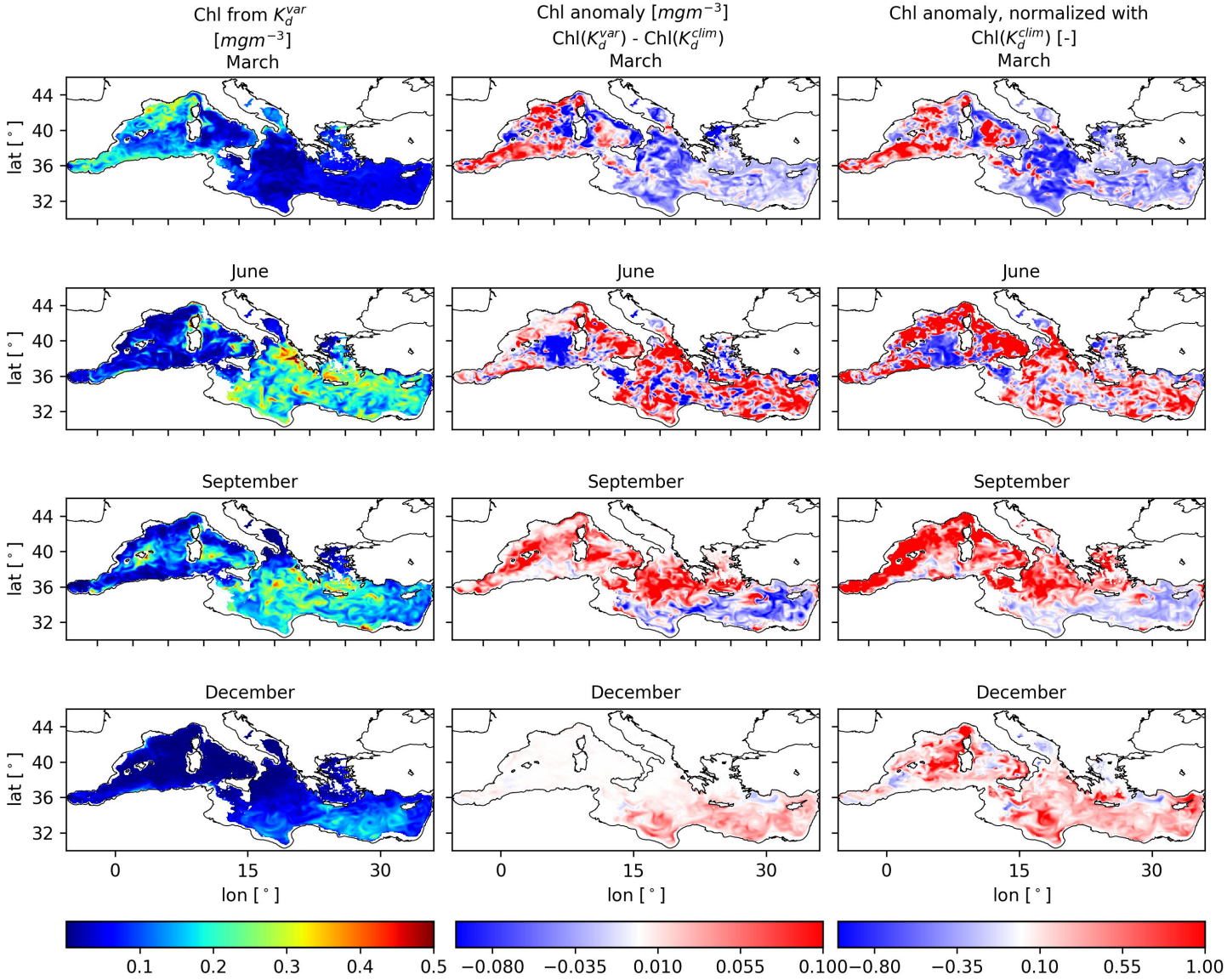

Figure 4.5. Chl output for four months at 100 m. The first column displays results from the reanalysis with K_d^{var} (units of $mg\,m^{-3}$), the middle one shows the difference between K_d^{var} and K_d^{clim} (units of $mg\,m^{-3}$), whereas the last column depicts the difference, normalized with K_d^{clim} results (unitless).

Higher variations could be explained also due to a shift in DCM depth, which cannot be seen from maps. Thus, Hovmöller diagrams are shown in Figures 4.6 and 4.7), for the Eastern Levantine and North-Western Mediterranean respectively, which are organized as follows: the top image shows monthly mean Chl values from the reanalysis with K_d^{var}, whereas the second one results from simulations with K_d^{clim}. The bottom figure depicts Chl results from the difference between K_d^{var} and K_d^{clim} reanalyses.

Figure 4.6 shows deeper DCM, seasonally oscillating between 100 and 140 m, which results from lower K_d ($K_d^{var} < K_d^{clim}$) also shown in Figure 4.2. The June subfigure at 100 m in Figure 4.5 could thus explain the enhancement, which is most likely due to such a shift in DCM.

Figure 4.7 in the North-Western Mediterranean displays a more complex behaviour, with strong vertical mixing intermissions, especially in 2005 2007 and 2013, however resulting in shallower DCM in early spring and late autumn and deeper DCM from April to July, which is in agreement with the variations shown in Figure 4.2. Figure 4.7 shows DCM ranging mostly between 60 and 80 m, which is in agreement with findings in Chapter 3.

Further elaborations on DCM variations will be elucidated in section 4.3.3.

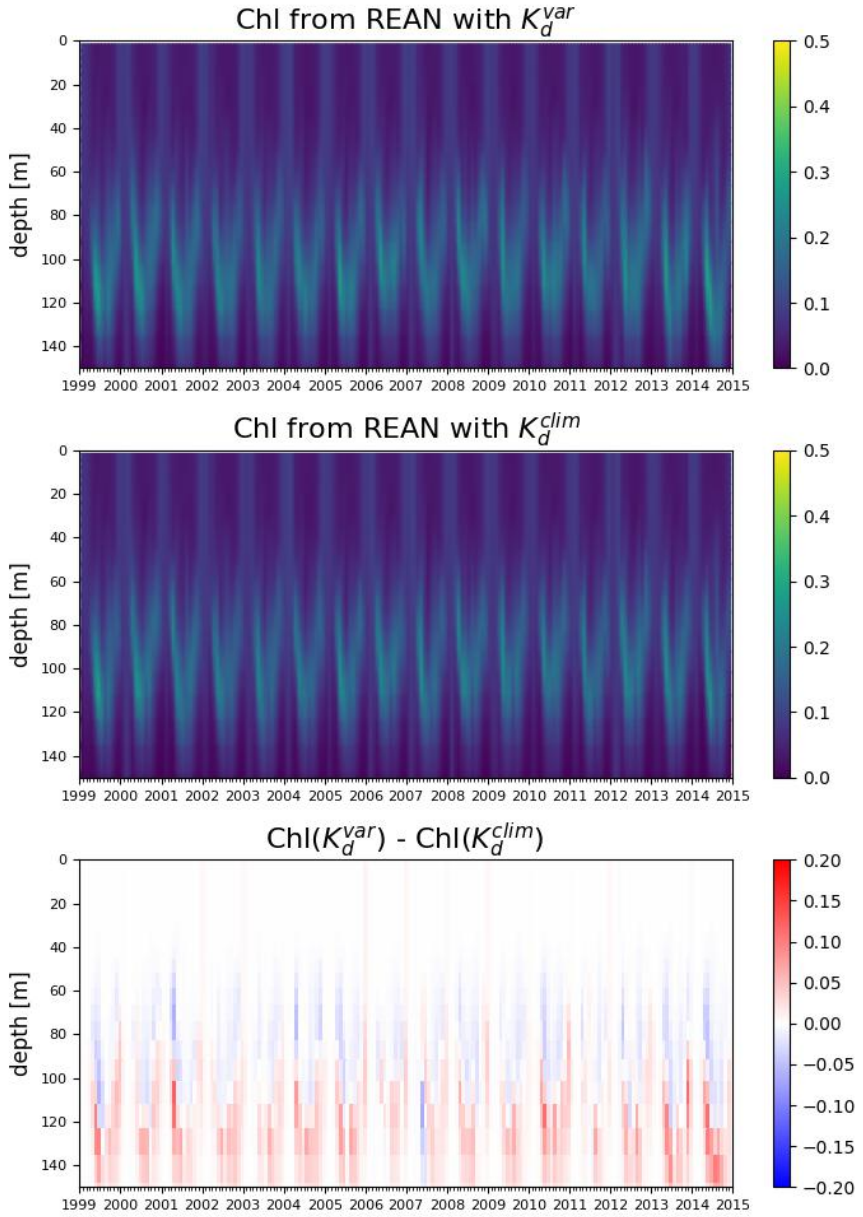

Figure 4.6. Hovmöller plots for the Eastern Levantine. The first image shows a time series of monthly mean Chl values from the reanalysis (REAN) with K_d^{var}, whereas the second one results from simulations with K_d^{clim}. The bottom figure depicts Chl results from the difference between K_d^{var} and K_d^{clim} reanalyses.

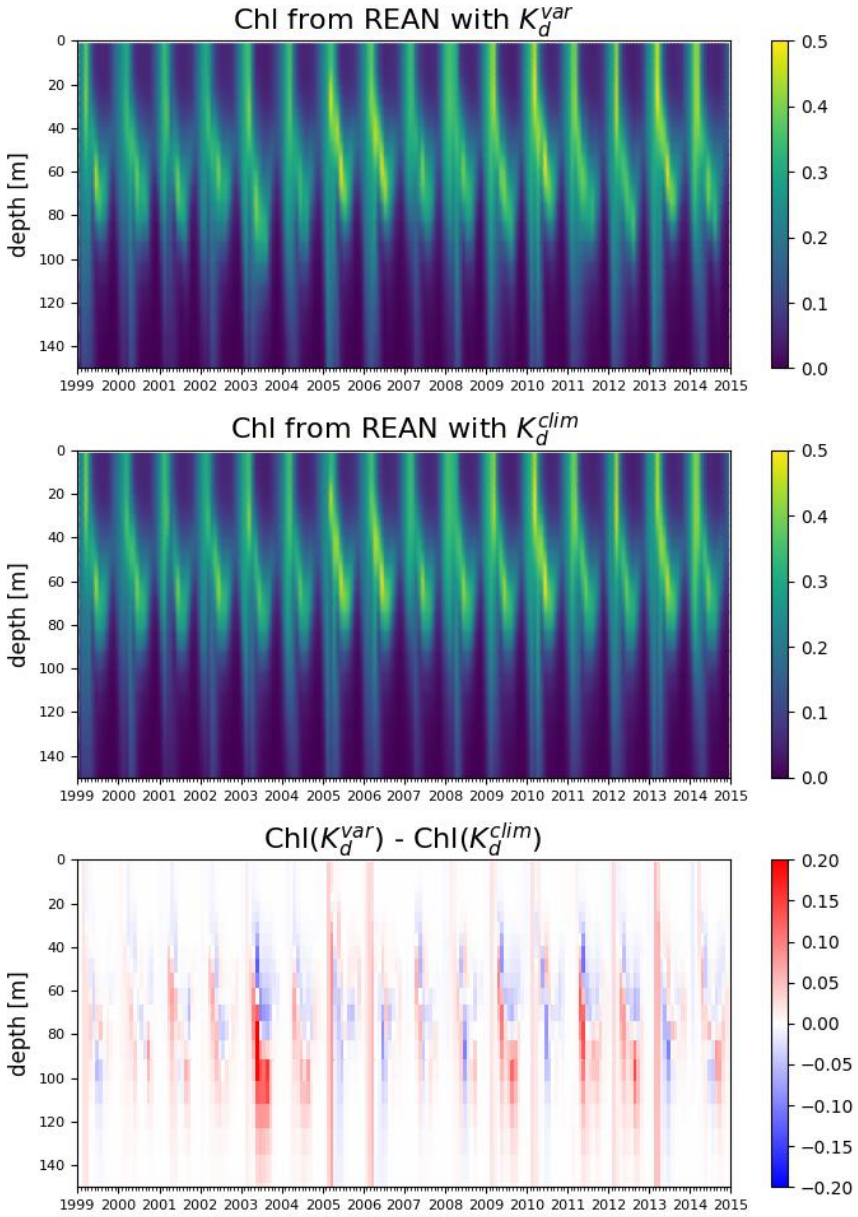

Figure 4.7. Hovmöller plots for the North Western Mediterranean subbasin. The first image shows a time series of monthly mean Chl values from the reanalysis (REAN) with K_d^{var}, whereas the second one results from simulations with K_d^{clim}. The bottom figure depicts Chl results from the difference between K_d^{var} and K_d^{clim} reanalyses.

4.3.2 Evaluation of model output variability on seasonal and interannual scales

Statistically, the model Chl output was quantified at the surface in terms of three different indicators: the interannual, seasonal and monthly variability respectively, shown in Figure 4.8. Analyses were done for each of the 16 subbasins, obtaining one number per each as a final results, all of which were finally normalized with the mean Chl value for the entire Mediterranean Sea (hereafter denoted as A). All figures in the second column depict enhanced variability (i.e. K_d^{var} has a larger variability than K_d^{clim}) in red and reduced in blue.

The interannual variability was calculated as follows: maximum Chl values were obtained for each of the simulated years, after which the standard deviation was computed and normalized with A. This allows to quantify the changes in maximum Chl peaks from year to year and estimate how the two models differ in the output. The first row in Figure 4.8 depicts enhanced variability for 5 out of 12 subbasins for K_d^{var} up to 20% in the Aegean, Tyrrhenian and Eastern Ionian. Inversely, a decrease is shown in the Western subbasins, most prominently in the North Western Mediterranean and the Eastern Levantine (15% and 20% respectively).

The indicator of seasonal variability was obtained by having evaluated periods of maximum (from January to March) and minimum (from July to September) Chl concentrations. For every year, a mean value for both defined periods and their difference were calculated. As a final estimator, the mean value of all the annual differences was obtained and normalized with A. As shown in the second row of Figure 4.8, the K_d^{var} model decreases the seasonal variability in all subbasins, save for the North Western Mediterranean (with an increase of more than 5%) and the Southern Adriatic.

The monthly variability estimation was achieved with the calculation of a climatological year for both data sets. The standard deviation of their anomaly (K_d^{var} - K_d^{clim}) was divided with A. The variability ranges within the 1% and it is increased for western subbasins, the Ionian and the Levantine regions and decreased for the Adriatic and Aegean Seas.

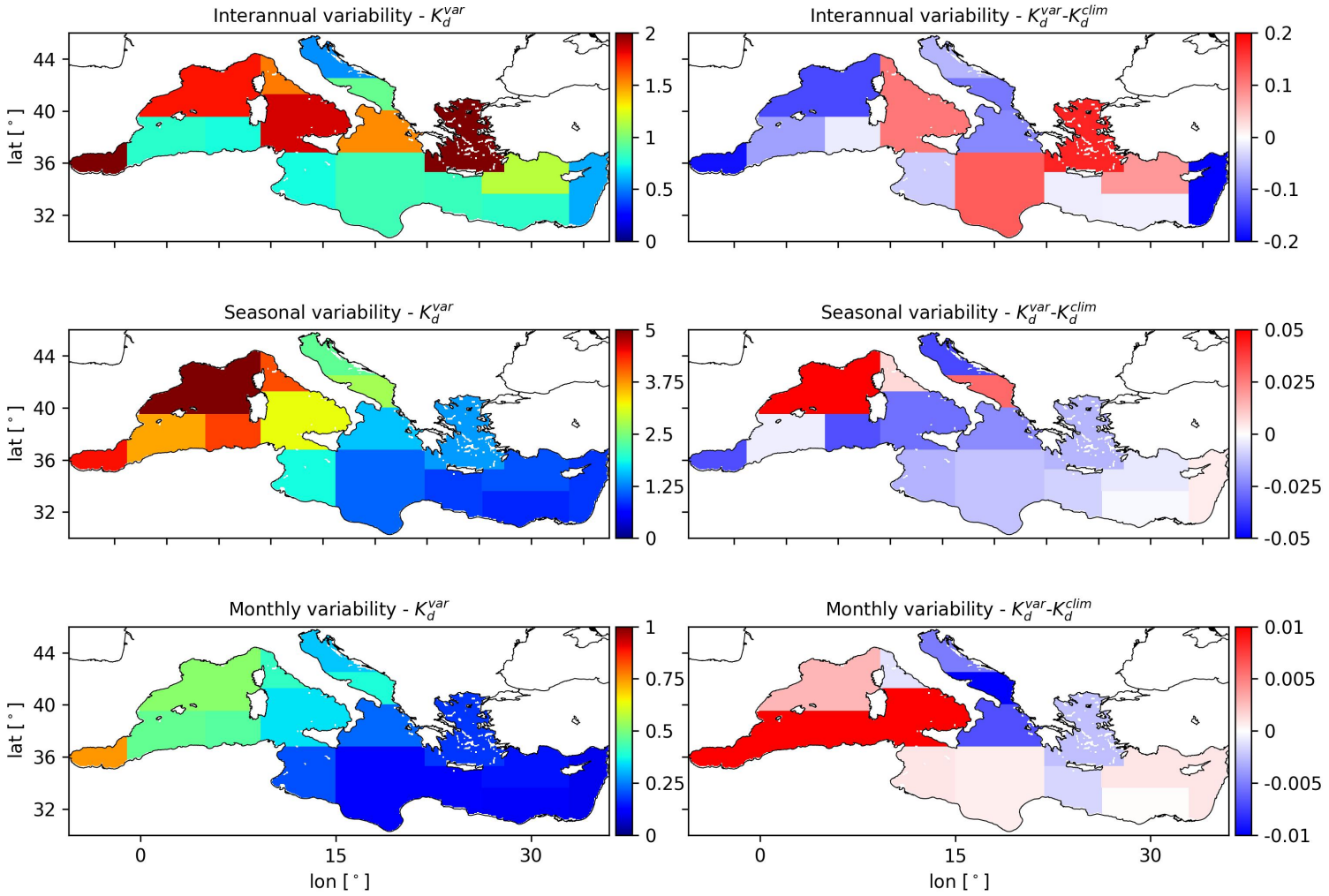

Figure 4.8. Surface Chl model output quantification in terms of three statistical parameters: interannual seasonal and monthly variability (shown row-wise). The first column shows relative values for K_d^{var}, whereas the second one indicates results from anomalies, i.e. K_d^{var} - K_d^{clim}.

4.3.3 Impact of K_d^{var} on DCM

The deep chlorophyll maximum (DCM) is defined as a subsurface maximum concentration in Chl. The calculation of the DCM followed certain criteria, which were already described in Chapter 2.

Figures 4.9 and 4.10 show monthly mean and standard deviation values calculated with K_d^{var}. Results are shown as bars per each subbasin. Dark blue colours depict western subbasins, following the Adriatic in cyan, Ionian basins in pale orange, and the Levantine region in mid- to dark red. As shown previously in Chapter 2 with the BGC-Argo data set analysis, the model output confirms the presence of the longitudinal gradient, as well as the disappearance of the feature during winter months due to enhanced convective mixing which destabilizes the water column. DCM depths are in the Levantine ranging from 80 to 100 m in spring, up to 120 m in summer months, with corresponding mean Chl concentrations of 0.2 $mg\,m^{-3}$, which is consistent with results in Christaki et al. [2001] and Dolan et al. [2002]. The DCM in western basins ranges from 60 m in spring and autumn, increasing in summer to 70 or 80 m, with corresponding Chl values of 0.4 $mg\,m^{-3}$ in May which decrease during summer and autumn to 0.35 and 0.25 $mg\,m^{-3}$ respectively. Eastern subbasins retain similar values throughout the entire period of the DCM occurrence, oscillating around 0.2 and 0.3 $mg\,m^{-3}$, with depths increasing from 90 to 120 m between April and July, followed by a decrease from August to November (from 110 to 90 m).

The feature of major interest in this study is however the difference in DCM between the two reanalyses, which are shown in Figures 4.11 and 4.12 for DCM depths and Chl values respectively.

It should be noted that the standard deviation values take into consideration the variations in model vertical layer grid thickness, which is increasing with depth. Thus, if a DCM from one simulation results from a layer with larger thickness, the difference will take the standard deviation of the latter and hence take into consideration the maximum range of possible values within the model grid.

Major differences in DCM depth (Figure 4.11) arise in the Ionian subbasins in August/September, with a mean difference of 12 m and a standard deviation of 8 m, however resulting in minimal differences in terms of Chl concentrations (less than 0.01 $mg\,m^{-3}$). In the majority of subbasins, the DCM depth increases with the use of K_d^{var}, except for few cases eastern region from May to July and the western subbasins in October. Chl magnitudes (Figure 4.12) decrease most prominently in spring months for the western basin and the Adriatic, from up to 0.05 $mg\,m^{-3}$ in June towards 0.02 $mg\,m^{-3}$ in September.

On average, the DCM depth increases for 10-12 m with the updated light

model, which is consistent with the initial expectations of the analysis. Chl magnitudes tend to decrease in western subbasins from March to July and in September between 0.02 and 0.04 $mg\,m^{-3}$, while eastern subbasins show an increase in early spring, August and December (up to 0.02 $mg\,m^{-3}$).

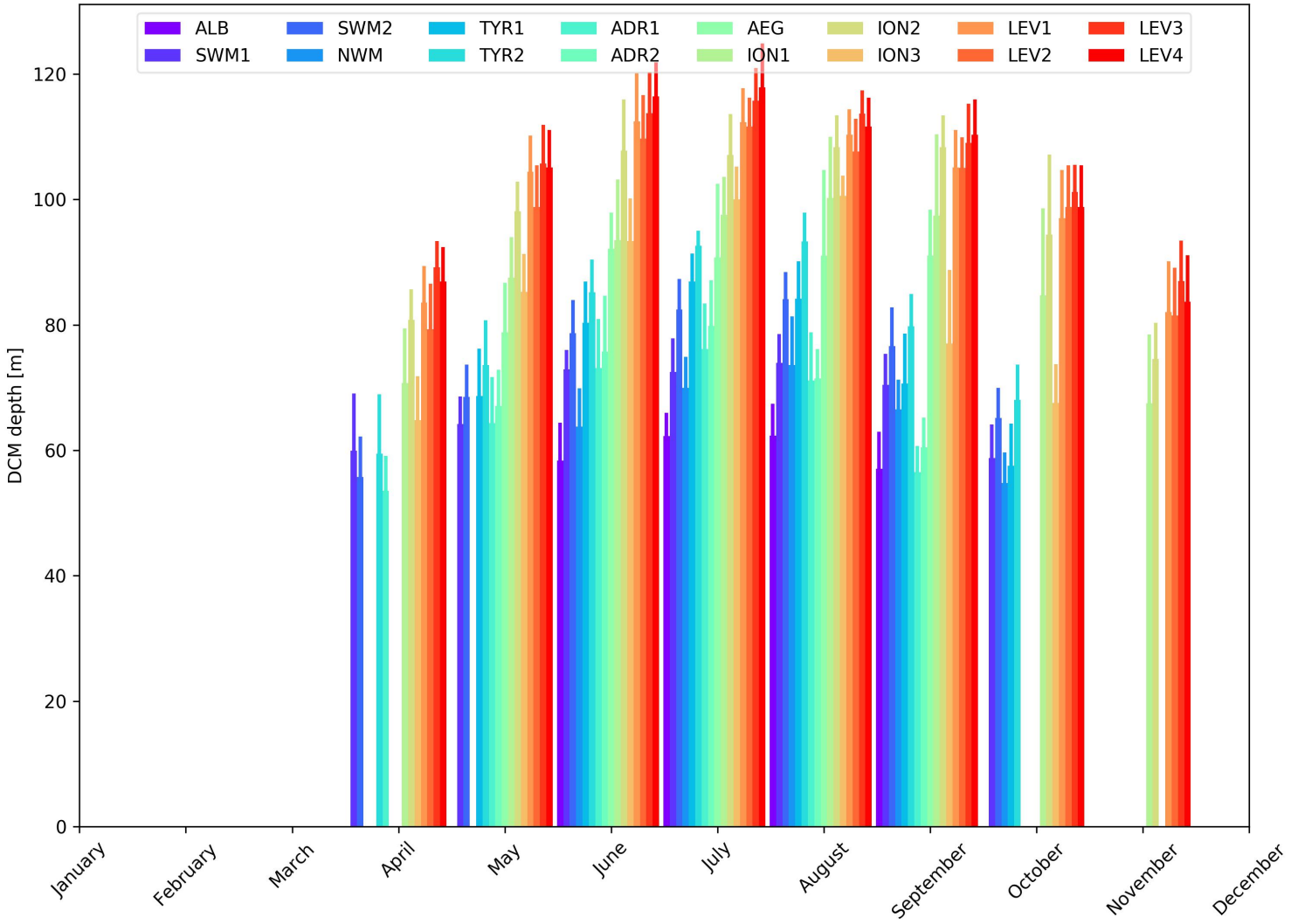

Figure 4.9. The DCM depth monthly mean and standard deviation values calculated with K_d^{var}, both shown as bar plots with colours corresponding to each of the 16 subbasins. Standard deviation bars are depicted as narrower lines with the same colour as the mean one.

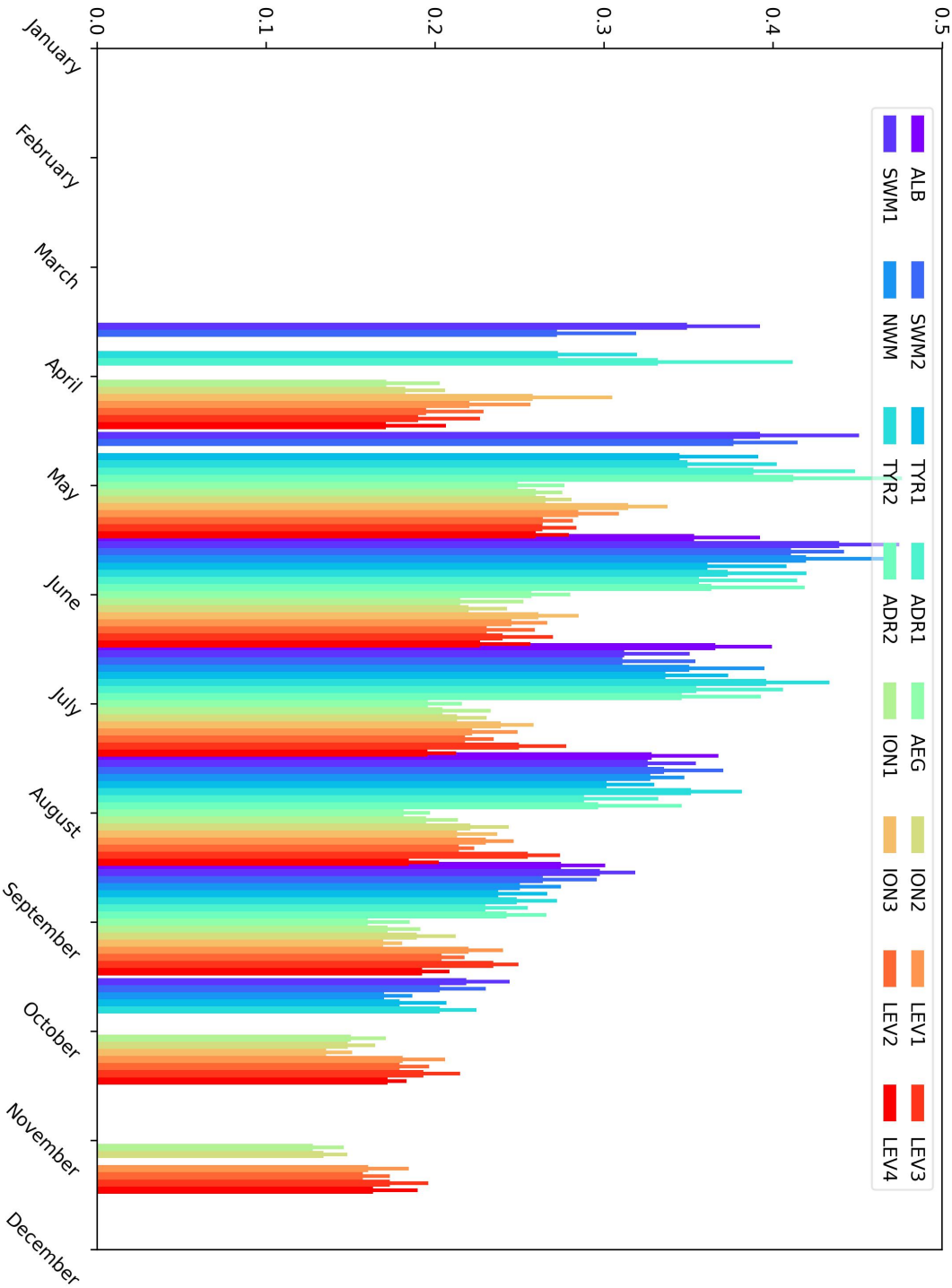

Figure 4.10. Chl at DCM monthly mean and standard deviation values calculated with K_d^{var}, both shown as bar plots with colours corresponding to each of the 16 subbasins. Standard deviation bars are depicted as narrower lines with the same colour as the mean one.

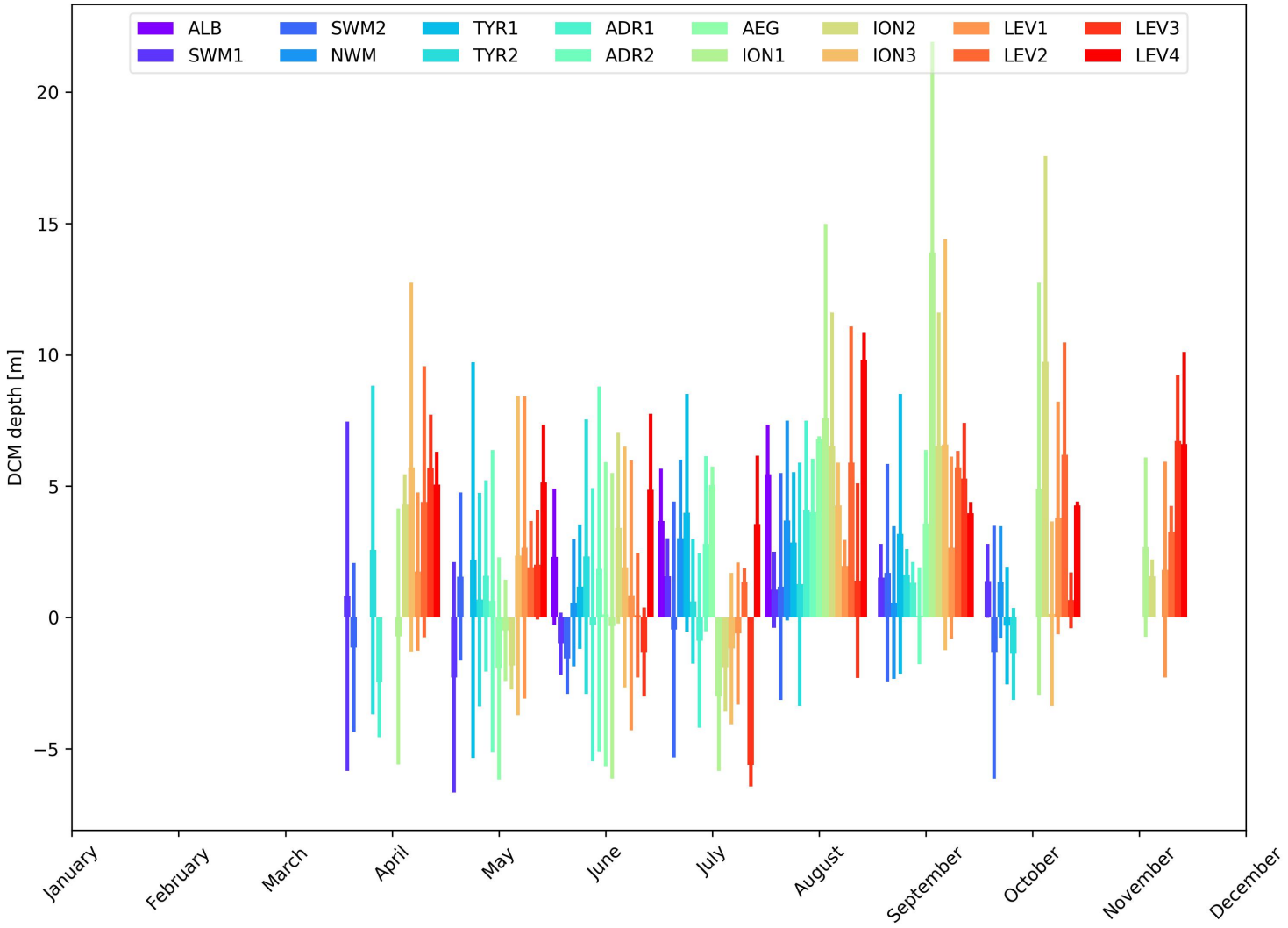

Figure 4.11. The DCM depth monthly mean and standard deviation values calculated as the difference between two model outputs, i.e. K_d^{var} - K_d^{clim}. Both mean and standard deviation values are shown as bar plots with colours corresponding to each of the 16 subbasins. Standard deviation bars are depicted as narrower lines with the same colour as the mean one.

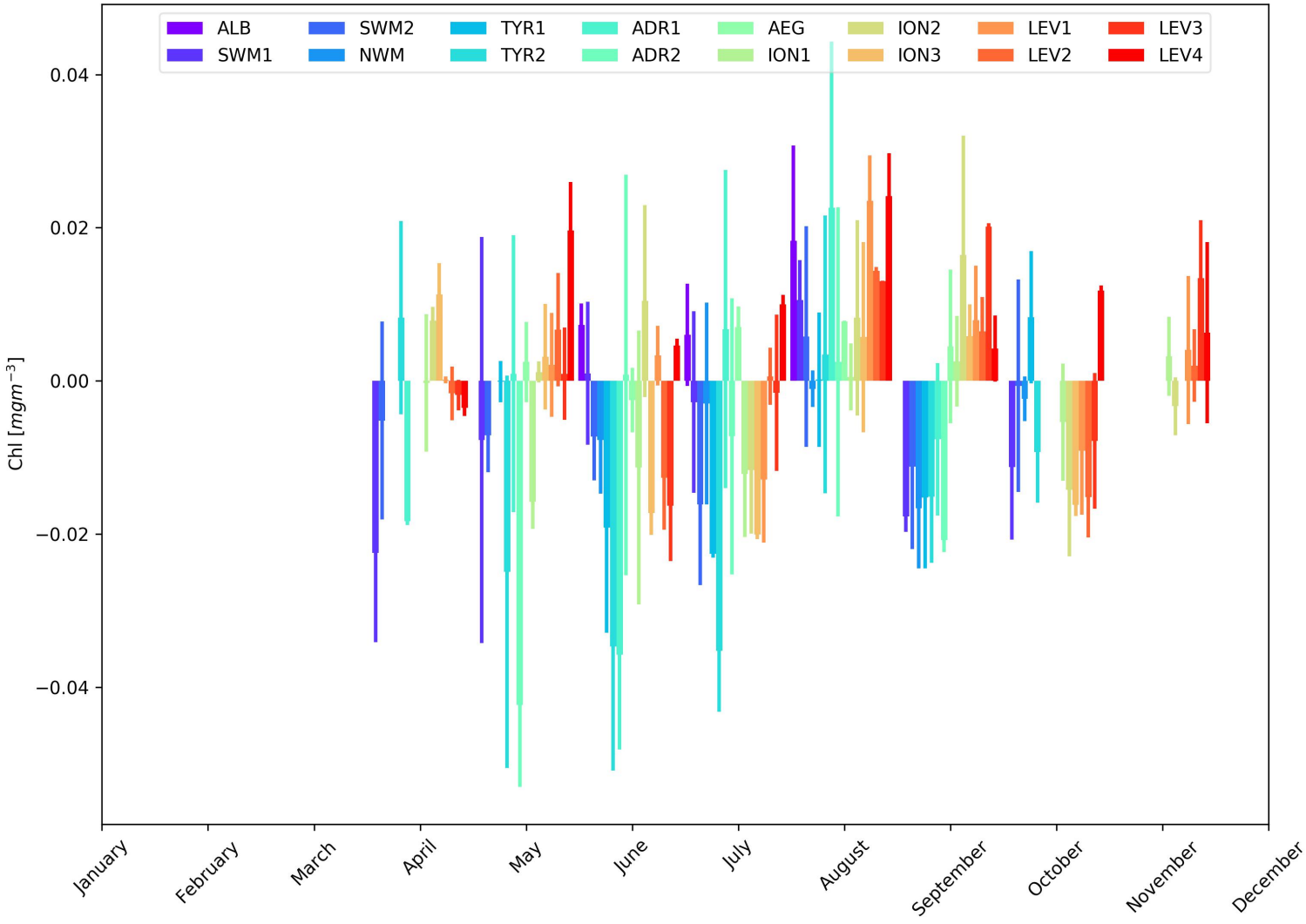

Figure 4.12. Chl at DCM monthly mean and standard deviation values calculated as the difference between two model outputs, i.e. K_d^{var} - K_d^{clim}. Both mean and standard deviation values are shown as bar plots with colours corresponding to each of the 16 subbasins. Standard deviation bars are depicted as narrower lines with the same colour as the mean one.

4.3.4 Impact of K_d^{var} on the CMEMS product quality

For CMEMS product quality assessment purposes, a quality-controlled data set of bio-optical variables from BGC-Argo floats was used, previously described in Chapters 2 and 3. The reader is appointed to the Figure 2.1 for the spatial distribution of floats. A point-by-point match-up was carried out with fluorescence-derived Chl data, which was followed by a spatio-temporal division (16 subbasins divided seasonally). The seasons were defined as previously in Chapter 2: winter is from the period between January and March, spring from April to June, summer from July to September, and autumn from October to December. The product quality was evaluated with three statistical parameters: bias, root mean square error (RMSE) and the Pearson correlation coefficient (ρ), which were calculated following equations 4.6 to 4.9:

$$BIAS = \frac{1}{n}\Sigma_{i=1}^{n}\Big(x_i - y_i\Big) \tag{4.6}$$

$$RMSE = \sqrt{\frac{1}{n}\Sigma_{i=1}^{n}\Big(x_i - y_i\Big)^2} \tag{4.7}$$

$$cov_{x,y} = \frac{\sum_{i=1}^{n}(x_i - \bar{x})(y_i - \bar{y})}{n-1}. \tag{4.8}$$

$$\rho = \frac{\mathrm{cov}(x,y)}{\sigma_x \sigma_y} \tag{4.9}$$

where x equals Chl from reanalyses and y denotes Chl from data (i.e. BGC-Argo floats). σ represents the standard deviation of the model/data values.

Figure 4.13 shows statistical parameters for the match-up between fluorescence -derived Chl data from BGC-Argo floats and model results from K_d^{var} simulations. The top figure shows negative biases for the majority of cases, indicating that the model underestimates Chl for all regions and seasons, especially during spring in the North-Western Mediterranean (resulting in almost 0.3 $mg\,m^{-3}$). Similarly, RMSE ranges between 0.1 and 0.2 $mg\,m^{-3}$ for eastern and from 0.2 to 0.3 $mg\,m^{-3}$ for western subbasins (with an anomalous value of 0.9 $mg\,m^{-3}$). Correlation coefficients span from 0.30 during spring for the Northern Levantine, albeit resulting from a low number of profiles to validate the model with (4, see Table 2.2), to 0.8, which is also the result of only one profile to compare the model output with. After the omission of subbasins and seasons with an insufficient quantity of profiles, it can be concluded that the correlation coefficients range from 0.40 to 0.70.

In Figure 4.14, same statistical parameters are compared for the match-up of both model outputs as their difference, i.e. K_d^{var} - K_d^{clim}. Highest bias is observed in the North Western Mediterranean during winter, which significantly impacts also the mean seasonal bias for the entire basin shown in Table 4.2. Similarly, negative values observed in the South-Western Mediterranean and the Southern Adriatic in spring result in a negative seasonal bias in basin dimensions. Differences diminish in summer and autumn months, with a maximum bias below 0.01 $mg\,m^{-3}$. RMSE decreases with the use of K_d^{var} (negative values), especially for spring periods in most subbasins, while the correlation coefficient also increases in the majority of cases between 0.10 and 0.15.

The summarizing Table 4.2 shows the average statistics for the entire basin per season. The total number of match-ups used for each seasonal assessment spans from less than 19000 in autumn to almost 32000 for spring months. Bias slightly increases with the use of K_d^{var} during autumn and winter, whereas RMSE is null or decreasing in all 4 seasons. The correlation worsens only during autumn and improves most notably for the spring period.

In conclusion, the statistical analysis from a match-up between BGC-Argo and model outputs shows small impact, with only a slight product quality improvement with the use of an upgraded light model.

Table 4.2. Match-up statistical parameters (bias, RMSE and correlation coefficient) of the difference between the two models skills K_d^{var} and K_d^{clim}

Season	**No. of points**	**BIAS**	**RMSE**	R^2
Winter	29988	0.003	-0.002	0.022
Spring	31969	-0.001	-0.006	0.073
Summer	27574	-0.001	0	0.002
Autumn	18730	0.002	0	-0.002

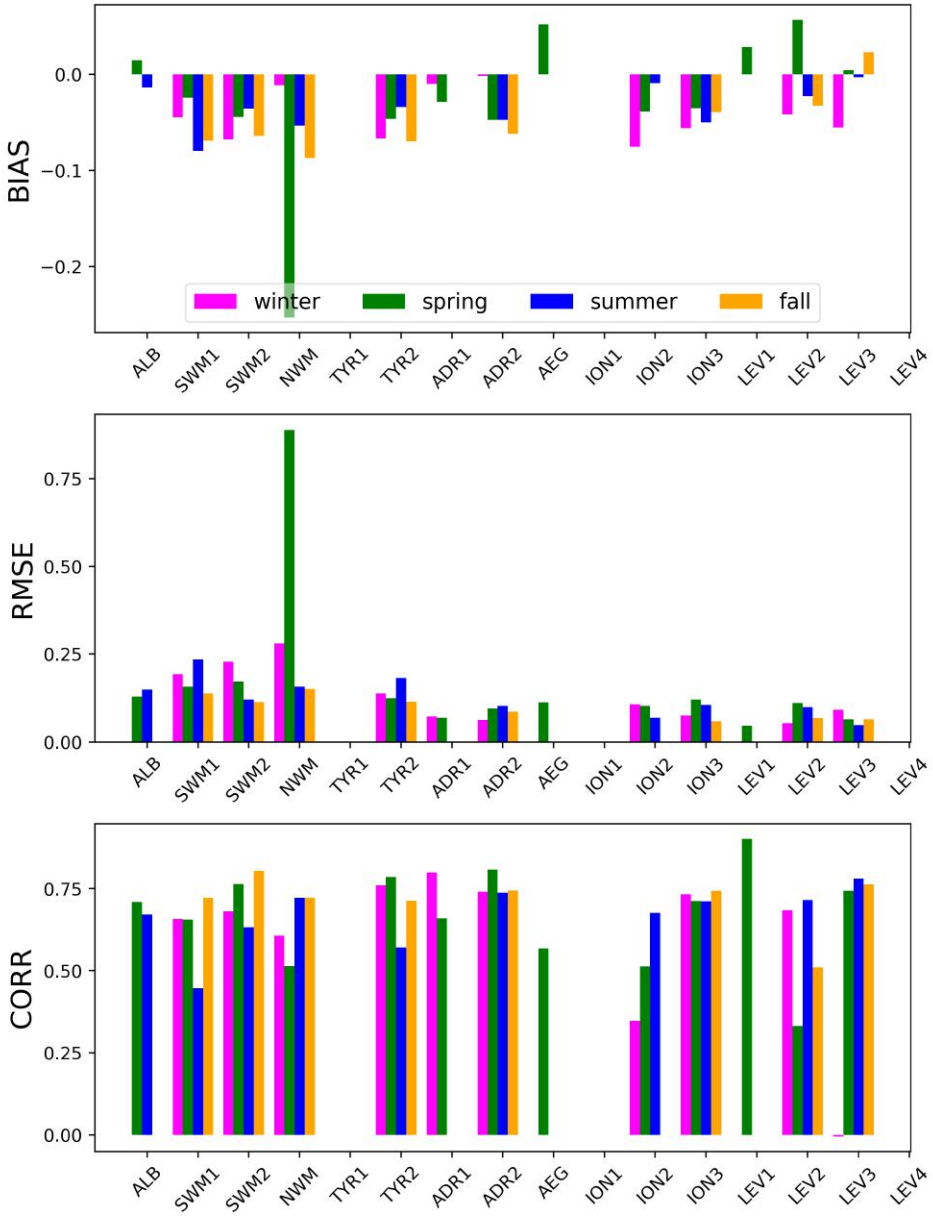

Figure 4.13. Chl match-up of K_d^{var} simulation results and BGC-Argo floats - bias, RMSE and the correlation coefficient.

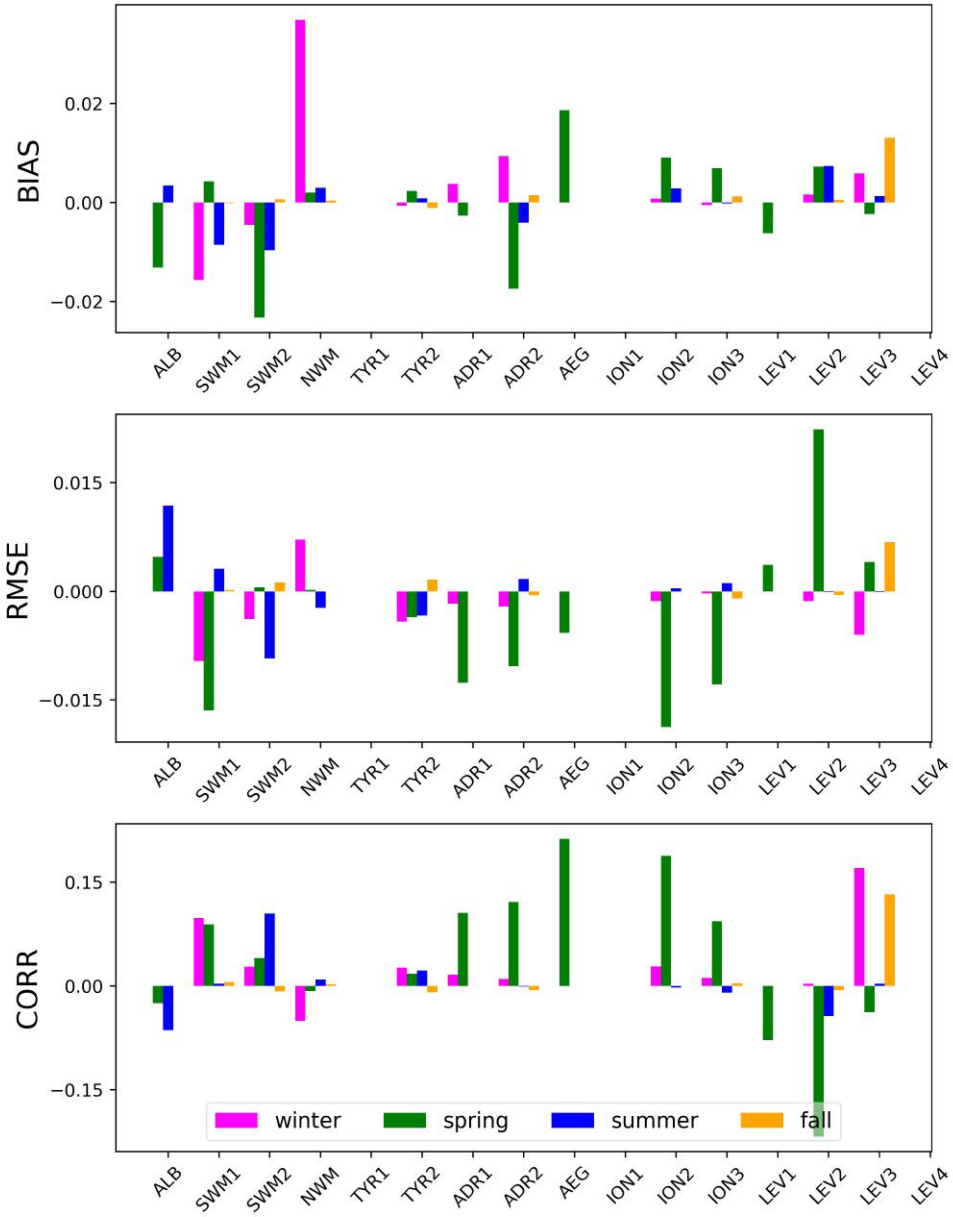

Figure 4.14. Chl match-up of K_d^{var} - K_d^{clim} simulation results with BGC-Argo floats - an estimation of the models' difference through three statistical parameters: bias, RMSE and the correlation coefficient.

4.3.5 Impact of K_d^{var} on specific areas - the DYFAMED case

In order to gather additional insight on the K_d^{var} model performance, a separate data set of HPLC profiles was acquired from the MAREDAT open access data base [Buitenhuis et al., 2013]. As underlined in Chapter 2, fluorescence-derived Chl profiles are prone to several sources of uncertainties and as such, if possible, should be validated with HPLC profiles (although it is seldom possible to do so in (quasi-)synoptic scales due to the floats' Lagrangian dynamics). The MAREDAT data set is however much older compared to the newly deployed BGC-Argo system, and has not been updated since its first publication, thus a comparison of two separate time intervals is shown in Figure 4.15 for the North-Western Mediterranean, which had the largest number of profiles, both from BGC-Argo and the HPLC database. The image is composed of Hovmöller diagrams with monthly mean Chl profiles, organized as follows: the first column is related to the time interval which coincides with the HPLC data collection, i.e. from 1999 to 2005, whereas the second column takes into consideration the 2012 to 2016 period, overlapping with the BGC-Argo data. The first row shows the Chl model output from the K_d^{var} reanalysis, the second row depicts values from in-situ data (HPLC and floats), while the last row results in the difference between model and data outputs. The latter clearly indicates a significant underestimation of the model, displaying differences above 0.5 $mg\,m^{-3}$ for the first 75 m.

Strictly speaking, such a comparison could be dismissed as erroneous due to different spatio-temporal scales of compared products: the model output is a monthly mean value for the entire subbasin, while in-situ data are collected at a specific day and location. In order to at least partially constrain the error, a spatial analysis of available HPLC profiles was done (shown in Figure 4.16) to control the data set distribution. Out of 135 profiles in the entire Mediterranean basin, 101 were located around the BOUSSOLE station, which was the site of frequent monthly DYFAMED cruises [Marty et al., 2002] that took also measurements of phytoplankton pigments for HPLC analyses [Vidussi et al., 2001].

Figure 4.17 was thus restricted to the rectangular region encompassing 101 points from HPLC, showing mean model values only for the corresponding site, thus requiring a very stringent assessment of model performance. The number of floats is reduced, however the completeness of the HPLC time series is preserved. As expected, despite the spatial limitation applied, the bottom row still shows similar variations between model and data outputs.

Such results require further elaboration in order to ascertain the sources

for conspicuously diverging values, which could stem both from a physical (i.e. insufficiently accurate description of convective mixing and thus resulting in a lower nutrient uptake) or bio-optical point of view (omission of scattering, which would enhance the available amount of light in the water column).

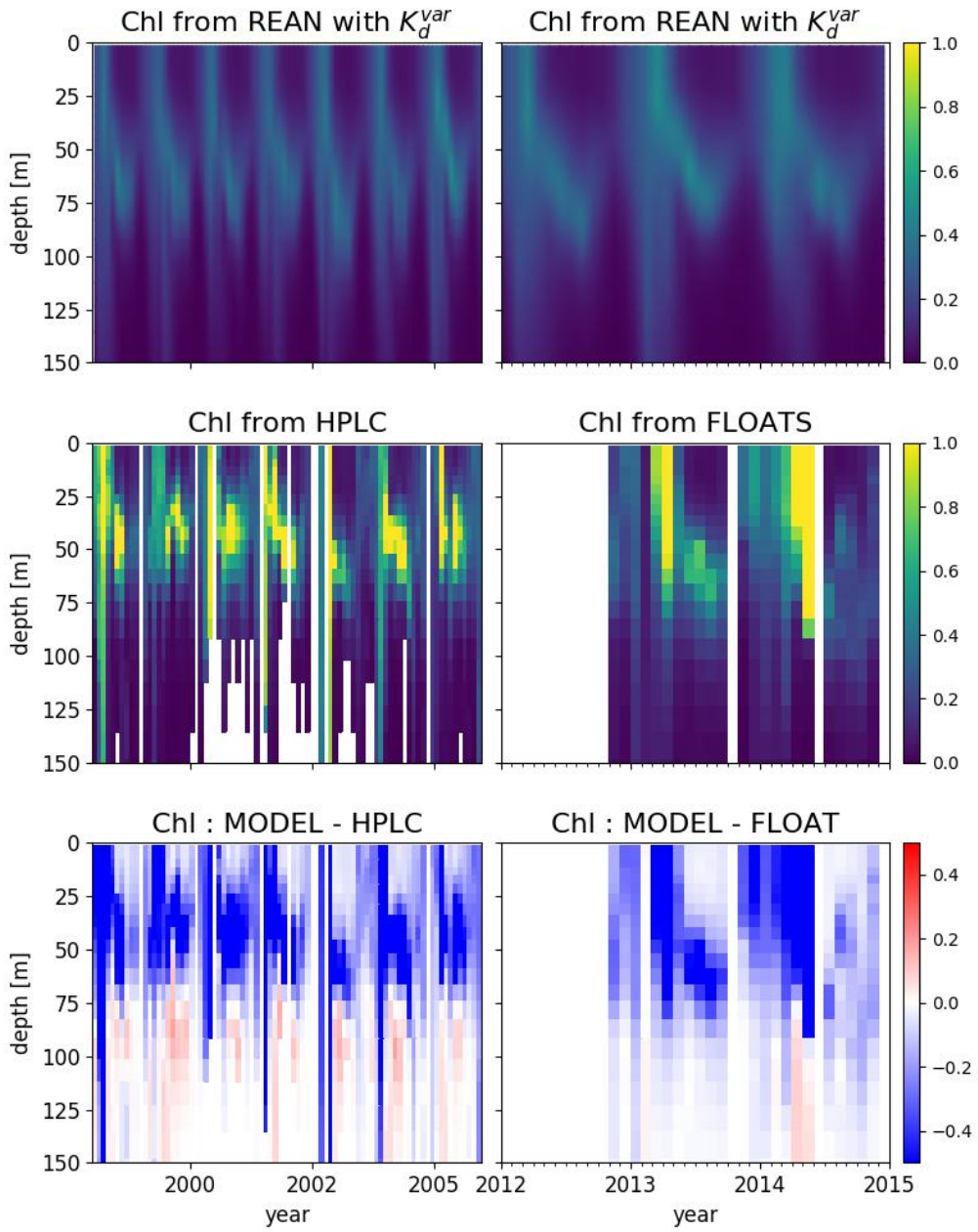

Figure 4.15. Hovmöller diagrams with monthly mean Chl profiles for the North Western Mediterranean subbasin, organized as follows: the first column is related to the time interval which coincides with the HPLC data collection, i.e. from 1999 to 2005, whereas the second column takes into consideration the 2012 to 2016 period, overlapping with the BGC-Argo data. The first row shows the Chl model output from the K_d^{var} reanalysis, the second row depicts values from in-situ data (HPLC and floats), while the last row results in the difference between model and data outputs.

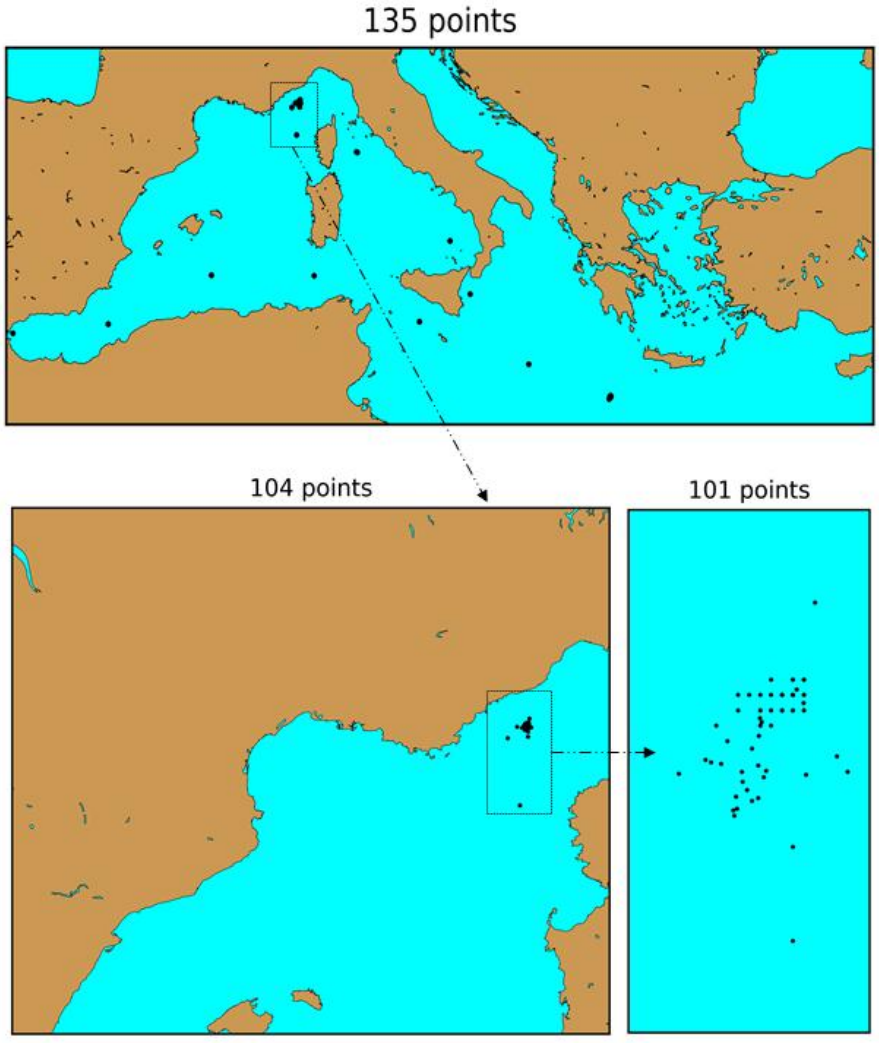

Figure 4.16. A composite image map of the spatial distribution of HPLC profiles. 135 points are present in the entire Mediterranean basin, the bottom left figure shows 104 profiles in the North-Western Mediterranean subbasin, whereas the bottom right figure limits the region to the BOUSSOLE site with data from DYFAMED cruises.

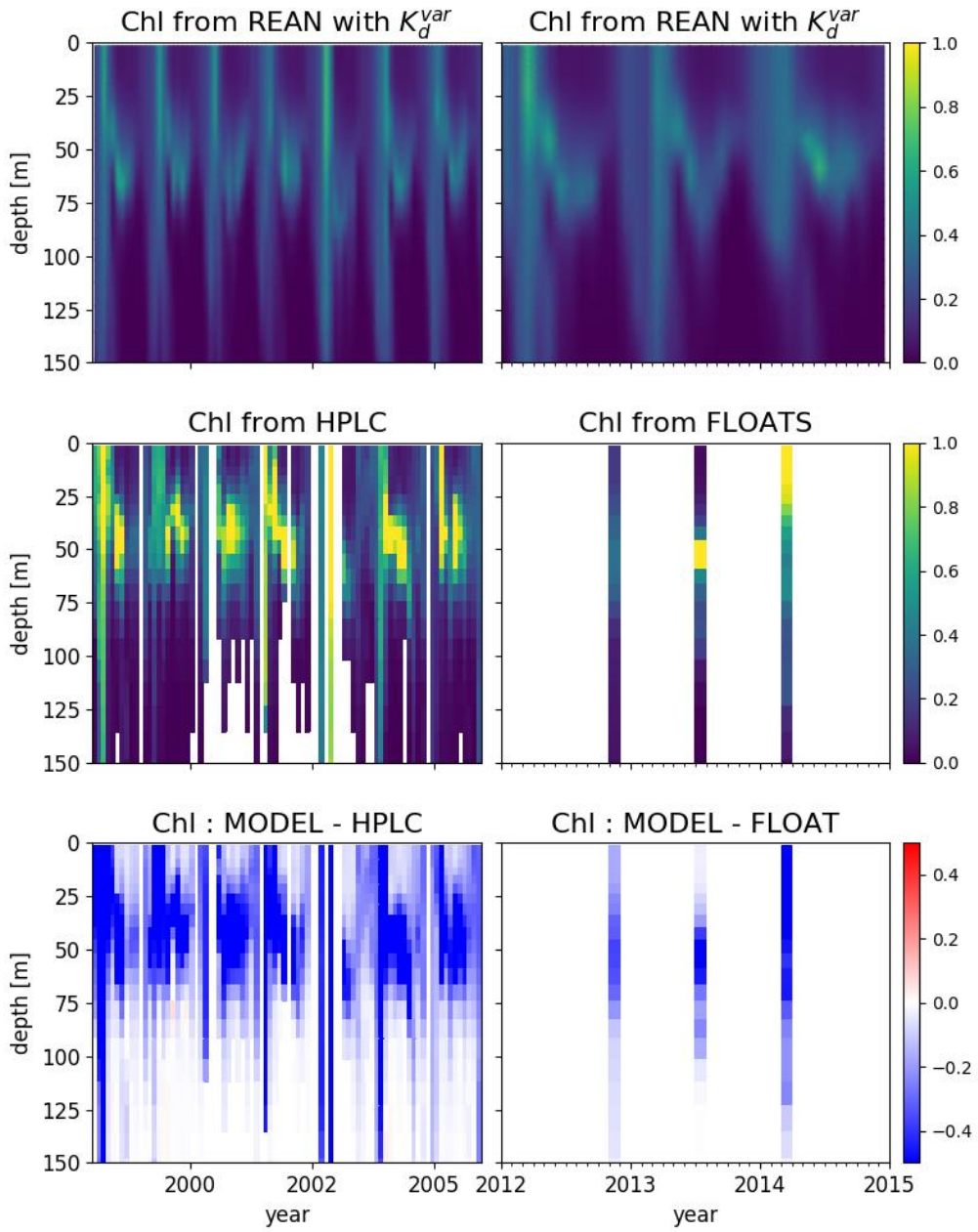

Figure 4.17. Hovmöller diagrams with monthly mean Chl profiles for the reduced spatial region related to DYFAMED HPLC data points. The figure is organized as follows: the first column is related to the time interval which coincides with the HPLC data collection, i.e. from 1999 to 2005, whereas the second column takes into consideration the 2012 to 2016 period, overlapping with the BGC-Argo data. The first row shows the Chl model output from the K_d^{var} reanalysis, the second row depicts values from in-situ data (HPLC and floats), while the last row results in the difference between model and data outputs.

4.3.6 A comparison of diffuse attenuation coefficients from remote sensing and BGC-Argo floats

The concluding section could be arguably located at the beginning of this chapter, before the model tuning procedure, however the text follows rather the chronological order of the analysis, hoping to shed a light on further improvements, which will be elucidated in the summarizing section. As previously described both in the introductory chapter about the development of optics, as well as in Chapter 2, which was dedicated to an in-depth study of the BGC-Argo data set and the derivation of K_d functions, satellite products result from less than 10% of the water-leaving signal and are as such more prone to errors due to inaccurate atmospheric corrections or wrong calibration procedures. BGC-Argo floats, on the other hand, could serve as a ground truth in order to validate AOPs obtained from satellites. With a thorough quality-control procedure, calculating depth derivatives should remove the impact of a changing light field and thus relate them with bio-optical properties (IOPs). Following the rationale of the match-up between Chl values of models versus data, a similar procedure was applied to satellite $K_d(490)$ data and BGC-Argo values, calculated for the first optical depth. Figure 4.18 shows monthly mean values of $K_d(490)$ per subbasin for the period between 2012 and 2016. Weekly satellite data are taken prior to the tuning procedure, i.e., without the multiplication factor of 1.3. Figure 4.19 shows the difference between satellite and BGC-Argo data, resulting in generally higher values from satellites. Few exceptions are seen in January, March, October and November for the North-Western Mediterranean. The Levantine subbasins, for which the model was tuned, prove to have already from 0.10 to 0.15 m^{-1} higher values compared to in-situ measurements.

Figure 4.20 quantifies the difference in terms of the three statistical parameters previously used in the Chl product quality assessment, in this case following a seasonal division of subbasins for better clarity of the images. Highest bias results in all basins for spring and summer months (0.01 m^{-1}) with negative values in winter for western basins and in autumn for the Southern Adriatic. RMSE is highest for the North Western Mediterranean, reaching 0.035 m^{-1} in spring, but on average ranging from 0.01 to 0.02 m^{-1}. Higher correlations are observed for western basins in spring and autumn months, (from 0.6 to 0.8) with drastically lower values in the Levantine region (from 0.1 to 0.4).

Such analyses could be useful for satellite algorithm retrieval validation, as well as for future model tuning. In the present case, the tuning procedure actually corresponds to $K_d(PAR)$ values or higher, which was also shown in Chapter 2.

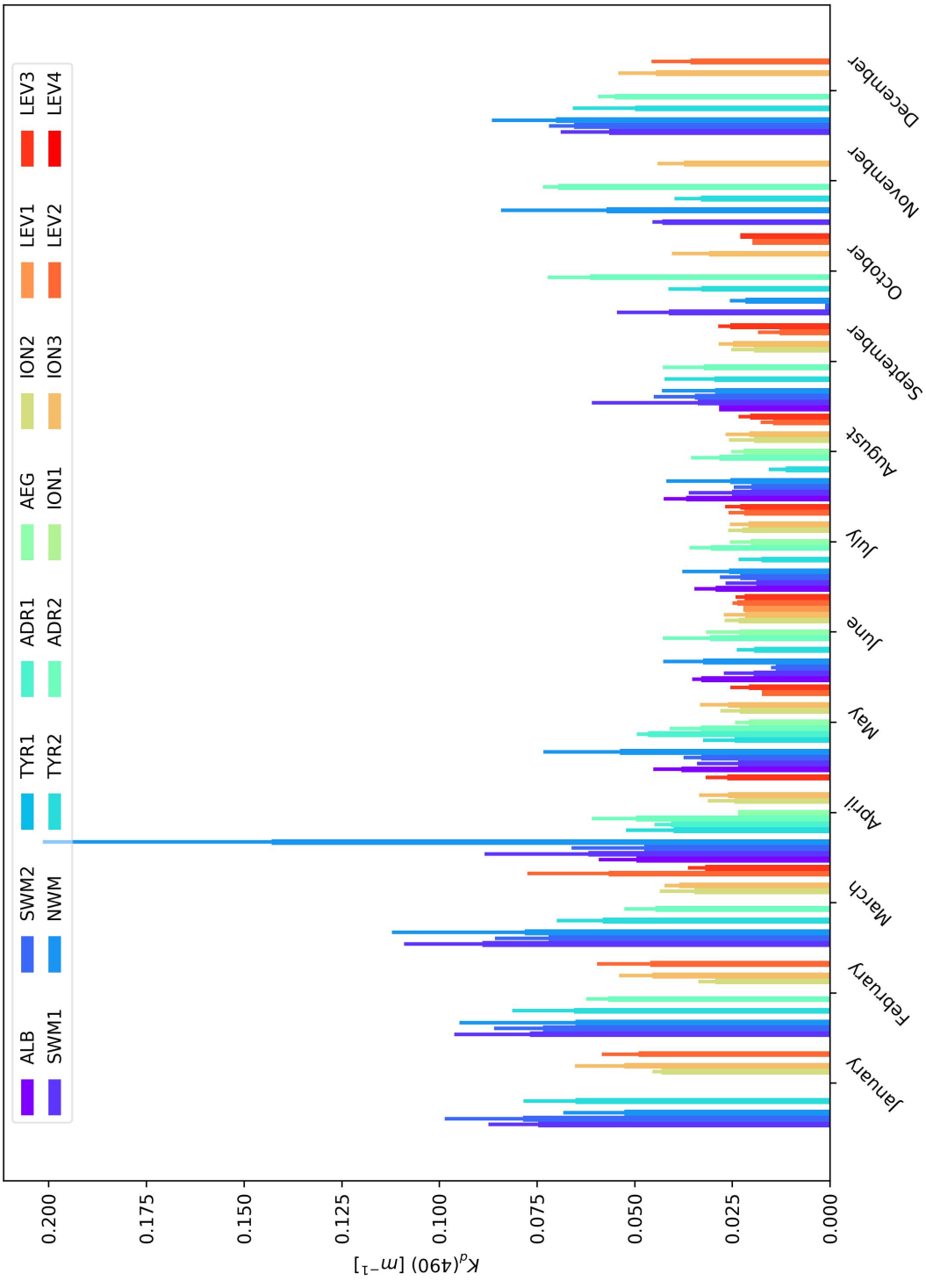

Figure 4.18. Monthly mean $K_d(490)$ values from BGC-Argo floats with standard deviation lines per each subbasin, units of m^{-1}.

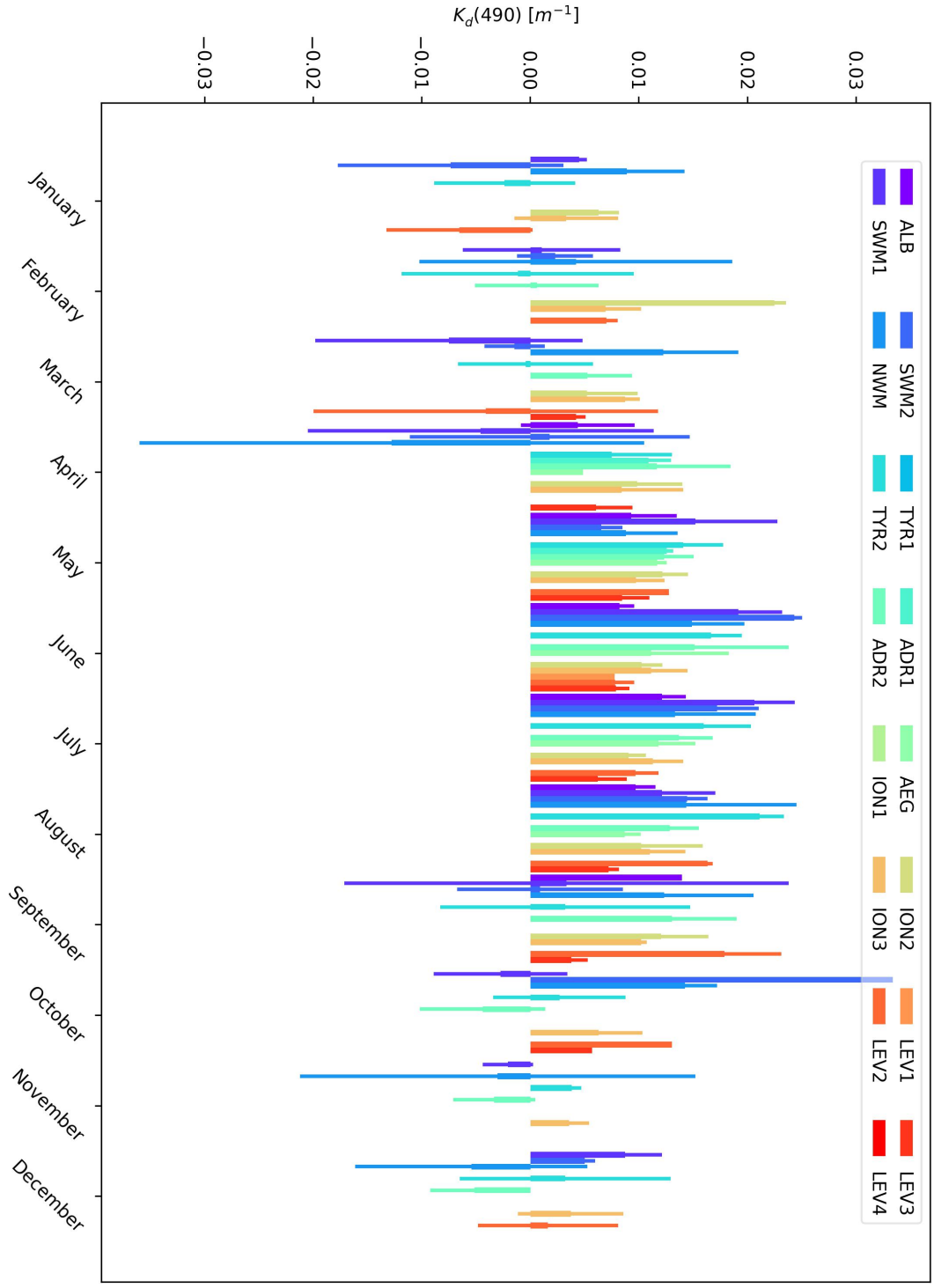

Figure 4.19. Monthly mean $K_d(490)$ values - difference between satellite and float measurements - with standard deviation lines per each subbasin, units of m^{-1}.

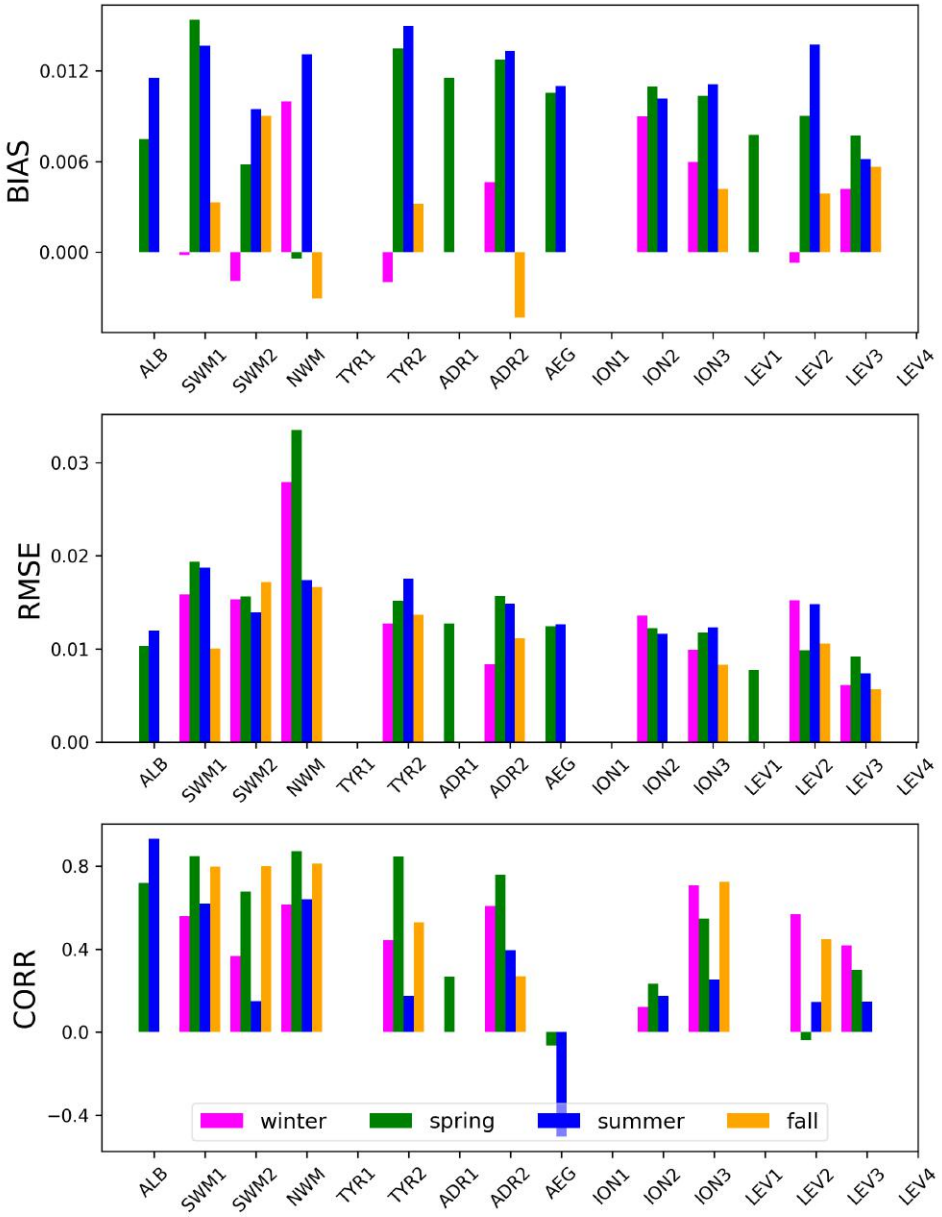

Figure 4.20. Seasonal statistical parameters per subbasin resulting from the match-up of $K_d(490)$ from floats and satellites. The first two figures show bias and RMSE (both in units of m^{-1}), whilst the bottom figure depicts the correlation coefficients.

4.4 Conclusions

The final chapter analysed Chl outputs from two reanalyses, utilizing two different diffuse attenuation coefficient data sets. The upgraded version resulted in a different product from two aspects, which could not be quantified separately: firstly, the interannual variability was introduced for the period between 1999 and 2015 and secondly, the product merged observations from 4 different satellites, thus resulting in a modified remote sensing algorithm, as shown in Volpe et al. [2007, 2017]. The previous data set had a 5-year time span to calculate a climatological year from SeaWiFS observations.

Spatial variability was quantified with K_d maps, where major differences were spotted in western and coastal regions. Chl maps at three different depth levels showed higher values in western subbasins at the surface during spring, at 50 m persisting also in summer months, followed by an enhancement in eastern parts at 100 m during summer and autumn, the last two cases corresponding to the period and depth of DCM formation in the regions.

Interannual variability on average does not increase with the introduction of K_d^{var}, in 5 out of 16 subbasins an increase of maximum 20% is noticed. Seasonal variability on the whole decreases for less than 5% with the exception of North Western Mediterranean and Southern Adriatic subbasins.

By using K_d^{var}, DCM deepens for 10 meters on average with decreasing Chl values in western subbasins from March to July for 0.02 $mg\,m^{-3}$ and increasing concentrations during early spring in eastern subbasins.

Examining the match-up between BGC-Argo data, it can be concluded that statistics improves with the use of K_d^{var} , although only slightly. The DYFAMED case showed drastic underestimation of Chl from models, varying for more than 50% during the entire time series.

Finally, a comparison between $K_d(490)$ from satellites and BGC-Argo floats revealed constantly higher satellite values for approximately 20 to 30%, resulting in numbers closer to $K_d(PAR)$. This could in turn provide additional insight both for model-tuning procedures, as well as for satellite product validation, since BGC-Argo floats prove to be a pioneering platform for ground truth measurements with such high spatio-temporal coverage.

A case study of this sort is addressed especially to CMEMS product users and ecological modellers who lack a more complex representation of the optical module. Introducing an interannually variable data set showed only a slight improvement in the model skill, if any, and is therefore only a small step in the path of possible modelling upgrades.

Furthermore, it is necessary to look at the modelling chain from a broader perspective, examining possible failures in accurately reproducing circulational patterns of the complex Mediterranean basin. Lower Chl values could, apart from having an over-simplified optical model, result from lower nutrient uptake due to incorrect initial conditions and insufficient vertical mixing.

As a conclusion, the importance of thinking towards multi- or hyperspectral solutions should be especially underlined, which would, through an analytical solution (the radiative transfer theory), link radiometry data to IOP and AOPs as model state variables rather than relying on remote sensing proxies, such as K_d, inherently derived from semi-empirical algorithms.

Discussion and conclusions

The main scope of the present thesis was to tackle the subject of light and its importance in marine biogeochemistry. Ocean optics is a relatively new field, the interest on which has expanded in the past 40 years, starting with the pioneering use of remote sensing techniques for biological applications, as well as with the development of radiative transfer theory for oceanographic purposes. Each of the methods widely accepted in the scientific community, such as remote sensing, in-situ platforms (e.g. BGC-Argo floats), research cruises and numerical models, have certain limitations. Satellites are, despite a long temporal acquisition and global spatial coverage, limited to surface layers and areas without clouds. Complex sensor calibration and atmospheric correction procedures can introduce large uncertainties in the retrieval of biogeochemical properties of interest. On the other hand, in-situ techniques, such as the examined BGC-Argo float network, can serve as ground truth data, thus avoiding issues related to atmospheric corrections, cloud coverage and especially depth limitations, hence regarded as a solid platform to validate satellite- or model-retrieved values, as well as reach areas which are otherwise inaccessible during cruises. Due to the relatively recent introduction of such technologies, several questions still need to be addressed in terms of sensor calibrations and sources or even magnitudes of uncertainties in relating direct measurements to final products (e.g. fluorescence-chlorophyll/CDOM concentration relationships). While both methods follow the current "pace" of introducing multi- or hyperspectral techniques, numerical models are in that aspect still lagging behind. An intermediate step towards the improvement of optics in numerical modelling applications was therefore examined in this monograph, the aim of which was to merge different methods and hence surpass the limitations of each tool considered separately.

BGC-Argo floats present a relatively novel approach in exploring physics and biogeochemistry of water regions subjected to measurements, thus a dataset study was necessary before starting with modelling applications, as it was done in Chapter 2, where the bio-optically anomalous nature of the Mediterranean Sea was examined with a re-evaluation of existent relationships between diffuse attenuation coefficients for downwelling irradiance and chlorophyll a

concentrations, derived especially for Case I waters. Findings confirmed the presence of DCM gradients, additionally showing systematically higher K_d values for western regions compared to the oligotrophic east. Highest attenuation coefficients were spotted at shorter wavelengths (380 nm) during winter and spring, decreasing in summer, which could be attributed to CDOM dynamics, the summer reduction most likely affected by photobleaching. Results of an updated regression analysis, following Morel and Maritorena [2001] and Morel et al. [2007b], showed high correlation when limiting the study to surface layers, however drastically deteriorating at shorter wavelengths when expanding the study to deeper layers. 380 and 412 nm wavelengths attenuate to 1% of the surface irradiance value at depths which are almost 3 times shallower compared to 490 nm. Chlorophyll thus proves to be insufficient as a biogeochemical parameter to describe the nature of K_d functions as in classical Case I water types. The enhanced absorption in the near-UV/blue suggests higher than average concentrations of CDOM (confirmed by previous publications) and possibly NAP (at present still no studies related to that). The relationship between $K_d(PAR)$ and $K_d(490)$ proved to be robust and should be further considered as a possible parametrization in 3-dimensional biogeochemical modelling cases, such as in the current OGSTM-BFM configuration.

Chapter 3 showed a combined approach, coupling 1-dimensional biogeochemical modelling with BGC-Argo data, integrating measurements both as an input information (in terms of photosynthetically available radiation) and for validation purposes (Chl profiles). Such an experiment was possible due to a large number of profiles with an unprecedented high vertical resolution of bio-optical measurements available in the region. Model simulations were able to reproduce first- (DCM profiles) and second-order features (vertical spikes or additional Chl profile patchiness). With known irradiance regimes and relatively simple vertical mixing configurations it was possible to reconstruct a large portion of Chl dynamics. Results conveyed that DCM depth is controlled mostly by irradiance, whereas nutrients regulate the amount of phytoplankton biomass at the same depth. The usage of PAR measured from BGC-Argo floats provides higher correlations compared to configurations with alternative bio-optical models, which also suggest the rate of improvements when considering a fully integrated value of light available for photosynthesis versus simplified approaches, which are usually embedded in ecological models. Results further support the strategic relevance of BGC-Argo data. Temperature, salinity and radiometric parameters encapsulate fundamental information for the reconstruction of primary producers dynamics and are paramount to investigate hypotheses concerning DCM formation. CDOM fluorescence data measured by BGC-Argo floats could be integrated in simulations to further infer and

reconstruct observed biogeochemical processes. Such an approach could be in future applied to regions other than the Mediterranean Sea (possibly on a global scale). Further details of this chapter's results can be found in Terzić et al. [2018].

Another example of a possible integration of different methods was analysed in Chapter 4. Two satellite remote sensing products for diffuse attenuation coefficients at 490 were compared and utilized as light extinction factors in the exponentially decreasing irradiance function, embedded in OGSTM-BFM 3-dimensional modelling system. The upgraded version of K_d^{var} maps introduced interannual variability (compared to the previously used climatological data set K_d^{clim}) and altogether resulted from merged observations of 4 satellites, which lead also to a different algorithm retrieval compared to the previously used dataset. Major differences in terms of chlorophyll concentrations arise in western regions during winter and spring months, coinciding with the bloom period. At intermediate depths, the enhancement spreads towards east with a time lag corresponding to the period and depth of DCM formation (i.e. summer months). Interannual variability on average does not increase with the introduction of K_d^{var}, in 5 out of 16 subbasins an increase of maximum 20% is noticed. Seasonal variability on the whole decreases for less than 5% with the exception of North Western Mediterranean and Southern Adriatic subbasins. By using K_d^{var}, DCM deepens for 10 meters on average with decreasing Chl values in western subbasins from March to July and increasing concentrations during early spring in eastern subbasins. Examining the match-up between BGC-Argo data, it can be concluded that statistics slightly improves with the use of K_d^{var}. The DYFAMED case showed significant underestimation of Chl from models, varying for more than 50% during the entire time series when comparing model outputs with HPLC data. Finally, a comparison between $K_d(490)$ from satellites and BGC-Argo floats revealed constantly higher satellite values for approximately 20 to 30%, resulting in numbers closer to $K_d(PAR)$. A case study of this sort is addressed especially to CMEMS product users and ecological modellers who lack a more complex representation of the optical module. Albeit introducing an interannually variable dataset showed only a slight improvement in the model skill, it constitutes a small step in the path of possible modelling upgrades. Furthermore, it is necessary to look at the modelling chain from a broader perspective, examining possible failures in accurately reproducing circulational patterns of the complex Mediterranean basin. Lower Chl values could, apart from having an over-simplified optical model, result from lower nutrient uptake due to incorrect initial conditions and insufficient vertical mixing.

In order to understand the ocean productivity in its complexity, an in-depth

knowledge on light attenuation along the water column is required, considering absorption and scattering properties (or inherent optical properties - IOPs) of the major constituents, which are most commonly divided into four groups: pure water, phytoplankton, colored dissolved organic matter (CDOM) and non-algal particles (NAP).

Most ecosystem models, including the one described in the present work, are increasing their spatial resolution while saving computational time, improving boundary conditions and adding more biogeochemical state variables, following the progress in ocean colour observation technologies and the use of inversion algorithms at a much slower pace [Fujii et al., 2007]. Due to their multi- or hyperspectral nature, such methods can provide more refined techniques to quantify biogeochemical variables (such as CDOM or particulate organic carbon - POC) and detect changes in ecology by discerning different phytoplankton pigments and functional types through their unique absorption and scattering signals.

The oversimplified description of optics in models can possibly lead to a detriment of the ecosystem predictions, both in terms of biogeochemistry (in the visible range), as well as in hydrodynamics (for the IR bands) [Mobley et al., 2015]. The use of a hyperspectral radiative transfer model could, with the use of accurate radiometry (vs. the currently used simple exponential functions), impact both the calculation of temperature stratification and therefore change the circulational patterns, additionally comparing and validating the output in terms of apparent optical properties (AOPs), especially remote sensing reflectance (R_{rs}), rather than biogeochemical variables. Considering a rapid progress in observational methods, comparing models to measurements or assimilating measurements into models should include modelling IOPs apart from biogeochemical properties [Fujii et al., 2007]. Such a modelling framework, where absorption and scattering coefficients could be available as state variables, would through the radiative transfer model impact both the physical and biogeochemical modules at each computational step and provide a more accurate modelling system.

Bibliography

Alvain, S., Moulin, C., Dandonneau, Y., and Bréon, F.-M. (2005). Remote sensing of phytoplankton groups in case 1 waters from global seawifs imagery. *Deep Sea Research Part I: Oceanographic Research Papers*, 52(11):1989–2004.

Antoine, D., Babin, M., Berthon, J.-F., Bricaud, A., Gentili, B., Loisel, H., Maritorena, S., and Stramski, D. (2014). Shedding light on the sea: André morel's legacy to optical oceanography. *Annual review of marine science*, 6:1–21.

Antoine, D., Chami, M., Claustre, H., d'Ortenzio, F., Morel, A., Bécu, G., Gentili, B., Louis, F., Ras, J., Roussier, E., et al. (2006). Boussole: a joint cnrs-insu, esa, cnes, and nasa ocean color calibration and validation activity.

Antoine, D., d'Ortenzio, F., Hooker, S. B., Bécu, G., Gentili, B., Tailliez, D., and Scott, A. J. (2008a). Assessment of uncertainty in the ocean reflectance determined by three satellite ocean color sensors (meris, seawifs and modis-a) at an offshore site in the mediterranean sea (boussole project). *Journal of Geophysical Research: Oceans*, 113(C7).

Antoine, D., Guevel, P., Desté, J.-F., Bécu, G., Louis, F., Scott, A. J., and Bardey, P. (2008b). The "boussole" buoy—a new transparent-to-swell taut mooring dedicated to marine optics: Design, tests, and performance at sea. *Journal of Atmospheric and Oceanic Technology*, 25(6):968–989.

Arnone, R. A., Wood, A. M., and Gould, R. W. (2004). The evolution of optical water mass classification. *Oceanography*, 17(2):14–15.

Babin, M. (2008). Phytoplankton fluorescence: theory, current literature and in situ measurement. *Real-time coastal observing systems for marine ecosystem dynamics and harmful algal blooms. UNESCO Publishing, Paris. p*, 860.

Babin, M., Stramski, D., Ferrari, G. M., Claustre, H., Bricaud, A., Obolensky, G., and Hoepffner, N. (2003). Variations in the light absorption coefficients of phytoplankton, nonalgal particles, and dissolved organic matter in coastal waters around europe. *Journal of Geophysical Research: Oceans*, 108(C7).

Baird, M. E., Adams, M. P., Babcock, R. C., Oubelkheir, K., Mongin, M., Wild-Allen, K. A., Skerratt, J., Robson, B. J., Petrou, K., Ralph, P. J., et al. (2016a). A biophysical representation of seagrass growth for application in a complex shallow-water biogeochemical model. *Ecological modelling*, 325:13–27.

Baird, M. E., Cherukuru, N., Jones, E., Margvelashvili, N., Mongin, M., Oubelkheir, K., Ralph, P. J., Rizwi, F., Robson, B. J., Schroeder, T., et al. (2016b). Remote-sensing reflectance and true colour produced by a coupled hydrodynamic, optical, sediment, biogeochemical model of the great barrier reef, australia: comparison with satellite data. *Environmental Modelling & Software*, 78:79–96.

Barale, V. and Schlittenhardt, P. M. (2012). *Ocean colour: theory and applications in a decade of CZCS experience*, volume 3. Springer Science & Business Media.

Barbieux, M., Uitz, J., Bricaud, A., Organelli, E., Poteau, A., Schmechtig, C., Gentili, B., Obolensky, G., Leymarie, E., Penkerc'h, C., et al. (2018). Assessing the variability in the relationship between the particulate backscattering coefficient and the chlorophyll a concentration from a global biogeochemical-argo database. *Journal of Geophysical Research: Oceans*, 123(2):1229–1250.

Belo Couto, A., Brotas, V., Mélin, F., Groom, S., and Sathyendranath, S. (2016). Inter-comparison of oc-cci chlorophyll-a estimates with precursor data sets. *International Journal of Remote Sensing*, 37(18):4337–4355.

Berman, T., Azov, Y., and Townsend, D. (1984a). Understanding oligotrophic oceans: can the eastern mediterranean be a useful model? In *Marine phytoplankton and productivity*, pages 101–112. Springer.

Berman, T., Townsend, D., Elsayed, S., Trees, C., and Azov, Y. (1984b). Optical transparency, chlorophyll and primary productivity in the eastern mediterranean near the israeli coast. *Oceanologica Acta*, 7(3):367–372.

Bidigare, R. R., Ondrusek, M. E., Morrow, J. H., and Kiefer, D. A. (1990). In-vivo absorption properties of algal pigments. In *Ocean Optics X*, volume 1302, pages 290–303. International Society for Optics and Photonics.

Bissett, W., Walsh, J., Dieterle, D., and Carder, K. (1999). Carbon cycling in the upper waters of the sargasso sea: I. numerical simulation of differential carbon and nitrogen fluxes. *Deep Sea Research Part I: Oceanographic Research Papers*, 46(2):205–269.

Boldrin, A., Miserocchi, S., Rabitti, S., Turchetto, M., Balboni, V., and Socal, G. (2002). Particulate matter in the southern adriatic and ionian sea: characterisation and downward fluxes. *Journal of Marine Systems*, 33:389–410.

Bosc, E., Bricaud, A., and Antoine, D. (2004). Seasonal and interannual variability in algal biomass and primary production in the mediterranean sea, as derived from 4 years of seawifs observations. *Global Biogeochemical Cycles*, 18(1).

Boss, E. S., Collier, R., Pegau, W., Larson, G., and Fennel, K. (2007). Measurements of spectral optical properties and their relation to biogeochemical variables and processes in crater lake, crater lake national park, or. In *Long-term Limnological Research and Monitoring at Crater Lake, Oregon*, pages 149–159. Springer.

Bracchini, L., Tognazzi, A., Dattilo, A. M., Decembrini, F., Rossi, C., and Loiselle, S. A. (2010). Sensitivity analysis of cdom spectral slope in artificial and natural samples: an application in the central eastern mediterranean basin. *Aquatic sciences*, 72(4):485–498.

Brewin, R. J., Devred, E., Sathyendranath, S., Lavender, S. J., and Hardman-Mountford, N. J. (2011). Model of phytoplankton absorption based on three size classes. *Applied Optics*, 50(22):4535–4549.

Bricaud, A., Babin, M., Claustre, H., Ras, J., and Tièche, F. (2010). Light absorption properties and absorption budget of southeast pacific waters. *Journal of Geophysical Research: Oceans*, 115(C8).

Bricaud, A., Babin, M., Morel, A., and Claustre, H. (1995). Variability in the chlorophyll-specific absorption coefficients of natural phytoplankton: Analysis and parameterization. *Journal of Geophysical Research: Oceans*, 100(C7):13321–13332.

Bricaud, A., Bosc, E., and Antoine, D. (2002). Algal biomass and sea surface temperature in the mediterranean basin: Intercomparison of data from various satellite sensors, and implications for primary production estimates. *Remote Sensing of Environment*, 81(2-3):163–178.

Bricaud, A., Claustre, H., Ras, J., and Oubelkheir, K. (2004). Natural variability of phytoplanktonic absorption in oceanic waters: Influence of the size structure of algal populations. *Journal of Geophysical Research: Oceans*, 109(C11).

Bricaud, A., Morel, A., and Andre, J. (1987). Spatial/temporal variability of algal biomass and potential productivity in the mauritanian upwelling zone, as estimated from czcs data. *Advances in Space Research*, 7(2):53–62.

Bricaud, A., Morel, A., Babin, M., Allali, K., and Claustre, H. (1998). Variations of light absorption by suspended particles with chlorophyll a concentration in oceanic (case 1) waters: Analysis and implications for bio-optical models. *Journal of Geophysical Research: Oceans*, 103(C13):31033–31044.

Bricaud, A., Morel, A., and Prieur, L. (1981). Absorption by dissolved organic matter of the sea (yellow substance) in the uv and visible domains 1. *Limnology and oceanography*, 26(1):43–53.

Buitenhuis, E., Vogt, M., Moriarty, R., Bednarsek, N., Doney, S., Leblanc, K., Le Quéré, C., Luo, Y.-W., O'Brien, C., O'Brien, T., et al. (2013). Maredat: towards a world atlas of marine ecosystem data. *Earth System Science Data*, 5:227–239.

Catalá, T. S., Martínez-Pérez, A. M., Nieto-Cid, M., Álvarez, M., Otero, J., Emelianov, M., Reche, I., Arístegui, J., and Álvarez-Salgado, X. A. (2018). Dissolved organic matter (dom) in the open mediterranean sea. i. basin–wide distribution and drivers of chromophoric dom. *Progress in Oceanography*, 165:35–51.

Christaki, U., Giannakourou, A., Van Wambeke, F., and Grégori, G. (2001). Nanoflagellate predation on auto-and heterotrophic picoplankton in the oligotrophic mediterranean sea. *Journal of Plankton Research*, 23(11):1297–1310.

Ciavatta, S., Brewin, R., Skákala, J., Polimene, L., de Mora, L., Artioli, Y., and Allen, J. I. (2018). Assimilation of ocean-color plankton functional types to improve marine ecosystem simulations. *Journal of Geophysical Research: Oceans*, 123(2):834–854.

Ciavatta, S., Torres, R., Martinez-Vicente, V., Smyth, T., Dall'Olmo, G., Polimene, L., and Allen, J. I. (2014). Assimilation of remotely-sensed optical properties to improve marine biogeochemistry modelling. *Progress in Oceanography*, 127:74–95.

Ciavatta, S., Torres, R., Saux-Picart, S., and Allen, J. I. (2011). Can ocean color assimilation improve biogeochemical hindcasts in shelf seas? *Journal of Geophysical Research: Oceans*, 116(C12).

Claustre, H., Morel, A., Hooker, S., Babin, M., Antoine, D., Oubelkheir, K., Bricaud, A., Leblanc, K., Queguiner, B., and Maritorena, S. (2002). Is desert dust making oligotrophic waters greener? *Geophysical Research Letters*, 29(10):107–1.

Cole, H., Henson, S., Martin, A., and Yool, A. (2012). Mind the gap: The impact of missing data on the calculation of phytoplankton phenology metrics. *Journal of Geophysical Research: Oceans*, 117(C8).

Corsini, G., Grasso, R., and Cipollini, P. (2002). Regional bio-optical algorithms for the alboran sea from a reflectance model and in situ data. *Geophysical research letters*, 29(15).

Crispi, G., Mosetti, R., Solidoro, C., and Crise, A. (2001). Nutrients cycling in mediterranean basins: the role of the biological pump in the trophic regime. *Ecological Modelling*, 138(1-3):101–114.

Cullen, J. J. (1982). The deep chlorophyll maximum: comparing vertical profiles of chlorophyll a. *Canadian Journal of Fisheries and Aquatic Sciences*, 39(5):791–803.

de Boyer Montégut, C., Madec, G., Fischer, A. S., Lazar, A., and Iudicone, D. (2004). Mixed layer depth over the global ocean: An examination of profile data and a profile-based climatology. *Journal of Geophysical Research: Oceans*, 109(C12).

Di Cicco, A., Sammartino, M., Marullo, S., and Santoleri, R. (2017). Regional empirical algorithms for an improved identification of phytoplankton functional types and size classes in the mediterranean sea using satellite data. *Frontiers in Marine Science*, 4:126.

Dolan, J., Claustre, H., Carlotti, F., Plounevez, S., and Moutin, T. (2002). Microzooplankton diversity: relationships of tintinnid ciliates with resources, competitors and predators from the atlantic coast of morocco to the eastern mediterranean. *Deep Sea Research Part I: Oceanographic Research Papers*, 49(7):1217–1232.

D'Ortenzio, F., Marullo, S., Ragni, M., d'Alcalà, M. R., and Santoleri, R. (2002). Validation of empirical seawifs algorithms for chlorophyll-a retrieval in the mediterranean sea: A case study for oligotrophic seas. *Remote Sensing of Environment*, 82(1):79–94.

D'Ortenzio, F. and Prieur, L. (2012). The upper mixed layer. *Life in the Mediterranean Sea: A look at habitat changes, edited by: Noga Stambler, Nova Science Publisher*, pages 127–156.

d'Ortenzio, F. and Ribera d'Alcalà, M. (2009). On the trophic regimes of the mediterranean sea: a satellite analysis. *Biogeosciences*, 6(2):139–148.

Dutkiewicz, S., Hickman, A. E., Jahn, O., Gregg, W. W., Mouw, C. B., and Follows, M. J. (2015). Capturing optically important constituents and properties in a marine biogeochemical and ecosystem model. *Biogeosciences*, 12(14):4447–4481.

Ebenhoh, W., Baretta-Bekker, J., and Baretta, J. (1997). The primary production module in the marine ecosystem model ersem ii, with emphasis on the light forcing. *Journal of Sea Research*, 38(3-4):173–193.

Estrada, M., Marrasé, C., Latasa, M., Berdalet, E., Delgado, M., and Riera, T. (1993). Variability of deep chlorophyll maximum characteristics in the northwestern mediterranean. *Marine Ecology Progress Series*, pages 289–300.

Feynman, R. P. (2006). *QED: The strange theory of light and matter*. Princeton University Press.

Fujii, M., Boss, E., and Chai, F. (2007). The value of adding optics to ecosystem models: a case study. *Biogeosciences Discussions*, 4(3):1585–1631.

Fusco, G., Manzella, G., Cruzado, A., Gacic, M., Gasparini, G., Kovacevic, V., Millot, C., Tziavos, C., Velásquez, Z., Walne, A., et al. (2003). Variability of mesoscale features in the mediterranean sea from xbt data analysis.

Gitelson, A., Karnieli, A., Goldman, N., Yacobi, Y., and Mayo, M. (1996). Chlorophyll estimation in the southeastern mediterranean using czcs images: adaptation of an algorithm and its validation. *Journal of Marine Systems*, 9(3-4):283–290.

Gordon, H. R. (1973). Simple calculation of the diffuse reflectance of the ocean. *Applied Optics*, 12(12):2803–2804.

Gordon, H. R. (1989). Can the lambert-beer law be applied to the diffuse attenuation coefficient of ocean water? *Limnology and Oceanography*, 34(8):1389–1409.

Gordon, H. R., Brown, O. B., Evans, R. H., Brown, J. W., Smith, R. C., Baker, K. S., and Clark, D. K. (1988). A semianalytic radiance model of ocean color. *Journal of Geophysical Research: Atmospheres*, 93(D9):10909–10924.

Gordon, H. R. and McCluney, W. (1975). Estimation of the depth of sunlight penetration in the sea for remote sensing. *Applied optics*, 14(2):413–416.

Gregg, W. W. and Casey, N. W. (2007). Modeling coccolithophores in the global oceans. *Deep Sea Research Part II: Topical Studies in Oceanography*, 54(5-7):447–477.

Hogan, R. (2017). Radiation quantities in the ecmwf model and mars.

Huot, Y. and Antoine, D. (2016). Remote sensing reflectance anomalies in the ocean. *Remote Sensing of Environment*, 184:101–111.

IOCCG (2006). *Remote Sensing of Inherent Optical Properties: Fundamentals, Tests of Algorithms, and Applications*, volume No. 5 of *Reports of the International Ocean Colour Coordinating Group*. IOCCG, Dartmouth, Canada.

IOCCG (2008). *Why Ocean Colour? The Societal Benefits of Ocean-Colour Technology*, volume No. 7 of *Reports of the International Ocean Colour Coordinating Group*. IOCCG, Dartmouth, Canada.

IOCCG (2011). *Bio-Optical Sensors on Argo Floats*, volume No. 11 of *Reports of the International Ocean Colour Coordinating Group*. IOCCG, Dartmouth, Canada.

IOCCG (2014). *Phytoplankton Functional Types from Space*, volume No. 15 of *Reports of the International Ocean Colour Coordinating Group*. IOCCG, Dartmouth, Canada.

Jerlov, N. (1968). Optical oceanography, vol. 5 of elsevier oceanography series.

Jerlov, N. G. (1976). *Marine optics*, volume 14. Elsevier.

Johnson, K. and Claustre, H. (2016). Bringing biogeochemistry into the argo age. *Eos*, 97(10.1029).

Jones, E. M., Baird, M. E., Mongin, M., Parslow, J., Skerratt, J., Lovell, J., Margvelashvili, N., Matear, R. J., Wild-Allen, K., Robson, B., et al. (2016). Use of remote-sensing reflectance to constrain a data assimilating marine biogeochemical model of the great barrier reef. *Biogeosciences*, 13(23):6441–6469.

Kiefer, D. (1973). Fluorescence properties of natural phytoplankton populations. *Marine Biology*, 22(3):263–269.

Kirk, J. T. (1994). *Light and photosynthesis in aquatic ecosystems*. Cambridge university press.

Kitidis, V., Uher, G., Upstill-Goddard, R., Mantoura, R., Spyres, G., and Woodward, E. (2006). Photochemical production of ammonium in the oligotrophic cyprus gyre (eastern mediterranean). *Biogeosciences*, 3(4):439–449.

Kohlmeier, C. and Ebenhöh, W. (2009). Modelling the biogeochemistry of a tidal flat ecosystem with ecotim. *Ocean dynamics*, 59(2):393–415.

Lacombe, H. (1990). A model of the world ocean-water, salt, heat, and wind in the med. *Oceanus*, 33(1):26–36.

Lavigne, H., D'ortenzio, F., d'Alcalà, M. R., Claustre, H., Sauzède, R., and Gacic, M. (2015). On the vertical distribution of the chlorophyll a concentration in the mediterranean sea: a basin-scale and seasonal approach. *Biogeosciences*, 12(16):5021–5039.

Lazzari, P., Solidoro, C., Ibello, V., Salon, S., Teruzzi, A., Béranger, K., Colella, S., and Crise, A. (2012). Seasonal and inter-annual variability of plankton chlorophyll and primary production in the mediterranean sea: a modelling approach. *Biogeosciences*, 9(1):217.

Lazzari, P., Solidoro, C., Salon, S., and Bolzon, G. (2016). Spatial variability of phosphate and nitrate in the mediterranean sea: A modeling approach. *Deep Sea Research Part I: Oceanographic Research Papers*, 108:39–52.

Lazzari, P., Teruzzi, A., Salon, S., Campagna, S., Calonaci, C., Colella, S., Tonani, M., and Crise, A. (2010). Pre-operational short-term forecasts for mediterranean sea biogeochemistry. *Ocean Science*, 6(1):25–39.

Leblanc, K., Quéguiner, B., Diaz, F., Cornet, V., Michel-Rodriguez, M., de Madron, X. D., Bowler, C., Malviya, S., Thyssen, M., Grégori, G., et al. (2018). Nanoplanktonic diatoms are globally overlooked but play a role in spring blooms and carbon export. *Nature communications*, 9(1):953.

Lee, Z. and Hu, C. (2006). Global distribution of case-1 waters: An analysis from seawifs measurements. *Remote Sensing of Environment*, 101(2):270–276.

Lee, Z., Shang, S., Hu, C., Du, K., Weidemann, A., Hou, W., Lin, J., and Lin, G. (2015). Secchi disk depth: A new theory and mechanistic model for underwater visibility. *Remote sensing of environment*, 169:139–149.

Lee, Z., Shang, S., Qi, L., Yan, J., and Lin, G. (2016). A semi-analytical scheme to estimate secchi-disk depth from landsat-8 measurements. *Remote sensing of environment*, 177:101–106.

Lee, Z.-P., Du, K.-P., and Arnone, R. (2005). A model for the diffuse attenuation coefficient of downwelling irradiance. *Journal of Geophysical Research: Oceans*, 110(C2).

Loisel, H. and Morel, A. (1998). Light scattering and chlorophyll concentration in case 1 waters: A reexamination. *Limnology and Oceanography*, 43(5):847–858.

Loisel, H., Vantrepotte, V., Norkvist, K., Meriaux, X., Kheireddine, M., Ras, J., Pujo-Pay, M., Combet, Y., Leblanc, K., Dall'Olmo, G., et al. (2011). Characterization of the bio-optical anomaly and diurnal variability of particulate matter, as seen from scattering and backscattering coefficients, in ultra-oligotrophic eddies of the mediterranean sea. *Biogeosciences*, 8(11):3295–3317.

Manca, B., Burca, M., Giorgetti, A., Coatanoan, C., Garcia, M.-J., and Iona, A. (2004). Physical and biochemical averaged vertical profiles in the mediterranean regions: an important tool to trace the climatology of water masses and to validate incoming data from operational oceanography. *Journal of Marine Systems*, 48(1):83–116.

Marty, J.-C., Chiavérini, J., Pizay, M.-D., and Avril, B. (2002). Seasonal and interannual dynamics of nutrients and phytoplankton pigments in the western mediterranean sea at the dyfamed time-series station (1991–1999). *Deep Sea Research Part II: Topical Studies in Oceanography*, 49(11):1965–1985.

Megard, R. O. and Berman, T. (1989). Effects of algae on the secchi transparency of the southeastern mediterranean sea. *Limnology and Oceanography*, 34(8):1640–1655.

Mignot, A., Claustre, H., Uitz, J., Poteau, A., D'Ortenzio, F., and Xing, X. (2014). Understanding the seasonal dynamics of phytoplankton biomass and the deep chlorophyll maximum in oligotrophic environments: A bio-argo float investigation. *Global Biogeochemical Cycles*, 28(8):856–876.

Mignot, A., Ferrari, R., and Claustre, H. (2018). Floats with bio-optical sensors reveal what processes trigger the north atlantic bloom. *Nature communications*, 9(1):190.

Mitchell, B. G. (1992). Predictive bio-optical relationships for polar oceans and marginal ice zones. *Journal of Marine Systems*, 3(1-2):91–105.

Mitchell, B. G. and Holm-Hansen, O. (1991). Bio-optical properties of antarctic peninsula waters: Differentiation from temperate ocean models. *Deep Sea Research Part A. Oceanographic Research Papers*, 38(8-9):1009–1028.

Mobley, C., Boss, E., and Roesler, C. (2010). Ocean optics web book.

Mobley, C. D. (1994). *Light and water: radiative transfer in natural waters*. Academic press.

Mobley, C. D., Chai, F., Xiu, P., and Sundman, L. K. (2015). Impact of improved light calculations on predicted phytoplankton growth and heating in an idealized upwelling-downwelling channel geometry. *Journal of Geophysical Research: Oceans*, 120(2):875–892.

Mobley, C. D., Stramski, D., Bissett, W. P., and Boss, E. (2004). Optical modeling of ocean waters: Is the case 1-case 2 classification still useful? *Oceanography*, 17(2):60–67.

Mobley, C. D., Werdell, J., Franz, B., Ahmad, Z., and Bailey, S. (2016). Atmospheric correction for satellite ocean color radiometry.

Morel, A. (1988). Optical modeling of the upper ocean in relation to its biogenous matter content(case i waters). *Journal of Geophysical Research*, 93(10):749–10.

Morel, A. and Bricaud, A. (1981). Theoretical results concerning light absorption in a discrete medium, and application to specific absorption of phytoplankton. *Deep-Sea Res*, 28(11):1375–1393.

Morel, A., Claustre, H., Antoine, D., and Gentili, B. (2007a). Natural variability of bio-optical properties in case 1 waters: attenuation and reflectance within the visible and near-uv spectral domains, as observed in south pacific and mediterranean waters. *Biogeosciences Discussions*, 4(4):2147–2178.

Morel, A. and Gentili, B. (2009). The dissolved yellow substance and the shades of blue in the mediterranean sea. *Biogeosciences*, 6(11).

Morel, A., Huot, Y., Gentili, B., Werdell, P. J., Hooker, S. B., and Franz, B. A. (2007b). Examining the consistency of products derived from various ocean color sensors in open ocean (case 1) waters in the perspective of a multi-sensor approach. *Remote Sensing of Environment*, 111(1):69–88.

Morel, A. and Maritorena, S. (2001). Bio-optical properties of oceanic waters-a reappraisal. *Journal of Geophysical research*, 106(C4):7163–7180.

Morel, A. and Prieur, L. (1977). Analysis of variations in ocean color 1. *Limnology and oceanography*, 22(4):709–722.

Moutin, T. and Raimbault, P. (2002). Primary production, carbon export and nutrients availability in western and eastern mediterranean sea in early summer 1996 (minos cruise). *Journal of marine systems*, 33:273–288.

Mouw, C. B., Hardman-Mountford, N. J., Alvain, S., Bracher, A., Brewin, R. J., Bricaud, A., Ciotti, A. M., Devred, E., Fujiwara, A., Hirata, T., et al. (2017). A consumer's guide to satellite remote sensing of multiple phytoplankton groups in the global ocean. *Frontiers in Marine Science*, 4:41.

Navarro, G., Almaraz, P., Caballero, I., Vázquez, Á., and Huertas, I. E. (2017). Reproduction of spatio-temporal patterns of major mediterranean phytoplankton groups from remote sensing oc-cci data. *Frontiers in Marine Science*, 4:246.

Navarro, G., Alvain, S., Vantrepotte, V., and Huertas, I. E. (2014). Identification of dominant phytoplankton functional types in the mediterranean sea based on a regionalized remote sensing approach. *Remote Sensing of Environment*, 152:557–575.

Nelson, N. B. and Siegel, D. A. (2013). The global distribution and dynamics of chromophoric dissolved organic matter. *Annual Review of Marine Science*, 5:447–476.

O'Reilly, J. E., Maritorena, S., Mitchell, B. G., Siegel, D. A., Carder, K. L., Garver, S. A., Kahru, M., and McClain, C. (1998). Ocean color chlorophyll algorithms for seawifs. *Journal of Geophysical Research: Oceans*, 103(C11):24937–24953.

Organelli, E., Bricaud, A., Antoine, D., and Matsuoka, A. (2014). Seasonal dynamics of light absorption by chromophoric dissolved organic matter (cdom) in the nw mediterranean sea (boussole site). *Deep Sea Research Part I: Oceanographic Research Papers*, 91:72–85.

Organelli, E., Claustre, H., Bricaud, A., Barbieux, M., Uitz, J., D'Ortenzio, F., and Dall'Olmo, G. (2017). Bio-optical anomalies in the world's oceans: An investigation on the diffuse attenuation coefficients for downward irradiance derived from biogeochemical argo float measurements. *Journal of Geophysical Research: Oceans*, 122(5):3543–3564.

Organelli, E., Claustre, H., Bricaud, A., Schmechtig, C., Poteau, A., Xing, X., Prieur, L., D'Ortenzio, F., Dall'Olmo, G., and Vellucci, V. (2016). A novel near-real-time quality-control procedure for radiometric profiles measured

by bio-argo floats: Protocols and performances. *Journal of Atmospheric and Oceanic Technology*, 33(5):937–951.

Organelli, E., Nuccio, C., Melillo, C., and Massi, L. (2011). Relationships between phytoplankton light absorption, pigment composition and size structure in offshore areas of the mediterranean sea. *Advances in Oceanography and Limnology*, 2(2):107–123.

Pérez, G. L., Galí, M., Royer, S.-J., Sarmento, H., Gasol, J. M., Marrasé, C., and Simó, R. (2016). Bio-optical characterization of offshore nw mediterranean waters: Cdom contribution to the absorption budget and diffuse attenuation of downwelling irradiance. *Deep Sea Research Part I: Oceanographic Research Papers*, 114:111–127.

Pinardi, N. and Masetti, E. (2000). Variability of the large scale general circulation of the mediterranean sea from observations and modelling: a review. *Palaeogeography, Palaeoclimatology, Palaeoecology*, 158(3-4):153–173.

Powley, H. R., Krom, M. D., and Van Cappellen, P. (2017). Understanding the unique biogeochemistry of the mediterranean sea: Insights from a coupled phosphorus and nitrogen model. *Global Biogeochemical Cycles*.

Preisendorfer, R. W. (1986). Secchi disk science: Visual optics of natural waters 1. *Limnology and oceanography*, 31(5):909–926.

Riley, G. A. (1956). *Oceanography of Long Island Sound, 1952-54*, volume 15. Bingham Oceanographic Laboratory.

Riley, G. A. (1975). Transparency-chlorophyll relations. *Limnology and Oceanography*, 20(1):150–152.

Roesler, C., Uitz, J., Claustre, H., Boss, E., Xing, X., Organelli, E., Briggs, N., Bricaud, A., Schmechtig, C., Poteau, A., et al. (2017). Recommendations for obtaining unbiased chlorophyll estimates from in situ chlorophyll fluorometers: A global analysis of wet labs eco sensors. *Limnology and Oceanography: Methods*, 15(6):572–585.

Roesler, C. S. and Barnard, A. H. (2013). Optical proxy for phytoplankton biomass in the absence of photophysiology: Rethinking the absorption line height. *Methods in Oceanography*, 7:79–94.

Ryabov, A. B. and Blasius, B. (2011). A graphical theory of competition on spatial resource gradients. *Ecology Letters*, 14(3):220–228.

Ryabov, A. B. and Blasius, B. (2014). Depth of the biomass maximum affects the rules of resource competition in a water column. *The American Naturalist*, 184(5):E132–E146.

Sammartino, M., Di Cicco, A., Marullo, S., and Santoleri, R. (2015). Spatio-temporal variability of micro-, nano-and pico-phytoplankton in the mediterranean sea from satellite ocean colour data of seawifs. *Ocean Science Discussions*, 12(1).

Santoleri, R., Volpe, G., Marullo, S., and Nardelli, B. B. (2008). Open waters optical remote sensing of the mediterranean sea. In *Remote sensing of the European seas*, pages 103–116. Springer.

Schmechtig, C., Claustre, H., Poteau, A., and D'Ortenzio, F. (2014). Bio-argo quality control manual for the chlorophyll-a concentration.

Sempere, R., Para, J., Tedetti, M., Charriere, B., and Mallet, M. (2015). Variability of solar radiation and cdom in surface coastal waters of the northwestern mediterranean sea. *Photochemistry and photobiology*, 91(4):851–861.

Sieburth, J. M., Smetacek, V., and Lenz, J. (1978). Pelagic ecosystem structure: Heterotrophic compartments of the plankton and their relationship to plankton size fractions 1. *Limnology and oceanography*, 23(6):1256–1263.

Siokou-Frangou, I., Christaki, U., Mazzocchi, M. G., Montresor, M., Ribera d'Alcalà, M., Vaqué, D., and Zingone, A. (2010). Plankton in the open mediterranean sea: a review.

Storm, T., Boettcher, M., Grant, M., Zühlke, M., Fomferra, N., Jackson, T., and Sathyendranath, S. (2013). Product user guide, ocean colour climate change initiative. *Plymouth: Plymouth Marine Laboratory*.

Swan, C. M., Siegel, D. A., Nelson, N. B., Carlson, C. A., and Nasir, E. (2009). Biogeochemical and hydrographic controls on chromophoric dissolved organic matter distribution in the pacific ocean. *Deep Sea Research Part I: Oceanographic Research Papers*, 56(12):2175–2192.

Szeto, M., Werdell, P., Moore, T., and Campbell, J. (2011). Are the world's oceans optically different? *Journal of Geophysical Research: Oceans*, 116(C7).

Tanhua, T., Hainbucher, D., Schroeder, K., Cardin, V., Álvarez, M., and Civitarese, G. (2013). The mediterranean sea system: a review and an introduction to the special issue. *Ocean Science*, 9(5):789–803.

Teruzzi, A., Bolzon, G., Salon, S., Lazzari, P., Solidoro, C., and Cossarini, G. (2018). Assimilation of coastal and open sea biogeochemical data to improve phytoplankton simulation in the mediterranean sea. *Ocean Modelling*, 132:46–60.

Teruzzi, A., Dobricic, S., Solidoro, C., and Cossarini, G. (2014). A 3-d variational assimilation scheme in coupled transport-biogeochemical models: Forecast of mediterranean biogeochemical properties. *Journal of Geophysical Research: Oceans*, 119(1):200–217.

Terzić, E., Lazzari, P., Organelli, E., Solidoro, C., Salon, S., D'Ortenzio, F., and Conan, P. (2018). Merging bio-optical data from biogeochemical-argo floats and models in marine biogeochemistry. *Biogeosciences Discussions*, 2018:1–32.

Turley, C., Bianchi, M., Christaki, U., Conan, P., Harris, J., Psarra, S., Ruddy, G., Stutt, E., Tselepides, A., and Van Wambeke, F. (2000). Relationship between primary producers and bacteria in an oligotrophic sea–the mediterranean and biogeochemical implications. *Marine Ecology Progress Series*, 193:11–18.

Uitz, J., Stramski, D., Gentili, B., D'Ortenzio, F., and Claustre, H. (2012). Estimates of phytoplankton class-specific and total primary production in the mediterranean sea from satellite ocean color observations. *Global Biogeochemical Cycles*, 26(2).

Valente, A., Sathyendranath, S., Brotas, V., Groom, S., Grant, M., Taberner, M., Antoine, D., Arnone, R., Balch, W. M., Barker, K., et al. (2016). A compilation of global bio-optical in situ data for ocean-colour satellite applications. *Earth System Science Data*, 8(1):235–252.

Vichi, M., Cossarini, G., Gutierrez, M., Lazzari, P., Lovato, T., Mattia, G., Masina, S., McKiver, W., Pinardi, N., Solidoro, C., and Zavatarelli, M. (2013). The Biogeochemical Flux Model (BFM): Equation description and user manual. BFM Report series 1, BFM version 5 (BFM-V5), Bologna, Italy.

Vidussi, F., Claustre, H., Manca, B. B., Luchetta, A., and Marty, J.-C. (2001). Phytoplankton pigment distribution in relation to upper thermocline circulation in the eastern mediterranean sea during winter. *Journal of Geophysical Research: Oceans*, 106(C9):19939–19956.

Viúdez, A., Pinot, J.-M., and Haney, R. (1998). On the upper layer circulation in the alboran sea. *Journal of Geophysical Research: Oceans*, 103(C10):21653–21666.

Volpe, G., Pitarch, J., Colella, S., Brando, V., Forneris, V., Bracaglia, M., and Benincasa, M. (2017). Ocean colour production centre.

Volpe, G., Santoleri, R., Vellucci, V., d'Alcalà, M. R., Marullo, S., and d'Ortenzio, F. (2007). The colour of the mediterranean sea: Global versus regional bio-optical algorithms evaluation and implication for satellite chlorophyll estimates. *Remote Sensing of Environment*, 107(4):625–638.

Werdell, P. J., McKinna, L. I., Boss, E., Ackleson, S. G., Craig, S. E., Gregg, W. W., Lee, Z., Maritorena, S., Roesler, C. S., Rousseaux, C. S., et al. (2018). An overview of approaches and challenges for retrieving marine inherent optical properties from ocean color remote sensing. *Progress in Oceanography*.

Wernand, M. and Van der Woerd, H. (2010). Spectral analysis of the forel-ule ocean colour comparator scale. *Journal of the European Optical Society-Rapid Publications*, 5.

Xing, X., Claustre, H., Blain, S., D'Ortenzio, F., Antoine, D., Ras, J., and Guinet, C. (2012a). Quenching correction for in vivo chlorophyll fluorescence acquired by autonomous platforms: A case study with instrumented elephant seals in the kerguelen region (southern ocean). *Limnology and Oceanography: Methods*, 10(7):483–495.

Xing, X., Claustre, H., Wang, H., Poteau, A., and Fabrizio, D. (2014). Seasonal dynamics in colored dissolved organic matter in the mediterranean sea: Patterns and drivers. *Deep Sea Research Part I: Oceanographic Research Papers*, 83:93–101.

Xing, X., Morel, A., Claustre, H., Antoine, D., D'Ortenzio, F., Poteau, A., and Mignot, A. (2011). Combined processing and mutual interpretation of radiometry and fluorimetry from autonomous profiling bio-argo floats: Chlorophyll a retrieval. *Journal of Geophysical Research: Oceans*, 116(C6).

Xing, X., Morel, A., Claustre, H., D'Ortenzio, F., and Poteau, A. (2012b). Combined processing and mutual interpretation of radiometry and fluorometry from autonomous profiling bio-argo floats: 2. colored dissolved organic matter absorption retrieval. *Journal of Geophysical Research: Oceans*, 117(C4).

Zaneveld, J. R. V., Kitchen, J. C., and Mueller, J. L. (1993). Vertical structure of productivity and its vertical integration as derived from remotely sensed observations. *Limnology and Oceanography*, 38(7):1384–1393.